USING ELECTRICAL CHEMICAL IMPEDANCE SPECTROSCOPY TO DETERMINE NANOCAPILLARY GEOMETRY AND DIFFERENTIAL CAPACITANCE BY DEVELOPING A VARIABLE TOPOLOGY NETWORK CIRCUIT MODEL

BY MICHAEL J VITARELLI JR.

A dissertation submitted to the

Graduate School—New Brunswick

Rutgers, The State University of New Jersey

in partial fulfillment of the requirements

for the degree of

Doctor of Philosophy

Graduate Program in Chemistry and Chemical Biology

Written under the direction of

David S. Talaga

and approved by

New Brunswick, New Jersey

May, 2013

ABSTRACT OF THE DISSERTATION

Using Electrical Chemical Impedance Spectroscopy to determine nanocapillary geometry and differential capacitance by developing a variable topology network circuit model

by Michael J Vitarelli Jr.

Dissertation Director: David S. Talaga

Nanocapillaries find increasing use in a variety of applications including, protein translocation dynamics, protein sequencing, and other nanofluidic studies. All of these applications are affected by the geometry of the nanopore and the molecular species found within. This dissertation develops a new equivalent circuit model to determine the geometry of nanocapillaries. This model is derived to include the effects of a varying nanocapillary radius, along with the capacitive double layer within the nanocpaillary. The model is tested by using electrochemical impedance spectroscopy on a nanocapillary array membrane. The resulting values extracted from the model fit are consistent with the manufacturer's specified geometry. The model is then further developed to determine the impedance of proteins. This is accomplished by modeling the protein as a cylinder and inserting this into our above mentioned model. By exploiting alternating regions of surface charge density on the protein this model will allow for the rapid sequencing of proteins.

Acknowledgements

I owe a great deal of gratitude to many people who have helped me along the way. Primarily are my parents for putting me though my undergraduate studies and the rest of my family for support and encouragement. My group members Xianglan He, Jeremy Pronchick who is the best Maelstrom player I have ever meet, and Jason Giurleo, eventhough I'm half Jason's weight I can still eat a foot long quick check Italian sub faster then he can. Outside my group I would like to thank Steve Dulin at GE Osmonics for happily answering my numerous questions on the material properties and fabrication of NCAMs. From the mechanical engineering department I would like to thank John Petrowski for assistance in using various fabrication instruments. My girlfriend Kathy Chen for giving me an interesting life outside of work. To Charles Dismukes for use of his potentiostat. To my committee members, Alexander Neimark, Ed Castner (who is not color blind, yet sometimes wears purple pants) and Jane Hinch for many years of exciting physical chemistry lab teaching assignments. Lastly, I would like to thank my advisor David Talaga for many things, including giving me interesting problems to work on and teaching me the importance of reproducibility in experiments.

Dedication

To my parents.

Table of Contents

Abstract ii

Acknowledgements iii

Dedication iv

List of Tables viii

List of Figures ix

1. Introduction 2

- 1.1. Overview 2
- 1.2. Circuit Theory 4
- 1.3. Electrical Impedance 7
  - 1.3.1. R || C Circuits 8
  - 1.3.2. R + R || C Circuits 9
  - 1.3.3. Purely capacitive circuit elements 11
  - 1.3.4. R+C Circuits 11
  - 1.3.5. Constant Phase Element 15
- 1.4. Peak Frequency Optimization 16
- 1.5. System Modeling 19

2. Determining Nanocapillary Geometry From Electrochemical Impedance Spectroscopy Using the Variable Topology Finite Warburg Impedance Model 27

- 2.1. Introduction 27
- 2.2. Theoretical Model 28
  - 2.2.1. Solution for constant radius 29

2.2.2. Solution for linearly varying radius 31
2.2.3. Model Geometry extension 33
2.3. Methods 34
2.3.1. Support Chamber 34
2.3.2. NCAM 35
2.3.3. Potentiostat 36
2.3.4. Fitting and Active Set 37
2.4. System modeling 37
2.5. Nanocapillary Models 39
2.6. Local fits reveal global NCAM EIS model 42
2.7. EIS global fitting gives NCAM geometry 44
2.8. Possible model limitations 46
2.9. Comparison of fit parameters and manufacturer's specifications 48
2.10. Conclusion 49

3. Theoretical Models for Electrochemical Impedance Spectroscopy of Unfolded Proteins Though Nanopores and Relation to Zeta Potential 55
3.1. Introduction 55
3.2. Results and Discussion 57
3.2.1. Developing the modified differential equation 57
3.2.2. Evaluating the solution 59
3.2.3. Completing the model: Inclusion of the chip impedance 60
3.2.4. Differential capacitance and zeta potential formalism 62
3.2.5. Transient Analysis 66
3.3. Conclusion 66

4. Focused Ion Beam : FIB 74
4.1. Introduction 74
4.2. Methods 74
4.3. Results and Discussion 75

4.3.1. Conical Model 75

4.3.2. Local Fitting 76

4.3.3. Global fitting 79

4.4. Conclusion 80

5. The NCAM DC Bias 85

5.1. The DC Bias 85

5.1.1. Inclusion of an inductor and CPE 86

Appendix A. Gouy-Chapman Model 91

A.1. Gouy-Chapman Model 91

Appendix B. Capacitance Models and the Stern Layer 95

B.1. Planar Model 95

B.2. Spherical Model 96

B.3. Cylindrical Model 96

B.4. Relation to Stern layer capacitance 97

Appendix C. Warburg Impedance 100

C.1. Developing the Warburg Impedance Model 100

C.2. Model Limits 101

Appendix D. Other Nanopore EIS Data 104

D.1. Clogging of a Nanopore 104

D.2. Gamry Single Nanopore Data 104

D.3. Parstat 2263 Potentiostat Single Nanopore and FIB 105

D.4. NCAM Wetting Kinetics 105

Appendix E. Spherical Case 108

List of Tables

2.1. Quality of Model Fits 42

2.2. Parameters for local fits to $Z_{\mathrm{VTW}} = Z_{\mathrm{cyl}} + Z_{\mathrm{loz}}$ 43

2.3. NCAM EIS global fit parameters 46

2.4. NCAM Nomenclature List 50

3.1. Nomenclature List 69

4.1. Parameters for local fits 76

4.2. Quality of Model Fits 79

4.3. FIB EIS global fit parameters 80

4.4. Nomenclature List 81

C.1. Warburg Nomenclature List 102

List of Figures

1.1. Here an application of KCL is shown, where the current entering the node is equal to the current leaving the node. 4

1.2. Here an application of KVL is shown. The voltage drop across each of the resistors is equal to that of the voltage source. 5

1.3. An infinite series of resistors each with resistance R is shown. By summing the resistors an equivalent resistance of approximately 1.62R is found. 7

1.4. All three figures above are representative of an $R \parallel C$ circuit, using 50 frequency points ranging from 0.1 Hz to 1 MHz along with a 100 Ohm resistor and a 0.1 mF capacitor. Left panel equation 1.18 is plotted, while in the center panel equation 1.21 is shown. Notice the phase angle approaches zero as the frequency approaches zero, while the phase angle approaches -90 degrees in the high frequency limit. Right panel the magnitude of equation 1.18 is plotted. Notice in the DC limit, the zero frequency limit the magnitude of the impedance is that of the resistor. This is true since the impedance of the capacitor will approach infinity in the low frequency limit. Thus the current will follow the path of the resistor. On the other hand, at the high frequency limit the impedance of the capacitor will approach zero and the current path will follow that of the capacitor, yielding a zero impedance. 10

1.5. All three figures above are representative of an $R + R \parallel C$ circuit, using 50 frequency points ranging from 0.1 Hz to 1 MHz along with a 100 Ohm resistor, a 0.1 mF capacitor, and R_{sln}=20 Ohms. Left panel equation 1.24 is plotted. Notice the only difference between the Nyquist plots in figure 1.4 and figure 1.5 is that figure 1.5 is offset by an addition 20 ohms vs that of figure 1.4. This is also true for the magnitude of impedance figures. The phase angle is plotted with six different values for R_{sln}. These being 20, 2, 0.2, 0.02, 0.002, and 0 ohms, red, blue, green, purple, cyan, and black respectively. Notice the 0 ohm plot, the black plot, is identical to that of figure 1.4. 10

1.6. All three figures above are representative of a purely capacitive circuit element, using 50 frequency points ranging from 0.1 Hz to 1 MHz along with a 0.1 mF capacitor. Left panel equation 1.16 is plotted. Notice that the impedance of a capacitor is purely imaginary. In the center panel the phase angle of the impedance of a capacitor is shown. Notice that it is -90 degrees for all frequencies, as show in equation 1.28. In the right panel equation 1.29 is shown. Again, in the high frequency limit the impedance of a capacitor approaches zero, while in the low frequency limit the impedance diverges. In the low frequency limit the capacitor acts as an open, or break in the circuit. 12

1.7. All three figures above are representative of resistor in series with a capacitor, using 50 frequency points ranging from 0.1 Hz to 1 MHz along with a 0.1 mF capacitor and a 1000 Ohm resistor. Left panel equation 1.36 is shown. Notice this is identical to figure 1.6 except shifted along the real axis by 1000 Ohms. The phase angle of the impedance, equation 1.37 is shown in the center panel. Notice at high frequencies the phase angle approaches zero degrees. This is true since at this limit the impedance of a capacitor approaches zero and will act as a short. Thus the phase angle will only be affected by the resistor, which will not affect the phase angle. At low frequencies the impedance of a capacitor will approach infinity, and act as an open, not allowing for a current path in the system. Since there is no current in the system there will be no voltage drop across the resistor, and only the capacitor will affect the phase angle of the impedance, thus the overall phase angle of the impedance will approach -90 degrees. 14

1.8. The figure above is representative of a R || C circuit, using 50 frequency points ranging from 0.1 Hz to 1 MHz along with a 0.1 mF capacitor and a 100 Ohm resistor. Here the negative of the imaginary part of the impedance of an R || C circuit, equation 1.45 is plotted vs. frequency. This shows the peak frequency of an R || C circuit is located at the inverse of the circuit's time constant, see equation 1.46. Notice at the location of the peak frequency the imaginary impedance is 50 Ohms, or R/2. 16

1.9. The above figures are representative of an $\mathrm{R_a} \parallel \mathrm{C_a} + \mathrm{R_b} \parallel \mathrm{C_b}$ circuit, using 50 frequency points ranging from 0.1 Hz to 1 MHz with $R_a = 100\ Ohm$, $C_a = 10\ \mu F$, $R_b = 400\ Ohm$, and $C_b = 10\ mF$. In the left panel equation 1.47 is plotted. The right panel shows the negative of the imaginary part of the impedance of an $\mathrm{R_a} \parallel \mathrm{C_a} + \mathrm{R_b} \parallel \mathrm{C_b}$ circuit, equation 1.48 is plotted vs. frequency. Here two peaks are visible at two different frequencies. The inverse of these frequencies are the time constants of the R $\parallel$ C circuits. 17

1.10. The above figures are representative of five R $\parallel$ C circuits in series. equation 1.49 is shown in the left figure with n=5. In the right panel equation 1.50, with n=5, is plotted vs. frequency. Here five peaks are visible at five different frequencies. As the above figures indicate as the impedance spectrum becomes more complex more and more circuit elements are needed to fit the data. 18

1.11. The figure above is representative of an $R \parallel C$ circuit, using 50 frequency points ranging from 0.1 Hz to 1 MHz. equation 1.18 is plotted while using equation 1.57 for the capacitance in the impedance of a capacitor equation 1.16. The parameters used are L=6 μm, r=25 nm, ϵ_r=3, and κ=1,2,5,10 S/m, red, green, blue, black respectively. 20

2.1. The above figure shows a schematic of the nanocapillary geometry with length L, center radius r_1 and opening radius, r_0. In addition to this there is a constant radii center section of length fL. The model is symmetrically presented, such that the variable radius and double-layer capacitance of the nanocapillary is accounted for by a differential equivalent circuit shown in the top panel. In the text a discussion of how the differential equation will be developed from the above figure, including discussion on boundary conditions and limits on the solution to the differential equation. 28

2.2. Above the negative imaginary component of the equation 2.6 for a fixed R_{cyl} is shown. This gives different peak frequencies depending on the nanocapillary cylindrical aspect ratio r/L. The aspect ratios labeled in the figure are relative to the reference geometry of L =6 μm , r =5 nm with $\kappa_{\text{c}} = 0.4$ S/m, $\widetilde{C}_{\text{c}} = 1.5$ mF/m^2. Plotting this as a standard Nyquist plot will only show a shift in the peak frequency, which is fairly difficult to distinguish from one plot to another. 31

2.3. The effect of constriction of the openings of cylindrical nanocapillaries on the EIS spectrum is shown by plotting 2.12 for different ratios of the radii as shown in the figure legend. Each of the four nano-capillaries has the same DC resistance and would in principle give identical current-voltage curves in spite of having vastly different shapes. The EIS shows a clear change with nanocapillary geometry. The parameters used are L=6 μm, r_1=5 nm, κ_{c}=0.4 S/m, $\widetilde{C}_{\text{c}}$=1.5 mF/m^2. The inset shows renderings of the nanocapillary shapes corresponding to the radii ratios labeled in the figure. 33

2.4. Here a figure of the experimental setup is presented, with gold counter electrodes, Ag/AgCl reference electrodes, the polycarbonate membrane, PDMS cylinders, and ABS support chamber clearly shown. Image created using Pro-E computer aided design software. 35

2.5. Here a figure of the device is presented. The gold counter electrodes and the Ag/AgCl reference electrodes are connected to a Gamry Instruments Reference 600 potentiostat. The purpose of the gold counter electrodes is to apply the field, while the reference electrodes measures the potential difference across the membrane. 36

2.6. Notice this most basic model, using a single resistor to fit the nanocapillary equation 2.25 performs terribly, with a reduced chi squared of about 4500. The only feature the model can obtain is the DC limit. With bulk specific conductivities [S/m] of 1.093, 0.617, 0.342, 0.238, 0.136, purple, blue, green orange, red, respectively. 39

2.7. Modeling the nanocapillary with Z_{cyl}, equation 2.26 improves the fit with a reduced chi squared of 500 and is a 9 times improvement over equation 2.25. However, the model still does not capture the degree of suppression at the peak of the spectrum. With bulk specific conductivities [S/m] of 1.093, 0.617, 0.342, 0.238, 0.136, purple, blue, green orange, red, respectively. 40

2.8. Modeling the nanocapillary with Z_{loz}, equation 2.27 improves the fit with a reduced chi squared of 61 and is a 9 times improvement over equation 2.26. The model accurately produces all the features of the data, however the still seemingly large reduced chi squared indicates that there is still improvements to the fit to be made. With bulk specific conductivities [S/m] of 1.093, 0.617, 0.342, 0.238, 0.136, purple, blue, green orange, red, respectively. 41

2.9. Panel A shows markers for experimental EIS data on a NCAM at 5 different concentrations of phosphate buffered NaCl that give conductivities as indicated in the figure ledgend. Panel B shows the response of the cell and instrument for the same solution conditions. Panel C shows the response of just the membrane obtained by the subtraction of the instrument response from the data. Local fits using 2.24, 2.20 and their difference are shown as solid lines in panels A, B, and C, respectively. . 42

2.10. Fits using active set are shown above. With bulk specific conductivities [S/m] of 1.093, 0.617, 0.342, 0.238, 0.136, purple, blue, green orange, red, respectively. 43

2.11. Local fit parameters were plotted in combination (points) to obtain the global dependence (fit lines) of nanocapillary parameters as discussed in the text. Error bars were propagated from the standard errors from the fit parameters. Panel A shows the capillary conductivity vs. the bulk conductivity. A linear dependence is found with a constant offset to account for surface charge counter ions in the nanocapillary. Panel B shows the ratio of the radii, r_1/r_0. Panel C shows the fraction, f, of the length, L, of the capillary that is cylindrical. Panel D shows the capillary double-layer differential capacitance and a fit to a square root power law. 45

3.1. Figure above shows an unfolded and elongated protein traversing the nanopore. Each colored sphere on the protein is an amino acid. As the protein passes though the nanopore the groupings of amino acids will be sampled. The amount of excluded volume and surface charge density within each grouping will effect the overall impedance. The goal of this study is to determine the impedance of a protein within a nanopore and propose a method to rapidly sequence a protein. 56

3.2. Here the EIS spectrum of a protein, modeled as a cylinder, within a nanopore is shown. Both figures show plots of 3.13 with L =60 nm, $\mathrm{r_n}$ =10 nm, $\mathrm{r_s}$ = 100 μm, κ = 0.5 S/m, $\widetilde{C}_\mathrm{n}$ = 1 mF/m^2, $\widetilde{C}_\mathrm{p}$ = 10 mF/m^2, and ϵ_s = 6, with $\mathrm{r_p}$ =0 nm, 5 nm, 9 nm, 9.5 nm, 9.9 nm, 9.99 nm, 9.999 nm, and 9.9999 nm, colored black, red, purple, green, orange, cyan, magenta, blue respectively. In the limit the radius of the protein is equal to that of the nanopore, the signal is that of an ideal capacitor. 60

3.3. The negative imaginary component of equation 3.13 is shown with L=60 nm, r_{n} =4 nm, r_{p} =1.5 nm, this is the radius of an unfold protein, r_{s} =40 nm, κ_{n} = 0.1 S/m, the experimentally determined[15] nanopore double layer differential capacitance $\widetilde{C}_{\mathrm{n}}$ = 1 mF/m^2, the calculated protein double layer differential capacitance $\widetilde{C}_{\mathrm{p}} = 0.1\alpha$ F/m^2, the dielectric constant of the substrate, assuming silicon nitride, $\epsilon_{\mathrm{s}} = 6$, and α = 1,2,5,10, blue, red, yellow, green, respectively. These parameters have been chosen to accentuate the effect of the double layer differential capacitance on the surface of the protein. However, one of the parameters the radius of the substrate, $\mathrm{r_s}$ =50 nm is rather small. The intension is to minimize the capacitance from the substrate so that it does not mask the signal from the capacitance of the double layer of the protein. However, the means that experimentally the nanopore can only be contained in a substrate with a radius of about 50 nm, otherwise the difference in surface charge density from region to region on the protein will not be distinguishable. If one would increase the radius of the substrate to r_{s} =200 nm then the capacitance of the substrate would mask the signal from the protein as shown in the right panel. Other than changing the radius of the substrate the left and right panels are identically calculated. 61

3.4. The left panel shows the excluded volume for alpha synuclein is shown as a function of the number of amino acids traversed. A protein is composed of numerous amino acids, in the case of alpha synuclein, 140. The shorter the nanopore the more the excluded volume structure is visable. Note that in both panels the zero point is where there are 25 amino acids in the nanopore. The average value of the length of an amino acid is about 0.38 nm. Using a nanopore with an equivalent length of 25 amino acids is about 9.5 nm long. The center panel shows the sum of the charge on the amino acids in the nanopore. The right panel shows the peak frequency for alpha synuclein as a function of the number of amino acids that have traversed the nanopore. Notice at the end points the function seems to diverge. This is due to the short pore used L =9.5 nm. With no protein in the nanopore the time constant is small yielding a large peak frequency. As the double-layer differential capacitance in the nanopore from the protein increases the time constant also increase, thus decreasing the peak frquency. The peak frequency rises again near the center of the figure do to the lack of surface charge density in the central region of alpha synuclein. The protein double layer differential capacitance, which was calculated using equations 3.31 and 3.32. This value was the used to calculate the time constant of the system equation 3.7b, which was then used to calculate the peak frequency, equation 3.10. Notice the time constant of the system with the protein in the nanopore equation 3.7b is a function of the radius of the protein. The radii where calculated by assuming a cylindrical volume with the average length of each amino acid. Then the average value of the radii of the amino acids in the nanopore at a given time was used. Values used include: $\mathrm{r_n}$ =4 nm, $\widetilde{C}_\mathrm{n} = 1$ mF/m^2, T=297 K, with 100 mM KCl yielding a solution conductivity of $\kappa =$ 1.19 S/m. A solution dielectric constant of $\epsilon_\mathrm{s} = 80$ used. 68

4.1. Here equation 4.6 is plotted with $L_{\mathrm{n}} = 200$ nm, $r_0 = 60$ nm, $r_1 = 150$ nm, $\widetilde{C}_{\mathrm{n}} = 1$ mF/m^2, $\kappa_0 = 0.136$ S/m, and bulk conductivities of 9.68, 5.37, 2.29, 1.19 S/m, green, red, blue, purple, respectively. The nanopore differential capacitance $\widetilde{C}_{\mathrm{n}}$ was determined previously.[14] The capacitance of the chip, C_{chip}=747 pF was calculated using equation 4.7 with the dielectric constant, ϵ_{r} of silicon nitride being 7, the thickness of the chip t=200 nm, and the area A of the chip being 2.25μm^2. This gives a theoretical expectation of the nanopore impedance with reasonable parameters. 76

4.2. Above the EIS data at four different concentrations of phosphate-buffered KCl is shown. The left panel shows the run to run variability. EIS was performed three times at each of the four concentrations. The right panel shows the average of these along with fits to equation 4.6 with fit parameters shown in Table 4.1. 77

4.3. Above the EIS data scaled by the pore conductivity is shown, that is both the real and imaginary portions of the EIS spectrum are multiplied by their respective pore conductivity. The net effect is for all the DC limits to be the same. With this scaling one can directly see the effect of the EDL on the impedance. At higher conductivities the capacitance of the EDL is larger thus the deviation from and ideal RC circuit would be larger, in this case causing a decrease in the imaginary impedance at the peak frequency. Where again the bulk conductivities are 9.68, 5.37, 2.29, 1.19 S/m, green, red, blue, purple, respectively. 78

4.4. Panel A shows the DC limit plotted vs. the bulk conductivity, which is fit to 4.8. From this the nano-pore conductivity offset is obtained that is $\kappa_0 = 0.136$. The center figure shows the ratio of the time constants equation 4.5 and fit to a constant of 3.39. That is $r_1 = 3.39r_0$. In the right panel, the scaled double-layer differential capacitance is shown. The combinations of fit parameters reveals a function form consistent with that of a constant capacitive stern layer and a capacitive Gouy-Chapman layer, depending on the square root of the solution conductivity, all in series. With $\widetilde{A}_{\mathrm{S}}$=1.4±0.18 μF$m^{-1/2}$ and $\widetilde{B}_{\mathrm{GC}}$=0.98±0.18 μF$S^{-1/2}$. Error bars were propagated from the standard errors in the fit parameters. . . 79

5.1. Above shows the effect of the DC bias on a NCAM, where the left panel shows the EIS data with background, while the right panel shows the EIS data with the background subtracted. Equation 2.24 was used to fit the EIS data. During fitting the geometric parameters, as indicated in table 2.7 were fixed, while conductivity within the pore and the double-layer differential capacitance were allowed to float. These fits seem deceptively promising, however upon close investigation of the low frequency part of the spectrum one sees that the model completely fails to capture these inductive hooks. This close up is shown in figure 5.2. In all cases, red, orange, brown, cyan, magenta, purple represent, 500, 400, 300, 200, 100, 0 mV DC bias. 86

5.2. Here, a close up of the low frequency spectrum is presented, where the left panel shows the EIS data with background, while the right panel shows the EIS data with the background subtracted. Notice the model equation 2.24 completely fails to capture the low frequency features in the data. There is no element in the model that would produce positive imaginary features, thus a new model is required. Again, red, orange, brown, cyan, magenta, purple represent, 500, 400, 300, 200, 100, 0 mV DC bias. 87

5.3. Here, a close up of the low frequency spectrum is presented, where the left panel shows the EIS data with background, while the right panel shows the EIS data with the background subtracted. Notice the model equation 5.1 captures the low frequency features in the data. Again, red, orange, brown, cyan, magenta, purple represent, 500, 400, 300, 200, 100, 0 mV DC bias. 88

B.1. Here the electrical double layer is shown. It is partitioned into the in Stern layer, the more diffuse Gouy-Chapman layer, and the bulk. The Stern layer is composed of solvated counter-ions, while the Gouy-chapman layer is mixture of solvated counter-ions and solvated species of the same valency a the surface. As one moves further from the surface concentration of counter-ions in the Gouy-Chapman layer falls and the concentration of oppositely charged species increases until one reaches the bulk where net neutrality occurs. 98

D.1. Here EIS data is shown for what appears to be the clogging of a nanopore. Although millipore water was used, possible dust and other particulates could have been in the dry buffer and KCl, which would clog the nanopore. During each subsequent run the clogging seems to increase. The nanopore is essentially acting as a filter. Each run is performed identically, from black to orange, as explained in the text. 105

D.2. Left panel shows the run to run variability in the EIS spectrum, while the right panel is the average of the three runs. Simply by inspecting the EIS data on can see that the peak frequency is low indicating a large double-layer differential capacitance, large chip capacitance or a combination of both. With bulk conductivities of 9.68, 5.37, 2.29, 1.19 S/m, green, red, blue, purple, respectively. 106

D.3. Left panel shows unequilibrated single nanopore EIS spectra on chip 88728-89133. The right panel shows unequilibrated FIB EIS spectra on chip 88671. There is also a possibility that that the fib was not completely hydrated. That EIS data presented in chapter 6 is on the same chip as that presented in the right panel. 107

D.4. Left panel shows the EIS of a NCAM. The test solution, a 1.0 M KCl, 10 mM sodium phosphate buffered solution is unchanged from run to run. However, as time progresses the EIS spectrum tends towards lower impedance. As time progresses the nano-capillaries are hydrated and their surface charge density is neutralized, drawing in excess counter-ions. The right panel shows the DC limit as a function of time, which is then fit to an exponential decay, equation D.1. This shows that 48 hours is a minimum amount of time required to properly equilibrate the NCAMs. 107

Chapter 1

Introduction

1.1 Overview

Nanocapillaries find increasing use in a variety of applications including, protein translocation dynamics [1, 2, 3], DNA sequencing[4, 5], for ion-channel studies[6, 7, 8, 9, 10, 4, 11] and for single molecule sensing[12, 13]. In addition to this, commercially available nanocapillary array membranes[14, 15] (NCAMs) have been used for nanofabrication templates[16, 17], for fundamental studies of ionic flow at the nanoscale[18, 19], permselectivity[20], and for studies on transport regimes as a function of radii[19]. All of these applications are affected by the surface properties and geometry of the nanopores or nanocapillaries. Thus, a method to determine the surface properties and geometry of nanopores and nanocapillaries is essential to the understanding of the above phenomena.

One type of method to determine the geometry of these nanopores or nanocapillaries is electron microscopy, which can image the geometry[21, 22, 23]. However, electron microscopy does not reveal any information about the surface properties. In addition to this, these methods often require a great deal of sample prep and may render the sample unusable for future purposes. Current-voltage measurements[24, 25, 26] give information on the surface properties of the sample, possibly surface-charge rectification, but do not give any direct information about the geometry. Although, if one has a cylindrical capillary and knows the length, while assuming no surface-charge rectification, then one can obtain the radius of this capillary.

In contrast to a DC measurment, electrochemical impedance spectroscopy or EIS[27, 28, 29] measures the impedance, complex resistance, as a function of frequency of applied AC potential. Since the EIS signal is a measure of the electrokinetic transport of ionic solution through the nanocapillaries, it is sensitive to their geometry and surface electrical properties[30, 31]. Equivalent circuit modeling is a standard approach to fitting EIS data[32, 33]. $R \parallel C$ equivalent circuit modeling has been applied to NCAMs,[34, 35, 36, 37, 15] during which attempts were made to extract the double-layer differential capacitance and geometric parameters from these $R \parallel C$ circuits. However, multiple $R \parallel C$ circuits can fit the same EIS data, with varying degree of accuracy, and thus as one would use more and more of these $R \parallel C$ circuits to try to reduce the error in the fit. Thus one would want to minimize the number of circuit elements to extract the relevant properties while minimizing the reduced chi square. In addition to this, authors have often assigned capacitance elements as parasitic or stray capacitance, without any justification for what it may actually be. Chien et al.[38] uses a constant phase element (CPE) to model a nanopore. The CPE is an empirical circuit that applies a constant phase change to an $R \parallel C$ circuit response. Chien et al.[38] interprets the DC impedance in terms of the conical resistivity of an electrolytic resistor. In addition to this element they have a resistor in series to account for ionic diffusion. In effect the use of EIS in this application served only to give the DC current at a given voltage bias.

In the following chapters an equivalent circuit element will be developed to obtain the nanopore or nanocapillary geometry and double-layer differential capacitance. This will be accomplished by arranging resistors and capacitors in a arrangement similar to the transmission line model[39, 40, 41]. Then discretizing and transforming this arrangement into a differential equation. Then solving this for the overall impedance, with a boundary condition such that the impedance of the nanopore is zero when the length of the nanocapillary is zero. The model is then modified to allow for protein sequencing by essentially inserting a charged cylinder into the model and measuring the impedance, piecewise, as a function of charged region. Lastly, a differential capacitance model is presented that is a function of the surface charge density for cylindrical and spherically symmetric systems. From this differential capacitance model a zeta potential model[42, 43, 44, 45] is obtained. Coupling this with the above mentioned models allows one to directly sequence or predict the impedance of a protein as a function of charged region. However, before this is accomplished an overview of circuit theory and electrical impedance is presented.

1.2 Circuit Theory

In this section an overview of circuit theory and electrical impedance is presented. Specific examples and discussion are directed towards chemical impedance spectroscopy. Circuit theory is first developed including Kirchhoff's laws and definitions of conservation of energy and charge in electric circuits. From these definitions equivalent circuits for series and parallel resistors and capacitors are developed. These are then used in conjunction with a discussion on electrical impedance to show various types of circuits and their frequency dependent spectrums. Lastly, peak frequency formalism is developed and representations of impedance spectra in terms of a distribution of time constants is shown.

Kirchhoff's voltage law (KVL), and Kirchhoff's current law (KCL) are the basis for circuit theory. KVL expresses conservation of energy in circuits, while KCL express conservation of charge. From KCL one finds that the sum of the charge entering and exiting a node, a junction of two or more circuit elements, is zero. Thus the sum of the currents at a node is zero. That is, the current entering a node is equal to that of current leaving the node.

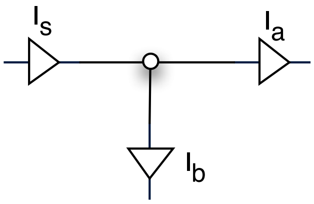

Figure 1.1: Here an application of KCL is shown, where the current entering the node is equal to the current leaving the node.

From KCL and figure 1.1 one sees that:

$$I_{\mathrm{s}} = I_{\mathrm{a}} + I_{\mathrm{b}} \tag{1.1}$$

From KVL one finds that when a charge traverses a loop in a circuit it does not gain or lose energy. At points in the loop it may absorb energy from one or more elements, but then must donate that energy to other elements before completing the loop. From KVL and figure 1.2 one sees:

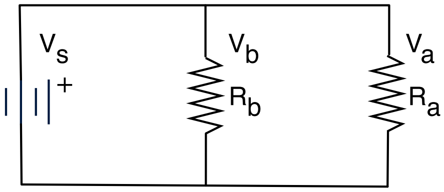

Figure 1.2: Here an application of KVL is shown. The voltage drop across each of the resistors is equal to that of the voltage source.

$$V_{\mathrm{s}} = V_{\mathrm{a}} = V_{\mathrm{b}} \tag{1.2}$$

The charge absorbs energy from the potential source, and donates it to either of the resistive elements. From ohms law, $V = IR$, and from equation 1.1 and equation 1.2, one sees that for resistors parallel:

$$R_{\mathrm{a}} \parallel R_{\mathrm{b}} = \frac{1}{1/R_{\mathrm{a}} + 1/R_{\mathrm{b}}} \tag{1.3}$$

For resistors in series the current through them is the same and the sum of the voltage drop across them is equal to the voltage source. This leads to resistors in series being additive.

However, capacitors obey opposite addition rules. The charge stored on a capacitor q, is equal to the capacitance C, times the voltage across the capacitor V_{c}. That is $q = CV_{\mathrm{c}}$. Since $i = \frac{dq}{dt}$, we have:

$$i(t) = C\frac{dV_{\mathrm{c}}}{dt} \tag{1.4}$$

or

$$V_{\mathrm{c}} = \frac{1}{C}\int i dt \tag{1.5}$$

For capacitors in series, the sum of the voltage drop across them is equal to that of the voltage source, along with the current through them being the same leads to:

$$V_{\mathrm{s}} = V_1 + V_2 = \frac{1}{C_1}\int idt + \frac{1}{C_2}\int idt = \frac{1}{C_{\mathrm{eq}}}\int idt \tag{1.6}$$

Thus:

$$C_{\mathrm{eq}} = \frac{1}{1/C_1 + 1/C_2} \quad (series \quad capacitors) \tag{1.7}$$

For capacitors in parallel the sum of the current across them is equal to the source current, and the voltage drop across them is equal to the source voltage:

$$I_{\mathrm{s}} = I_1 + I_2 = C_1\frac{dV_{\mathrm{s}}}{dt} + C_2\frac{dV_{\mathrm{s}}}{dt} = C_{\mathrm{eq}}\frac{dV_{\mathrm{s}}}{dt} \tag{1.8}$$

Therefore:

$$C_{\mathrm{eq}} = C_1 + C_2 \quad (parallel \quad capacitors) \tag{1.9}$$

An interesting example of a combination of circuit elements is a ladder circuit, see figure 1.3. The ladder circuit is composed of an infinite series of identical resistors. To find the equivalent resistance for this collection of elements split off the first resistor and add that in series to the second resistor in parallel to the rest of the ladder, while setting this equal to the entire ladder:

$$R_{\mathrm{eq}} = R + R \parallel R_{\mathrm{eq}} \tag{1.10}$$

Solving for R_{eq} yields:

$$R_{\mathrm{eq}} = \frac{1}{2}(R + \sqrt{5}R) \quad (ladder\ circuit) \tag{1.11}$$

This is approximately 1.62R. In this derivation we exploited a property of infinity, in that splitting off an element from a collection of infinitely many symmetric elements still leaves infinity many of these elements.

Using the above material one can analyze most any electrical circuit. However, as the number of circuits increases and the functionality of the voltage source becomes more complicated, say from a static source to a time dependent source, the standard

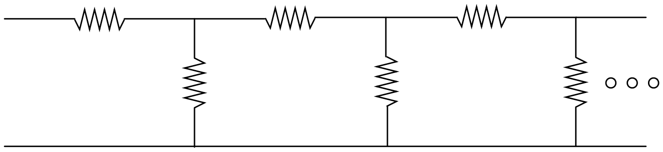

Figure 1.3: An infinite series of resistors each with resistance R is shown. By summing the resistors an equivalent resistance of approximately 1.62R is found.

---

methods of setting up and solving the differential equations involved becomes increasingly formidable. In addition to this, it often the case that one is not entirely interested in the time dependent properties of the circuit, but possibly the frequency dependent properties of the circuit.

1.3 Electrical Impedance

As mentioned above, often systems are exposed to time dependent sources. Analyzing the response of the system due to these time dependent sources may involve solving complicated differential equations. A simpler approach is to the transform the differential equation to the frequency domain, solve the now algebraic equation, then return to the time domain. One may also remain in the frequency domain if time dependent properties are not desired.

First consider a voltage source with the form:

$$V_{\mathrm{s}}(t) = V_{\mathrm{s}} e^{i(\omega t + \phi)} \tag{1.12}$$

It is more standard to use a voltage source of the cosine form, however this form will illuminate the results more clearly. Consider applying this across a resistor, with resistance R. Using Ohm's law one finds the current though the resistor to be:

$$I_{\mathrm{R}}(t) = V_{\mathrm{s}} e^{i(\omega t + \phi)}/R \tag{1.13}$$

Defining the impedance, complex resistance, as the ratio of the voltage over the current, due to the frequency dependent excitation one finds:

$$Z_R = V_R(t)/I_R(t) = R \tag{1.14}$$

An ideal resistor will have impedance R, and no frequency dependance. Now consider this voltage across a capacitor. Recalling equation 1.4, one finds the current to be:

$$I_{\mathrm{C}}(t) = i\omega C V_{\mathrm{s}} e^{i(\omega t+\phi)} \tag{1.15}$$

Again taking the ratio of the voltage and current one find the impedance of a capacitor to be:

$$Z_{\mathrm{C}} = \frac{1}{i\omega C} \tag{1.16}$$

Notice in these two cases the time dependance has been eliminated. We are now in the frequency domain.

1.3.1 R || C Circuits

Next, consider a system with a resistor and capacitor in parallel. While analyzing this system in the frequency domain one can add the impedances of these elements as if they were resistors. By using equation 1.3, and the results obtained for the impedance of a resistor and the impedance of a capacitor, one finds:

$$Z_{\mathrm{R}} \parallel Z_{\mathrm{C}} = \frac{1}{1/R + i\omega C} \tag{1.17}$$

Which can be decomposed into its real and imaginary components:

$$Z_{\mathrm{R}} \parallel Z_{\mathrm{C}} = \frac{R}{1+\omega^2 C^2 R^2} - i\frac{\omega C R^2}{1+\omega^2 C^2 R^2} \tag{1.18}$$

with limits

$$\lim_{\omega\to 0} Z_{\mathrm{R}} \parallel Z_{\mathrm{C}} = R \tag{1.19}$$

and

$$\lim_{\omega\to\infty} Z_{\mathrm{R}} \parallel Z_{\mathrm{C}} = 0 \tag{1.20}$$

Physically, in the low frequency limit, as the frequency approaches zero, the impedance of the capacitor approaches infinity. As this happens the path of the current follows the resistor thus would yield an impedance of R. In addition to this a resistor will not affect the phase angle of the current relative to the applied potential. Thus at the low frequency limit the phase angle of the impedance approaches zero. However, in the high frequency limit, as the frequency approaches infinity, the impedance of the capacitor approaches zero, thus the current will follow the path through capacitor yielding an overall impedance of zero. At this limit the phase angle of the impedance approaches -$\pi/2$. Notice the phase angle of the impedance of an $R \parallel C$ circuit is:

$$\phi_{\mathrm{R}\parallel\mathrm{C}} = \tan^{-1}(\mathrm{Im}[Z]/\mathrm{Re}[Z]) = \tan^{-1}(-RC\omega) \tag{1.21}$$

with limits

$$\lim_{\omega\to 0} \phi_{\mathrm{R}\parallel\mathrm{C}} = 0 \tag{1.22}$$

and

$$\lim_{\omega\to\infty} \phi_{\mathrm{R}\parallel\mathrm{C}} = -\pi/2 \tag{1.23}$$

The left panel of figure 1.4 show a Nyquist, or Cole-Cole, plot of equation 1.18. A Nyquist plot plots the real portion of the impedance vs. the imaginary, often negative imaginary, portion of the impedance. The center panel of figure 1.4 shows the phase angle vs. frequency plot of equation 1.21, while the right panel of figure 1.4 shows the magnitude vs. frequency plot. Bode plots would be a plot where both the phase angle and magnitude are represented on the same plot.

1.3.2 R + R ∥ C Circuits

A simple extension to an R ∥ C is to add a resistor in series to this, possibly for the resistance of the fluid between the electrodes:

$$Z_{\mathrm{R_{sln}}} + Z_{\mathrm{R}} \parallel Z_{\mathrm{C}} = R_{\mathrm{sln}} + \frac{R}{1+\omega^2C^2R^2} - i\frac{\omega C R^2}{1+\omega^2C^2R^2} \tag{1.24}$$

with limits

$$\lim_{\omega\to 0}(Z_{R_{\mathrm{sln}}} + Z_{\mathrm{R}} \parallel Z_{\mathrm{C}}) = R_{\mathrm{sln}} + R \tag{1.25}$$

and

$$\lim_{\omega\to\infty}(Z_{\mathrm{R_{sln}}} + Z_{R} \parallel Z_{\mathrm{C}}) = R_{\mathrm{sln}} \tag{1.26}$$

figure 1.5 show a plot of equation 1.24, and discussion.

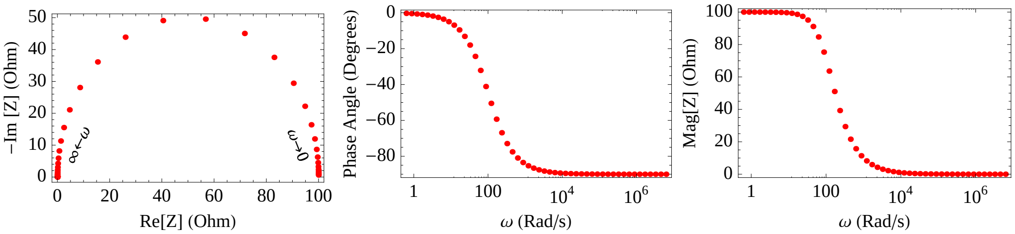

Figure 1.4: All three figures above are representative of an $R \parallel C$ circuit, using 50 frequency points ranging from 0.1 Hz to 1 MHz along with a 100 Ohm resistor and a 0.1 mF capacitor. Left panel equation 1.18 is plotted, while in the center panel equation 1.21 is shown. Notice the phase angle approaches zero as the frequency approaches zero, while the phase angle approaches -90 degrees in the high frequency limit. Right panel the magnitude of equation 1.18 is plotted. Notice in the DC limit, the zero frequency limit the magnitude of the impedance is that of the resistor. This is true since the impedance of the capacitor will approach infinity in the low frequency limit. Thus the current will follow the path of the resistor. On the other hand, at the high frequency limit the impedance of the capacitor will approach zero and the current path will follow that of the capacitor, yielding a zero impedance.

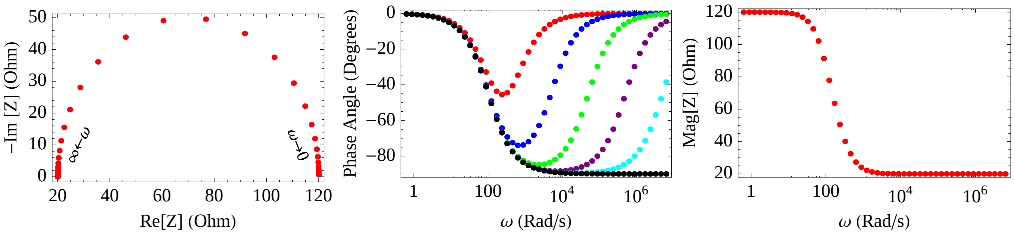

Figure 1.5: All three figures above are representative of an $R + R \parallel C$ circuit, using 50 frequency points ranging from 0.1 Hz to 1 MHz along with a 100 Ohm resistor, a 0.1 mF capacitor, and R_{sln}=20 Ohms. Left panel equation 1.24 is plotted. Notice the only difference between the Nyquist plots in figure 1.4 and figure 1.5 is that figure 1.5 is offset by an addition 20 ohms vs that of figure 1.4. This is also true for the magnitude of impedance figures. The phase angle is plotted with six different values for R_{sln}. These being 20, 2, 0.2, 0.02, 0.002, and 0 ohms, red, blue, green, purple, cyan, and black respectively. Notice the 0 ohm plot, the black plot, is identical to that of figure 1.4.

1.3.3 Purely capacitive circuit elements

In this section we will consider the impedance of a purely capacitive[27, 46] element. Physically the time dependance of a purely capacitive system is somewhat uninteresting, since the only element being the capacitor thus the voltage across it is equal to that of the source. The impedance of a capacitor was found earlier, see equation 1.16, and shown in the left panel of figure 1.6.

To obtain the phase angle of the impedance of a capacitor one needs the imaginary component of equation 1.16

$$\mathrm{Im}[Z_{\mathrm{C}}] = \mathrm{Im}[\frac{1}{i\omega C}] = \mathrm{Im}[\frac{-i}{\omega C}] = \frac{-1}{\omega C} \tag{1.27}$$

The sole purpose of this is to not forget the negative sign. While the real component of the impedance of a capacitor is zero. Thus the ratio of the imaginary component to the real component is negative infinity for all frequency points. Thus for the phase angle of the impedance of a capacitor we have:

$$\phi_{\mathrm{C}} = \tan^{-1}\left(\frac{\mathrm{Im}[Z]}{\mathrm{Re}[Z]}\right) = \tan^{-1}(-\infty) = -\pi/2 \tag{1.28}$$

This is show in the center panel of figure 1.6. This was also shown in the high frequency limit for an $R \parallel C$ circuit. Recall in this limit the impedance of the capacitor approaches zero, thus the current follow the path of the capacitor and yields the same phase angle as in equation 1.28. While the magnitude of the impedance of the capacitor is

$$|Z_{\mathrm{c}}| = \frac{1}{\omega C} \tag{1.29}$$

Which is shown in the right panel of figure 1.6.

1.3.4 R+C Circuits

In this section, we consider the impedance of a resistor and capacitor in series along with a time domain analysis. Starting first with the time domain analysis using a constant voltage source V_{s}, with the voltage drop across the resistor being V_{r}, and the voltage across the capacitor being V_{c}, one finds:

$$V_{\mathrm{s}} = V_{\mathrm{r}} + V_{\mathrm{c}} \tag{1.30}$$

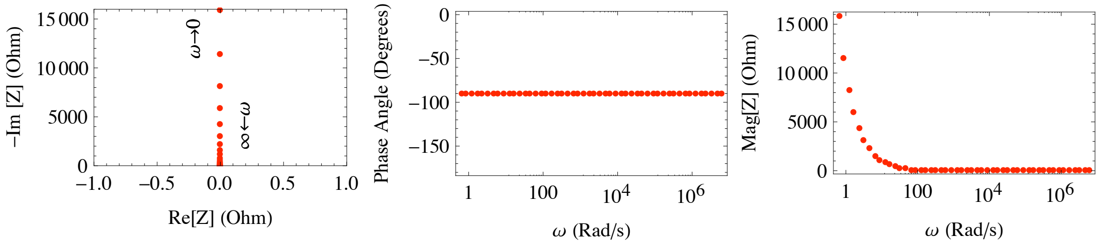

Figure 1.6: All three figures above are representative of a purely capacitive circuit element, using 50 frequency points ranging from 0.1 Hz to 1 MHz along with a 0.1 mF capacitor. Left panel equation 1.16 is plotted. Notice that the impedance of a capacitor is purely imaginary. In the center panel the phase angle of the impedance of a capacitor is shown. Notice that it is -90 degrees for all frequencies, as show in equation 1.28. In the right panel equation 1.29 is shown. Again, in the high frequency limit the impedance of a capacitor approaches zero, while in the low frequency limit the impedance diverges. In the low frequency limit the capacitor acts as an open, or break in the circuit.

Taking the time derivative of equation 1.30, while using ohm's law for the resistor and equation 1.4 for the derivative of the voltage across the capacitor yields:

$$0 = R\frac{di}{dt} + \frac{i}{C} \tag{1.31}$$

Integrating with respect to time yields:

$$i = Ae^{-t/RC} \tag{1.32}$$

where A is the constant of integration. Since these elements are in series the current across all the elements is the same. Integrating equation 1.32 with respect to time from zero to infinity yields the charge on the capacitor. If the capacitor is originally uncharged then $q(0) = 0$ and we have

$$\int_0^\infty idt = ARC = q(\infty) - q(0) = q(\infty) \tag{1.33}$$

However, the charge on the capacitor at a given time is equal to the capacitance times the voltage across the capacitor, thus

$$ARC = q(\infty) = CV_{\mathrm{c}}(\infty) = C(V_{\mathrm{s}}(\infty) - V_r(\infty)) \tag{1.34}$$

The current though the circuit approaches zero as time approaches infinity, thus the potential across the resistor approaches zero as time approaches infinity. Recalling that the potential V_{s} is constant in time, $V_{\mathrm{s}}(\infty) = V_{\mathrm{s}}$, the constant of integration A becomes V_{s}/R:

$$i = \frac{V_{\mathrm{s}}}{R} e^{-t/RC} \tag{1.35}$$

Initially there is no charge on the capacitor, and thus no potential drop; the capacitor will act as a short. As time evolves the charge increases on the capacitor until the potential across the capacitor equals that of the applied voltage, at this time the current flowing in the circuit is zero, the capacitor acts as an open. What is meant by charge on the capacitor is as follows. Consider two neutral conducting parallel plates connected to a voltage source. As time evolves the sum of the charges on the places will remain neutral, however one plate will gain positive charge while the other gains an equal amount of negative charge.

Unfortunately, this does not tell us about what we are interested in, the frequency dependance of these elements. To determine this one needs to replace the constant voltage source with a source that is both time and frequency dependent, then the impedance can be obtained by solving the differential equation and taking the ratio of the voltage and current. However, since we already know what the impedance of a resistor and capacitor are we can simply add them in series to obtain the circuit impedance:

$$Z_{\mathrm{R+C}} = R + \frac{1}{i\omega C} \tag{1.36}$$

The impedance of a resistor and capacitor in series is shown in the left panel in figure 1.7, while the phase angle:

$$\phi_{\mathrm{R+C}} = \tan^{-1}\left(\frac{\mathrm{Im}[Z]}{\mathrm{Re}[Z]}\right) = \tan^{-1}\left(\frac{-1}{RC\omega}\right) \tag{1.37}$$

is shown in the center panel of figure 1.7.

As the frequency approaches zero in equation 1.36 the impedance of the capacitor approaches infinity and acts as an open, blocking the current path. But, how does this physically happen? There is no flow of charge though a capacitor. That is, say

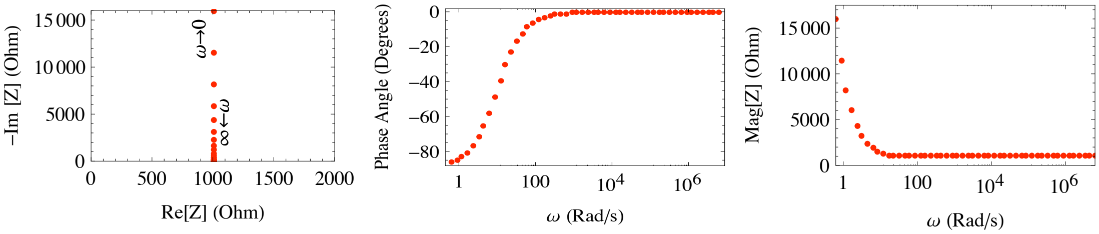

Figure 1.7: All three figures above are representative of resistor in series with a capacitor, using 50 frequency points ranging from 0.1 Hz to 1 MHz along with a 0.1 mF capacitor and a 1000 Ohm resistor. Left panel equation 1.36 is shown. Notice this is identical to figure 1.6 except shifted along the real axis by 1000 Ohms. The phase angle of the impedance, equation 1.37 is shown in the center panel. Notice at high frequencies the phase angle approaches zero degrees. This is true since at this limit the impedance of a capacitor approaches zero and will act as a short. Thus the phase angle will only be affected by the resistor, which will not affect the phase angle. At low frequencies the impedance of a capacitor will approach infinity, and act as an open, not allowing for a current path in the system. Since there is no current in the system there will be no voltage drop across the resistor, and only the capacitor will affect the phase angle of the impedance, thus the overall phase angle of the impedance will approach -90 degrees.

a negative charge appears on one side of the capacitor, then a negative charge will leave the opposite side. This build up of opposite charge will create a larger and larger electric field opposing the field applied by the voltage source until no further charge can be stored on the capacitor.

It is useful show how to obtain equation 1.36. Consider a time and frequency dependent voltage source:

$$V_{\rm s} = V_{\rm o} e^{i\omega t} \tag{1.38}$$

Using equation 1.30, ohm's law, and the current though a capacitor equation 1.4 yields:

$$V_{\rm s} = V_{\rm c} + RC\frac{dV_{\rm c}}{dt} = V_{\rm o} e^{i\omega t} \tag{1.39}$$

yields a voltage across the capacitor of

$$V_{\rm c} = \frac{V_{\rm o} e^{i\omega t}}{1 + iRC\omega} \tag{1.40}$$

It is interesting to look at various limits. First consider the limit as the resistance R across the resistor approaches zero. In this limit the voltage across the capacitor is equal to that of the source, for all time. Equivalently, as the capacitance of the capacitor approaches zero the capacitor acts as an open. Thus, no current can flow in the circuit, thus the current through the resistor is zero, thus the potential across the resistor is zero, thus the potential drop across the capacitor is equal to the source.

Using equation 1.4 one finds the current across the capacitor:

$$i_{\mathrm{c}} = \frac{Ci\omega V_{\mathrm{o}}e^{i\omega t}}{1 + iRC\omega} \tag{1.41}$$

Taking the ratio of equation 1.40 to equation 1.41 yields the impedance across the capacitor:

$$Z_{\mathrm{C}} = \frac{1}{i\omega C} \tag{1.42}$$

Which was found earlier equation 1.16. Adding 1.42 with the impedance across the resistor being R, yields equation 1.36.

Lastly, it is important to mention that equation 1.40 is not the full solution to the differential equation equation 1.39. It is only the in-homogenous solution, due to the voltage source. There is also the homogenous solution, the solution when the voltage source is zero, yielding a exponential in time, the constant of which is dependent on whether the capacitor is charged or not. The linear combination of these is the full solution to the differential equation. However, as mentioned earlier electrical impedance is the ratio of the voltage across the capacitor due to the frequency dependent voltage source to the frequency dependent current.

1.3.5 Constant Phase Element

One final circuit is a constant phase element (cpe) whoes impedance given by:

$$Z_{\mathrm{cpe}} = \frac{A}{(\omega i)^{n}} \tag{1.43}$$

where n is an integer and A is a constant. Notice when n = 0 the cpe acts as an ideal resistor, while it acts as an ideal capacitor when n = 1. Since

$$\frac{1}{i^{n}} = e^{-\pi n i/2} \tag{1.44}$$

the cpe will apply a constant phase of -$(90 * n)^{\circ}$ thus the name.

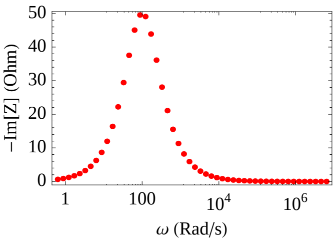

Figure 1.8: The figure above is representative of a R ∥ C circuit, using 50 frequency points ranging from 0.1 Hz to 1 MHz along with a 0.1 mF capacitor and a 100 Ohm resistor. Here the negative of the imaginary part of the impedance of an R ∥ C circuit, equation 1.45 is plotted vs. frequency. This shows the peak frequency of an R ∥ C circuit is located at the inverse of the circuit's time constant, see equation 1.46. Notice at the location of the peak frequency the imaginary impedance is 50 Ohms, or R/2.

1.4 Peak Frequency Optimization

In the previous section Nyquist and Bode plots have been shown. However, there is yet another way to display an impedance spectrum. By looking at the negative of the imaginary portion of the impedance one can pick out the peak frequency[47]. Consider the negative imaginary part of the impedance of an R ∥ C circuit:

$$-\mathrm{Im}(Z_{\mathrm{R}} \parallel Z_{\mathrm{C}}) = \frac{\omega C R^2}{1 + \omega^2 C^2 R^2} \tag{1.45}$$

Equation 1.45 is plotted in figure 1.8 vs. frequency. Notice there is a peak in the spectrum. This peak can be easily found by maximizing equation 1.45. While differentiating equation 1.45, setting this equal to zero, and solving for ω yields the peak frequency:

$$\omega_{\mathrm{peak}} = \frac{1}{RC} = \frac{1}{\tau} \tag{1.46}$$

For an R ∥ C circuit the peak frequency is equal to the inverse of the time constant. By looking at the zero frequency limit in the Nyquist plot one may obtain the resistance, R. Then by finding the peak frequency in the $-\mathrm{Im}(Z_{\mathrm{R}} \parallel Z_{\mathrm{C}})$ vs. frequency plot, one

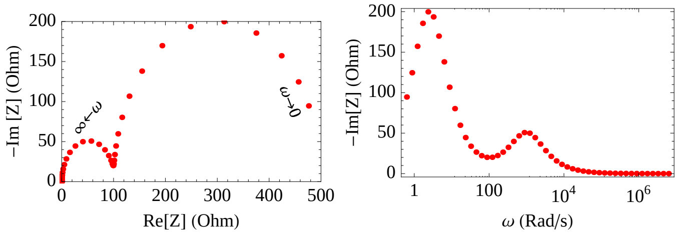

Figure 1.9: The above figures are representative of an $\mathrm{R_a} \parallel \mathrm{C_a} + \mathrm{R_b} \parallel \mathrm{C_b}$ circuit, using 50 frequency points ranging from 0.1 Hz to 1 MHz with $R_a = 100\ Ohm$, $C_a = 10\ \mu F$, $R_b = 400\ Ohm$, and $C_b = 10\ mF$. In the left panel equation 1.47 is plotted. The right panel shows the negative of the imaginary part of the impedance of an $\mathrm{R_a} \parallel \mathrm{C_a}+\mathrm{R_b} \parallel \mathrm{C_b}$ circuit, equation 1.48 is plotted vs. frequency. Here two peaks are visible at two different frequencies. The inverse of these frequencies are the time constants of the R ∥ C circuits.

---

maybe obtain the capacitance of the system, without doing any fitting, assuming the system may be idealized to an R ∥ C circuit. In addition to this putting the peak frequency back into equation 1.45 yields that magnitude of the imaginary portion of the impedance at the peak frequency; this being $R/2$.

For more complex systems one R ∥ C circuit will often not be sufficient. The next obvious extension would be to go to two R ∥ C circuits in series:

$$\begin{gathered} Z_{\mathrm{R}_a} \parallel Z_{\mathrm{C}_a} + Z_{\mathrm{R}_b} \parallel Z_{\mathrm{C}_b} = \\ \frac{R_a}{1+\omega^2 C_a^2 R_a^2} - i\frac{\omega C_a R_a^2}{1+\omega^2 C_a^2 R_a^2} + \frac{R_b}{1+\omega^2 C_b^2 R_b^2} - i\frac{\omega C_b R_b^2}{1+\omega^2 C_b^2 R_b^2} \end{gathered} \tag{1.47}$$

Taking the negative of the imaginary impedance of this yields:

$$-\mathrm{Im}(Z_{\mathrm{R}_a} \parallel Z_{\mathrm{C}_a} + Z_{\mathrm{R}_b} \parallel Z_{\mathrm{C}_b}) = \frac{\omega C_a R_a^2}{1+\omega^2 C_a^2 R_a^2} + \frac{\omega C_b R_b^2}{1+\omega^2 C_b^2 R_b^2} \tag{1.48}$$

Equation 1.47 and equation 1.48 are plotted in figure 1.9. Here one sees two time constants are needed. With two time constants the data is still fairly easily fit with two R ∥ C circuits. However, as the complexity of the impedance spectrum increases more and more R ∥ C circuits will be needed. In addition to this, it may become more difficult to properly fit the data with R ∥ C circuits.

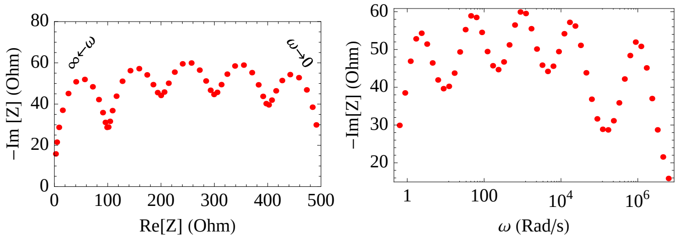

Figure 1.10: The above figures are representative of five R ∥ C circuits in series. equation 1.49 is shown in the left figure with n=5. In the right panel equation 1.50, with n=5, is plotted vs. frequency. Here five peaks are visible at five different frequencies. As the above figures indicate as the impedance spectrum becomes more complex more and more circuit elements are needed to fit the data.

One can extend equation 1.47 and equation 1.48 to n R ∥ C circuits:

$$\sum_i^n Z_{\mathrm{R}_i} \parallel Z_{\mathrm{C}_i} = \sum_i^n \frac{R_i}{1+\omega^2 C_i^2 R_i^2} - i\frac{\omega C_i R_i^2}{1+\omega^2 C_i^2 R_i^2} \tag{1.49}$$

$$-\mathrm{Im}(\sum_i^n Z_{\mathrm{R}_i} \parallel Z_{\mathrm{C}_i}) = \sum_i^n \frac{\omega C_i R_i^2}{1+\omega^2 C_i^2 R_i^2} \tag{1.50}$$

With limits:

$$\lim_{\omega\to 0} \sum_i^n Z_{\mathrm{R}_i} \parallel Z_{\mathrm{C}_i} = \sum_i^n R_i \tag{1.51}$$

$$\lim_{\omega\to\infty} \sum_i^n Z_{\mathrm{R}_i} \parallel Z_{\mathrm{C}_i} = 0 \tag{1.52}$$

$$\lim_{\omega\to 0} -\mathrm{Im}(\sum_i^n Z_{\mathrm{R}_i} \parallel Z_{\mathrm{C}_i}) = \lim_{\omega\to\infty} -\mathrm{Im}(\sum_i^n Z_{\mathrm{R}_i} \parallel Z_{\mathrm{C}_i}) = 0 \tag{1.53}$$

equation 1.49 and equation 1.50 are shown in figure 1.10 with n=5.

Lastly, instead of extracting resistances and capacitances from an impedance spectrum one can reformulate equation 1.49 and equation 1.50 to obtain a resistance and a time constant:

$$\sum_i^n Z_{\mathrm{R}_i} \parallel Z_{\mathrm{C}_i} = \sum_i^n \frac{R_i}{1+\omega^2 \tau_i^2} - i\frac{R_i \omega \tau_i}{1+\omega^2 \tau_i^2} \tag{1.54}$$

$$-\mathrm{Im}(\sum_{i}^{n} Z_{\mathrm{R}_i} \parallel Z_{\mathrm{C}_i}) = \sum_{i}^{n} \frac{R_i \omega \tau_i}{1 + \omega^2 \tau_i^2} \tag{1.55}$$

The advantage of this is that certain electrochemical processes may mimic the effect of capacitances, but may actually be something else. This formalism allows one to fit with $R \parallel C$ circuits and extract time constants which can be related to diffusion rates, for example.

1.5 System Modeling

The final component to this introduction is system modeling. Consider a cylindrically symmetric capillary in a substrate of uniform dielectric immersed in a conducting solution. The resistance of the conducting solution though the capillary is given by:

$$R_{\mathrm{sln}} = \frac{L}{\kappa \pi r^2} \tag{1.56}$$

where L is the length of the capillary, r is the radius of the capillary, and κ is the conductivity of the solution. Also, consider modeling the capacitance of the substrate using the parallel plate model:

$$C_{\mathrm{Pplate}} = \frac{\epsilon_0 \epsilon_r A}{L} \tag{1.57}$$

where ϵ_0 is the permittivity of free space, ϵ_r is the dielectric constant of the substrate, A is the surface area of the substrate, and L is the thickness of the substrate, here assumed to be the same as the length of the capillary thought the substrate. The impedance spectrum of this system can be found by modeling the system as an $R \parallel C$ circuit, equation 1.18 while using equation 1.57 for the capacitance in the impedance of a capacitor equation 1.16.

In figure 1.11 the effects of the solution dielectric and of the electrical double layer within the capillary were not included. The Gouy-Chapman model[48, 49] shows that the capacitance of the electrical double-layer is shown to have a square root dependance on the solution conductivity. Appendix A is dedicated to a derivation and discussion of this model.

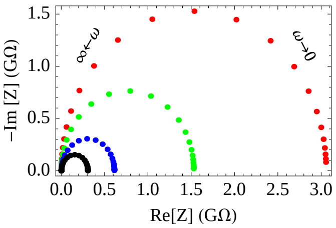

Figure 1.11: The figure above is representative of an $R \parallel C$ circuit, using 50 frequency points ranging from 0.1 Hz to 1 MHz. equation 1.18 is plotted while using equation 1.57 for the capacitance in the impedance of a capacitor equation 1.16. The parameters used are L=6 μm, r=25 nm, ϵ_r=3, and κ=1,2,5,10 S/m, red, green, blue, black respectively.

Now that the machinery has been put in place we are now able to use all of this to developed our model, the Variable Topology finite Warburg Impedance Model. One can also call this the Vitarelli Talaga finite Warburg Impedance Model or VTW.

Bibliography

[1] D.S. Talaga and J. Li. Single-molecule protein unfolding in solid state nanopores. *J. Am. Chem. Soc.*, 131:9287–9297, 2009.

[2] J. Li and D. S. Talaga. The distribution of dna translocation times in solid-state nanopores. *J. Phys. Condens. Mat.*, 22:454129, 2010.

[3] Z. Yang, S. Li, L. Zhang, A. Ur Rehman, and H. Liang. Translocation of alpha-helix chains through a nanopore. *J Chem. Phys.*, 133:154903, 2010.

[4] Cees. Dekker. Solid-state nanopores. *Nat. Nanotechnol.*, 2:209–215, 2007.

[5] Daniel Branton, David W. Deamer, Andre Marziali, Hagan Bayley, Steven A. Benner, Thomas Butler, Massimiliano Di Ventra, Slaven Garaj, Andrew Hibbs, Xiaohua Huang, Stevan B. Jovanovich, Predrag S. Krstic, Stuart Lindsay, Xinsheng Sean Ling, Carlos H. Mastrangelo, Amit Meller, John S. Oliver, Yuriy V. Pershin, J. Michael Ramsey, Robert Riehn, Gautam V. Soni, Vincent Tabard-Cossa, Meni Wanunu, Matthew Wiggin, and Jeffery A. Schloss. The potential and challenges of nanopore sequencing. *Nat. Biotechnol.*, 26:1146–1153, 2008.

[6] Y. Tian, X. Hou, L.P. Wen, W. Guo, Y.L. Song, H.Z. Sun, Y.G. Wang, L. Jiang, and D.B. Zhu. A biomimetic zinc activated ion channel. *Chem. Comm.*, 46:1682–1682, 2010.

[7] Z.S. Siwy and S. Howorka. Engineered voltage-responsive nanopores. *Chem. Soc. Rev.*, 39:1115–1132, 2010.

[8] Jason K. Holt, Hyung Gyu Park, Yinmin Wang, Michael Stadermann, Alexander B. Artyukhin, Costas P. Grigoropoulos, Aleksandr Noy, and Olgica. Bakajin. Fast mass transport through sub-2-nanometer carbon nanotubes. *Science*, 312:1034–1037, 2006.

[9] Z. Siwy, E. Heins, C.C. Harrell, P. Kohli, and C.R Martin. Conical-nanotube ion-current rectifiers: the role of surface charge. *J. Am. Chem. Soc.*, 126:10850–10851, 2004.

[10] E.D. Steinle, D.T. Mitchell, M. Wirtz, S.B. Lee, and C.R Young, V.Y Martin. Ion channel mimetic micropore and nanotube membrane sensors. *Anal. Chem.*, 74:2416–2422, 2002.

[11] Aigars Piruska, Maojun Gong, Jonathan V. Sweedler, and Paul W. Bohn. Nanofluidics in chemical analysis. *Chem. Soc. Rev.*, 39:1060–1072, 2010.

[12] Stefan Howorka and Zuzanna. Siwy. Nanopore analytics: sensing of single molecules. *Chem. Soc. Rev.*, 38:2360–2384, 2009.

[13] Zhu Chen, Yingbing Jiang, Darren R. Dunphy, David P. Adams, Carter Hodges, Nanguo Liu, Nan Zhang, George Xomeritakis, Xiaozhong Jin, N. R. Aluru, Steven J. Gaik, Hugh W. Hillhouse, and C. Jeffrey. Brinker. Dna translocation through an array of kinked nanopores. *Nat. Mater.*, 9:667–675, 2010.

[14] Sang Bok Lee and Charles R. Martin. Electromodulated molecular transport in gold-nanotube membranes. *J. Am. Chem. Soc.*, 124:11850–11851, 2002.

[15] S. Prakash, J. Yeom, N. Jin, I. Adesida, and M. A Shannon. Characterization of ionic transport at the nanoscale. *Proc. Inst. Mech. Eng., Part N*, 220:45–52, 2007.

[16] Evin Gultepe, Dattatri Nagesha, Latika Menon, Ahmed Busnaina, and Srinivas. Sridhar. High-throughput assembly of nanoelements in nanoporous alumina templates. *Appl. Phys. Lett.*, 90:163119/1–163119/3, 2007.

[17] Z.X. Lu, A. Namboodiri, and M.M. Collinson. Self-supporting nanopore membranes with controlled pore size and shape. *ACS Nano*, 2:993–999, 2008.

[18] A. V. Raghunathan and N. R. Aluru. Self-consistent molecular dynamics formulation for electric-field-mediated electrolyte transport through nanochannels. *Phys. Rev. E: Stat., Nonlinear, Soft Matter Phys.*, 76:011202/1–011202/12, 2007.

[19] Paula J. Kemery, Jack K. Steehler, and Paul W. Bohn. Electric field mediated transport in nanometer diameter channels. *Langmuir*, 14:2884–2889, 1998.

[20] Matsuhiko Nishizawa, Vinod P. Menon, and Charles R. Martin. Metal nanotubule membranes with electrochemically switchable ion-transport selectivity. *Science*, 268:700–2, 1995.

[21] Meng-Yue Wu, Ralph M. M. Smeets, Mathijs Zandbergen, Ulrike Ziese, Diego Krapf, Philip E. Batson, Nynke H. Dekker, Cees Dekker, and Henny W. Zandbergen. Control of shape and material composition of solid-state nanopores. *Nano Lett.*, 9:479–484, 2009.

[22] A. J. Storm, J. H. Chen, X. S. Ling, H. W. Zandbergen, and C. Dekker. Fabrication of solid-state nanopores with single-nanometre precision. *Nat. Mater.*, 2:537–540, 2003.

[23] Daniel Fologea, James Uplinger, Brian Thomas, David S. McNabb, and Jiali. Li. Slowing dna translocation in a solid-state nanopore. *Nano Lett.*, 5:1734–1737, 2005.

[24] Rohit Karnik, Rong Fan, Min Yue, Deyu Li, Peidong Yang, and Arun. Majumdar. Electrostatic control of ions and molecules in nanofluidic transistors. *Nano Lett.*, 5:943–948, 2005.

[25] R.B. Schoch, J.Y. Han, and P. Renaud. Transport phenomena in nanofluidics. *Rev. Mod. Phys.*, 80:839–883, 2008.

[26] Derek Stein, Maarten Kruithof, and Cees. Dekker. Surface-charge-governed ion transport in nanofluidic channels. *Phys. Rev. Lett.*, 93:035901/1–035901/4, 2004.

[27] Allen J. Bard and Larry R. Faulkner. *Electrochemical Methods: Fundamentals and Applications.* John Wiley & Sons, 1980.

[28] Evgenij Barsoukov and Ross. MacDonald. *Impedance Spectroscopy: Theory, Experiment, and Applications, 2nd Edition.* Wiley-Interscience, 2005.

[29] J. Ross Macdonald. *Impedance spectroscopy: emphasizing solid materials and systems.* John Wiley and Sons, 1987.

[30] Eric Nathan Ervin, Henry S. White, Lane A. Baker, and Charles R. Martin. Alternating current impedance imaging of high-resistance membrane pores using a scanning electrochemical microscope. application of membrane electrical shunts to increase measurement sensitivity and image contrast. *Anal. Chem.*, 78:6535–6541, 2006.

[31] Eric Nathan Ervin, Henry S. White, and Lane A. Baker. Alternating current impedance imaging of membrane pores using scanning electrochemical microscopy. *Anal. Chem.*, 77:5564–5569, 2005.

[32] Digby D.. Macdonald. Reflections on the history of electrochemical impedance spectroscopy. *Electrochim. Acta*, 51:1376–1388, 2006.

[33] James Ross. Macdonald. Impedance spectroscopy: old problems and new developments. *Electrochim. Acta*, 35:1483–92, 1990.

[34] J. M. Kavanagh, S. Hussain, T. C. Chilcott, and H. G. L.. Coster. Fouling of reverse osmosis membranes using electrical impedance spectroscopy: Measurements and simulations. *Desalination*, 236:187–193, 2009.

[35] H.G.L. Coster and T.C Chilcott. *Surface chemistry and electrochemistry of membranes.* Marcel Dekker, Inc., 1999.

[36] H. G. L. Coster, K. J. Kim, K. Dahlan, J. R. Smith, and C. J. D. Fell. Characterization of ultrafiltration membranes by impedance spectroscopy. i. determination of the separate electrical parameters and porosity of the skin and sublayers. *J. Membr. Sci.*, 66:19–26, 1992.

[37] L. Gaedt, T. C. Chilcott, M. Chan, T. Nantawisarakul, A. G. Fane, and H. G. L..

Coster. Electrical impedance spectroscopy characterisation of conducting membranes ii. experimental. *J. Membr. Sci.*, 195:169–180, 2002.

[38] Ming-Chun Chien, Gou-Jen Wang, and Ming-Chang. Yu. Nanopore size estimation by electrochemical impedance spectroscopy analysis. *Jpn. J. Appl. Phys.*, 47:7459–7463, 2008.

[39] H. Kaiser, K. D. Beccu, and M. A.. Gutjahr. Abschtzung der porenstruktur porser elektroden aus impedanzmessungen. *Electrochim. Acta*, 21:539, 1976.

[40] Donald R.. Franceschetti. Small-signal a.c. response of supported thin-layer electrochemical cells. *J. Chem. Phys.*, 86:6495–501, 1987.

[41] Ming-Chun Chien, Gou-Jen Wang, and Win-Chun. Yu. Modeling ion diffusion current in nanochannel using infinitesimal distribution resistor-capacitor circuits. *Jpn. J. Appl. Phys., Part 1*, 46:7436–7440, 2007.

[42] N. Amani, M.R. Saberi, and J.K. Chamani. Investigation by fluorescence spectroscopy, resonance rayleigh scattering and zeta potential approaches of the separate and simultaneous binding effect of paclitaxel and estradiol with human serum albumin. *Protein Pept. Lett.*, 19:935–951, 2011.

[43] A. Doostmohammadi, A. Monshi, R. Salehi, M.H. Fathi, Z. Golniya, and A.U. Daniels. Bioactive glass nanoparticles with negative zeta potential. *Ceram. Int.*, 37:2311–2316, 2011.

[44] P. Leroy, C. Tournassat, and M. Bizi. Influence of surface conductivity on the apparent zeta potential of tio(2) nanoparticles. *J. Colloid Interface Sci.*, 356:442–453, 2011.

[45] Z. Omidvar, K. Parivar, H. Sanee, Z. Amiri-Tehranizadeh, A. Baratian, M.R. Saveri, A. Asoodeh, and J. Chamani. Investigations with spectroscopy, zeta potential and molecular modeling of the non-cooperative behaviour between cyclophosphamide hydrochloride and aspirin upon interaction with human serum albumin:

Binary and ternary systems from the view point of multi-drug therapy. *J. Biomol. Struct. Dyn.*, 29:181–206, 2011.

[46] J.R. Cogdell. *Foundations of Electric Circuits.* Prentice Hall, 1999.

[47] Michael J. Vitarelli, Shaurya Prakash, and David S. Talaga. Determining nanocapillary geometry from electrochemical impedance spectroscopy using a variable topology network circuit model. *Anal. Chem.*, 83:533–541, 2011.

[48] G. Gouy. Constitution of the electrical charge at the surface of an electroyte. *J. Phys. Theor. Appl.*, 9:457–468, 1910.

[49] D.A. Chapman. Contribution to the theory of electrocapillarity. *Philos. Mag., Ser. 6*, 25:475–481, 1913.

Chapter 2

Determining Nanocapillary Geometry From Electrochemical Impedance Spectroscopy Using the Variable Topology Finite Warburg Impedance Model

2.1 Introduction

In this chapter the Variable Topology finite Warburg Impedance Model (VTW), to determine the geometry and electrical double layer differential capacitance of a nanocapillary or nanopore is developed. The model is formulated by transforming an arraignment of resistors and capacitors into a differential equation. This model is similar to a transmission line[1, 2, 3] model but has the boundary condition such that if the nanocapillary has zero thickness the impedance is zero. The solutions for a constant and linearly varying nano-capillary radii are presented. Using the constant radii solution, the negative imaginary component of the impedance vs. frequency is shown. Plotting multiple signals as a function of the aspect ratio shows a shift in the peak frequency. Noting the location of the peak frequency, gives a measure of the total surface area, and thus total capacitance. Next, the EIS spectrum for multiple nanocapillaries is shown for linearly varying radii. It is shown that constrictions for the center radius, while fixing the DC limit will yield a depression in the EIS spectrum at the location of the peak frequency. The nanocapillary is not freely floating in space, but incased in a substrate. In this case the substrate is a polycarbonate tract-etched membrane. The impedance of which is added in parallel to the VTW model. Lastly the impedance of the electrical double-layer on the surface of the membrane is modeled as an $R \parallel C$ equivalent circuit element, and the background is also modeled as an $R \parallel C$ equivalent circuit element, both of which are added in series to the overall model, thus completing the model.

2.2 Theoretical Model

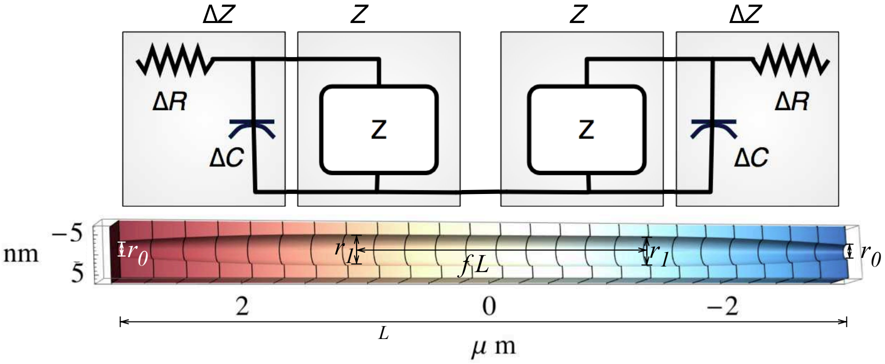

Figure 2.1: The above figure shows a schematic of the nanocapillary geometry with length L, center radius r_1 and opening radius, r_0. In addition to this there is a constant radii center section of length fL. The model is symmetrically presented, such that the variable radius and double-layer capacitance of the nanocapillary is accounted for by a differential equivalent circuit shown in the top panel. In the text a discussion of how the differential equation will be developed from the above figure, including discussion on boundary conditions and limits on the solution to the differential equation.

As illustrated in figure 2.1, a differential equivalent circuit model is developed to account for a variable nanocapillary radius and the double layer differential capacitance found within. The approach is similar to that used to construct mathematical models for transmission lines[1, 2, 3]. Essentially the model will be a combination of resistors and capacitors, which are then discretized and transformed into a differential equation whoes boundary conditions appropriate for the nanocapillary, that is the impedance of a nanocapillary which has zero length, has zero impedance.

The differential equation is developed by adding the total impedance Z to a infinitesimal amount ΔZ. This creates the left side of the equation. On the right side, the total impedance is again added to to an infinitesimal amount, however these are decomposed into resistive and capacitive elements. On the right side a differential element of the capillary resistance, $\Delta R(x)$, is added in series with a parallel circuit of a differential element of the nanocapillary double-layer capacitance, $\Delta C(x)$, and the overall impedance of the capillary, $Z(x)$:

$$Z(x)+\Delta Z(x) = R'(x)\Delta x+\frac{1}{\frac{1}{Z(x)}+i\omega C'(x)\Delta x} = R'(x)\Delta x+\frac{Z(x)}{i\omega Z(x)C'(x)\Delta x+1} \quad (2.1)$$

Here $i = \sqrt{-1}$, ω is the angular frequency of the AC signal, and x is the coordinate along the length of the nanocapillary. Next, expanding the right side of the differential equation into a Taylor series in Δx yields:

$$Z(x)+\Delta Z(x) = R'(x)\Delta x + Z(x) - i\omega Z^2(x)C'(x)\Delta x - \omega^2 Z^3(x)C'(x)^2\Delta x^2 + ... \quad (2.2)$$

Subtracting the total impedance from both sides yields:

$$\Delta Z(x) = R'(x)\Delta x - i\omega Z^2(x)C'(x)\Delta x - \omega^2 Z^3(x)C'(x)^2\Delta x^2 + ... \quad (2.3)$$

Finally, dividing by Δx, and evaluating the limit $\Delta x \to 0$ gives the differential equation,

$$Z'(x) + i\omega C'(x)Z^2(x) - R'(x) = 0, \quad (2.4)$$

where,

$$\frac{dR}{dx} = R'(x) = \frac{1}{\pi r^2(x)\kappa_{\mathrm{c}}}\ , \quad \text{and} \quad \frac{dC}{dx} = C'(x) = 2\pi r(x)\widetilde{C}_{\mathrm{c}}, \quad (2.5)$$

$\widetilde{C}_{\mathrm{c}}$ is the nanocapillary double-layer differential capacitance, and κ_{c} is the specific conductivity of the solution within the nanocapillary. Notice here the conductivity within the nanopore κ_{c} is mentioned here instead of simply saying solution conductivity. The conductivity within nanopore is found to be higher then that of the bulk[4, 5, 6, 7, 8]. In this formulation, a nanocapillary of length zero should have zero impedance and provides the boundary condition, $Z(0) = 0$. The symmetrized circuit element is obtained by solving the differential equation with $r(x)$ proceeding from $x = 0$ to $x = L/2$ and then replacing $r(x)$ by $r(L/2 - x)$ and proceeding again from $x = 0$ to $x = L/2$, to obtain the impedance for the total length, L, for the nanocapillary.

2.2.1 Solution for constant radius

For a constant radius, $r(x) = r_1$, the solution to equation 2.4 gives a solution, Z, as a function of x. Where again, x is the coordinate along the length of the nanocapillary. For a nanocapillary of length L, one would think to simply set x equal to L. However, this will produce an asymmetric solution. For the general case, to symmetrize this function one solves equation 2.4 with r(x) from 0 to L/2. Then add to this the mirror image of r(x), shifted back to the origin.This, however, is simple for a constant radius function. Since, the mirror of r1 shifted back to the origin, is a again, r1. For a constant radius function solve equation 2.4 with $r(x) = r_1$, then let x = L/2, half of the nanocapillary. Lastly, multiply the total impedance by 2, this is equivalent to solving the differential equation twice, with $r(x) = r_1$ and $r(x) = r_1$, then adding the solutions. The solution below is for a constant radius cylinder.

$$Z_{\text{cyl}}(\omega) = R_{\text{cyl}} \frac{\tanh\left(\sqrt{i\tau_{\text{cyl}}\omega/4}\right)}{\sqrt{i\tau_{\text{cyl}}\omega/4}}. \tag{2.6}$$

This solution, equation 2.6 has the same functional form, but different parameterization, as the finite Warburg impedance [9, 10, 11]. Equation 2.6 can be used to fit the geometry of a cylindrical nanocapillary, and has two free parameters for fitting: the DC resistance, R_{cyl}, and a time constant, τ_{cyl} given by:

$$R_{\text{cyl}} = \frac{L}{\pi r_1^2 \kappa_{\text{c}}}, \tag{2.7a}$$

$$\tau_{\text{cyl}} = R_{\text{cyl}}\, C_{\text{cyl}} = \frac{2L^2 \widetilde{C}_{\text{c}}}{r_1 \kappa_{\text{c}}}. \tag{2.7b}$$

Next, looking at limits of equation 2.6 one finds that in the DC limit, the limit in which the frequency approaches zero, the equation 2.6 acts as a pure electrolytic resistor. Furthermore, in the limit the electrical double layer differential capacitance approaches zero it also acts as a pure electrolytic resistor:

$$\lim_{\omega \to 0} Z_{\text{cyl}}(\omega) = \lim_{\widetilde{C} \to 0} Z_{\text{cyl}}(\omega) = \frac{L}{\pi r_1^2 \kappa_{\text{c}}} \tag{2.8}$$

While in the high frequency limit, the impedance of a capacitor approaches zero. Thus the current path will follow the least resistive path, that of the capacitor, yielding an overall zero impedance:

$$\lim_{\omega \to \infty} Z_{\text{cyl}}(\omega) = 0 \tag{2.9}$$

For a fixed DC limit, that is for fixed R_{cyl} changes in the double layer differential capacitance $\widetilde{C}$ only shift the spectrum along a parametric path. That is, it will only

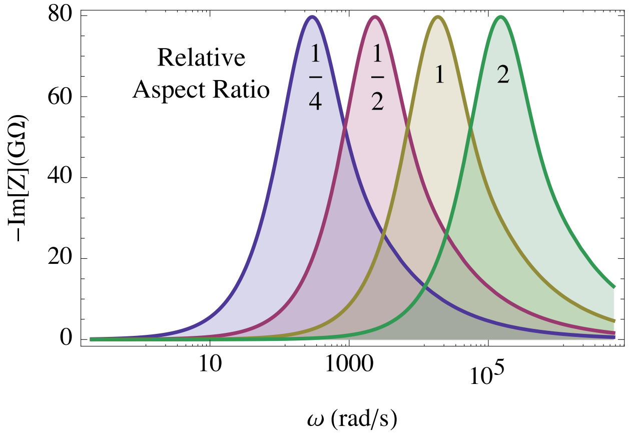

Figure 2.2: Above the negative imaginary component of the equation 2.6 for a fixed R_{cyl} is shown. This gives different peak frequencies depending on the nanocapillary cylindrical aspect ratio r/L. The aspect ratios labeled in the figure are relative to the reference geometry of L =6 μm , r =5 nm with $\kappa_{\text{c}} = 0.4$ S/m, $\widetilde{C}_{\text{c}} = 1.5$ mF/m^2. Plotting this as a standard Nyquist plot will only show a shift in the peak frequency, which is fairly difficult to distinguish from one plot to another.

shift the peak frequency. Similarly, changes in the aspect ratio of the nanocapillary for a constant R_{cyl} change the peak frequency in the Nyquist plot, which is obtained by maximizing $-\text{Im}[Z_{\text{cyl}}(\omega)]$ from equation 2.6 giving:

$$\omega_{peak} \approx 10.16/\tau_{\text{cyl}}. \tag{2.10}$$

By altering the aspect ratio, the capillary surface area is changed. As the surface area increases the overall capacitance of the capillary increases, which increases the time constant and consequently decreases the peak frequency, see equation 2.10. Again, this effect is best show by looking at the negative imaginary impedance, figure 2.2. Thus, EIS can distinguish the capillaries aspect ratio based on the peak frequency, assuming all the capillaries have the same differential capacitance.

2.2.2 Solution for linearly varying radius

Constriction at the center of the nanocapillary results in an hourglass shape, while constriction at the nanocapillary opening results in a lozenge shape. Both of theses cases can be treated with a linearly varying capillary radius:

$$r(x) = r_0 + 2x(r_1 - r_0)/L, \tag{2.11}$$

where, r_0 is the entrance radius, and r_1 is the center radius. Recalling that the model is symmetric both hourglass and lozenge shapes will yield identical impedance. Solving equation 2.4 using equation 2.11 gives a variation of the Warburg impedance, which the author named the variable topology finite Warburg impedance or $Z_{\mathrm{VTW}}(\omega)$. The linear case gives a closed form for lozenge shaped nanocapillaries.

$$\begin{aligned} Z_{\mathrm{loz}}(\omega) =& \frac{R_{\mathrm{loz}}(I_1(\xi_1)K_1(\xi_0) - I_1(\xi_0)K_1(\xi_1))}{\tau_1 - \tau_0} \times \\ & \left(\frac{\tau_1}{\xi_0(I_2(\xi_0)K_1(\xi_1) + I_1(\xi_1)K_2(\xi_0))} + \frac{\tau_0}{\xi_1(I_2(\xi_1)K_1(\xi_0) + I_1(\xi_0)K_2(\xi_1))} \right) \end{aligned} \tag{2.12}$$

where I_n is the modified Bessel function of the first kind of order n. And K_n is the modified Bessel function of the second kind of order n. Also with,

$$R_{\mathrm{loz}} = \frac{L}{\kappa_{\mathrm{c}} \pi r_1 r_0}, \tag{2.13}$$

and

$$\xi_0 = \sqrt{i4\tau_0\omega} \quad \text{and} \quad \xi_1 = \sqrt{i4\tau_1\omega} \tag{2.14}$$

where,

$$\tau_0 = \frac{L^2 \widetilde{C}_{\mathrm{c}} r_0}{2\kappa_{\mathrm{c}}(r_1 - r_0)^2} \quad \text{and} \quad \tau_1 = \frac{L^2 \widetilde{C}_{\mathrm{c}} r_1}{2\kappa_{\mathrm{c}}(r_1 - r_0)^2}. \tag{2.15}$$

The ratio of the time constants is equal to the ratio of the entrance radius and center radius.

$$\frac{\tau_1}{\tau_0} = \frac{r_1}{r_0} \tag{2.16}$$

Figure 2.3 shows the predicted effect of constricting the capillary opening on the EIS data. In each case the spectrum is normalized to fixing the DC limit. To have a fixed DC limit, with a fixed capillary length, and capillary conductivity, one needs the product $r_0 * r_1$ to be fixed in equation 2.13. This can be accomplished by setting $r_0 = r\alpha^{1/2}$ and $r_1 = r\alpha^{-1/2}$. Varying α in these cases keeps the DC limit fixed while changing the time constants. Thus, if one was performing only a DC measurement one would not

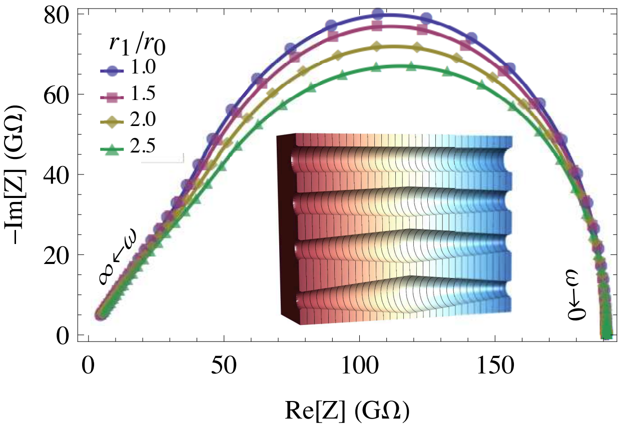

Figure 2.3: The effect of constriction of the openings of cylindrical nanocapillaries on the EIS spectrum is shown by plotting 2.12 for different ratios of the radii as shown in the figure legend. Each of the four nano-capillaries has the same DC resistance and would in principle give identical current-voltage curves in spite of having vastly different shapes. The EIS shows a clear change with nanocapillary geometry. The parameters used are L=6 μm, r_1=5 nm, κ_c=0.4 S/m, $\widetilde{C}_c$=1.5 mF/m^2. The inset shows renderings of the nanocapillary shapes corresponding to the radii ratios labeled in the figure.

---

measure any difference between the capillaries. However, the constriction reduces the magnitude of the imaginary component of the EIS data. This effect increases with the degree of constriction of the openings or the center.

2.2.3 Model Geometry extension

Nanopores and nanocapillaries may have many geometries[12], including quadraticly varying radii. In addition to this, the different $Z_{\rm VTW}$ circuit elements can be combined piecewise to account for different regions of variable nanocapillary radius. For example, the linear circuit element, $Z_{\rm loz}$, can be combined with cylindrical circuit element, $Z_{\rm cyl}$ to model a tapered nanocapillary that has a cylindrical center of fractional length f such as that illustrated in figure 2.1. The tapered capillary is modeled as the sum of two circuit elements:

$$Z_{\rm VTW} = Z_{\rm cyl} + Z_{\rm loz}, \tag{2.17}$$

the cylindrical center portion of length $f \cdot L$ in the center, 2.12, and two tapered regions of total length $(1-f)\cdot L$, as illustrated in figure 2.7. Thus in equation 2.6 L is replaced by $f \cdot L$, and in 2.13 and 4.4 L is replaced by $(1 - f) \cdot L$. Combining equation 2.12 and equation 2.6 requires the constraint that the cylindrical portion have the same radius as the end of the adjoining tapered region. The time constant for the cylindrical contribution is now determined by the other time constants:

$$\tau_{\mathrm{cyl}} = \frac{4R_{\mathrm{cyl}}^2 \tau_1 (\tau_0 - \tau_1)^2}{R_{\mathrm{loz}}^2 \tau_0^2}. \tag{2.18}$$

This eliminates τ_{cyl} as a fit variable.

Lastly, since the model, equation 2.12 is symmetric it can be extended to a conical model by simply doubling the length of the capillary and then dividing the overall impedance by 2.

2.3 Methods

2.3.1 Support Chamber

Two glass chambers sandwich two cylindrical pieces of polydimethylsiloxane (PDMS), with a NCAM (GE KN1CP02500) in between. The manufacturer specified that the NCAM has nanocapillary density of 6×10^8 capillaries/cm^2 ±15%, a thickness of 6 μm ±10%, prepared by track etching for a nominal pore radius of 5 nm +0% -20%. The glass chambers contain 5 ml of the test electrolyte solution in 18 MΩ Millipore water with a known concentration of electrolytes as discussed below. Ag/AgCl reference electrodes (MF-2052, Bioanalytical Systems, Inc.) and gold wire counter electrodes were used. The PDMS cylinders have a 0.60 cm diameter hole for an exposed NCAM surface area A_{mem} of 0.283 cm^2. The PDMS pieces are bonded following exposure to 30 W oxygen plasma[13, 14, 15]. The oxygen plasma attacks the surface of the PDMS, $CH_3[Si(CH_3)_2O]_nSi(CH_3)_3$, forming -$O_nSi(OH)_{4-n}$[13]. These then form covalent siloxane (Si-O-Si) bonds by a dehydration reaction with opposing surfaces.

All experiments were performed in a copper mesh Faraday cage to minimize electrical noise. The Au counter electrodes were RCA-1 cleaned before each experiment[16]. The RCA-1 cleaning procedure entails boiling the gold counter electrodes in a solution of 18 MΩ Millipore water, hydrogen peroxide, and ammonium hydroxide in a 10 to 1 to 0.1 ratio, at 100°C for 30 minutes. See Figure 2.4 for the experimental setup and Figure 2.5 for a picture of the device.

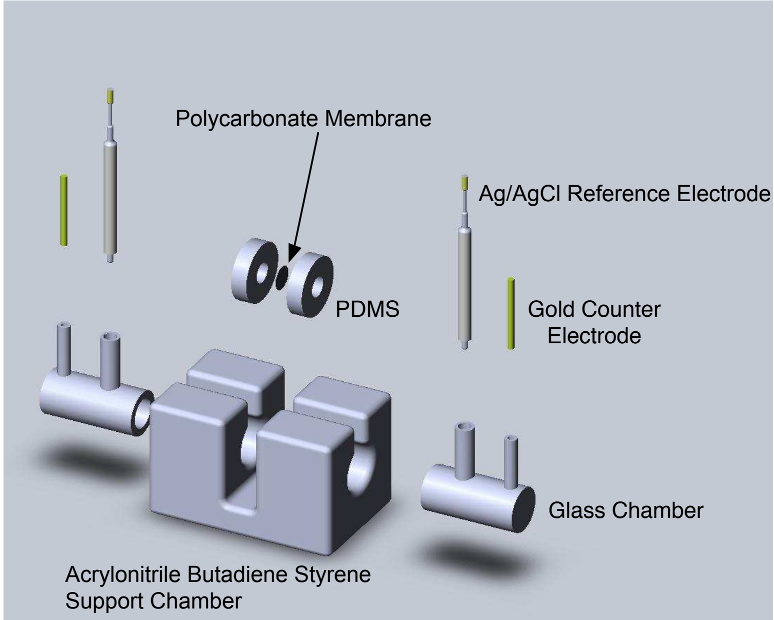
Polycarbonate Membrane
Ag/AgCl Reference Electrode
PDMS
Gold Counter Electrode
Glass Chamber
Acrylonitrile Butadiene Styrene Support Chamber

Figure 2.4: Here a figure of the experimental setup is presented, with gold counter electrodes, Ag/AgCl reference electrodes, the polycarbonate membrane, PDMS cylinders, and ABS support chamber clearly shown. Image created using Pro-E computer aided design software.

2.3.2 NCAM

NCAMs require equilibration prior to use[17]. Prior to use, the membranes were soaked in 18 MΩ Millipore water for 48 hours. Prior to each experiment, they were soaked at the experimental solution conditions for 4 hours. This is to ensure the the nanocapillaries within the membrane are not only hydrated, but have reached their equilibration. At equilibration they will have a slightly higher concentration of ions within themselves as compared to the bulk concentration. It is critical to maintain a constant pH so as to preserve the membrane surface charge density[18], which determines the double-layer capacitance[19]. A 10 mM sodium phosphate buffer was used to fix the pH at 7.0±0.1 at each of the five concentrations of NaCl: 100, 50, 20, 10, 0 mM. Bulk conductivities

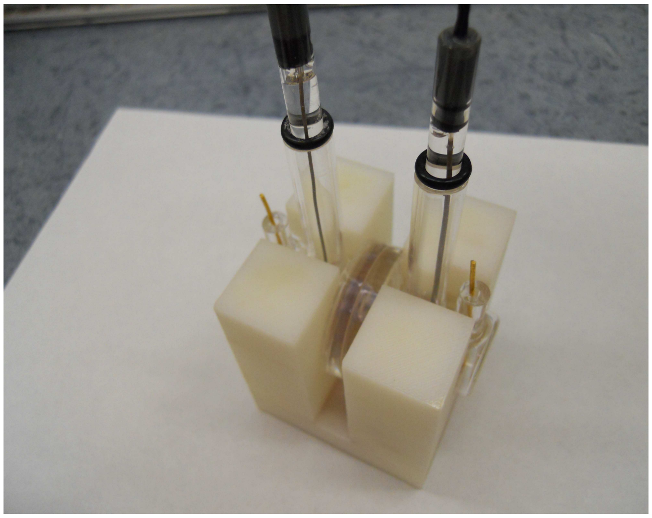

Figure 2.5: Here a figure of the device is presented. The gold counter electrodes and the Ag/AgCl reference electrodes are connected to a Gamry Instruments Reference 600 potentiostat. The purpose of the gold counter electrodes is to apply the field, while the reference electrodes measures the potential difference across the membrane.

---

of these solutions were interpolated from published values.[20] These values matched well with conductivity measurements made based on determining the cell constant and instrument without a membrane present but showed some deviations at high ionic strengths. (See supporting information.)

2.3.3 Potentiostat

A Gamry Instruments Reference 600 potentiostat was used to apply the potentials and measure the impedance in the system in a standard 4-electrode permeation cell mode. In this work, the applied potentials were kept low (10 mV AC amplitude and no DC bias) to minimize any Faradaic reactions. Furthermore, the reference electrodes are connected to a high impedance input and draw negligible current. 67 frequencies were measured ranging from 0.1 Hz to 1 MHz. Measurements were made for each solution condition with and without the membrane present to determine the cell constant and instrument response. Each experiment was repeated 4 times with a maximum variability of 0.8%, in the magnitude of impedance, and the data reported is the average of these measurements.

2.3.4 Fitting and Active Set

Each EIS measurement was subjected to Kramers-Kronig validation using a grid of 300 R||C functions with log-spaced time constants ranging from 9 ns to 400 s to fit using the active set approach.[21] Increasing the resolution and range of the grid did not improve the fits. The residuals were well behaved with magnitudes that matched the empirically observed run-to-run variability in the data. The equivalent circuit models were implemented in Mathematica 7.0.1 (Wolfram Research) and the data sets were fit using the built in `NonlinearModelFit` function. The variance of the residuals from the active set fit was used to estimate the per-point variance of the data sets and also used to determine a reduced chi-squared statistic, χ^2_{red}, to evaluate the quality of non-linear fits to the different equivalent circuit models:

$$\chi^2_{\mathrm{red}} = \frac{\nu_{\mathrm{as}}}{\nu_{\mathrm{m}}}\frac{\chi^2_{\mathrm{m}}}{\chi^2_{\mathrm{as}}} \tag{2.19}$$

Here, χ^2_{m} and χ^2_{as} are the summed squared residuals from the equivalent circuit model fit and the active set fit respectively. The corresponding degrees of freedom are ν_{m} and ν_{as}. Each of the 67 frequencies used produces an impedance with a real part and an imaginary part, thus n=134 measurements are made. For the active set fits, $\nu_{\mathrm{as}} = n - p$ where p is the number of active elements in the active set fit. For the nonlinear model fits, $\nu_{\mathrm{m}} = n - p$ where p is the number of free fit parameters in the model. Errors in nonlinear model fit parameters were taken from the estimates provided by the `NonlinearModelFit` function.

2.4 System modeling

The NCAM EIS data, shown in figure 2.9, is fit to various models of increasing complexity. Each model is identical except for the element representing the nanocapillary. In addition to the nanocapillary there is the cell and instrument response, the membrane surface effects, and the membrane itself. All of which add to the overall impedance of the system, and thus must be accounted for in the overall model. The cell and instrument response, the background, is modeled as a single R ∥ C circuit:

$$Z_{\text{bk}} = R_{\text{bk}} \parallel C_{\text{bk}}, \tag{2.20}$$

where, Z_{bk}, R_{bk}, and C_{bk}, are respectively the impedance, resistance, and capacitance of the electrochemical cell and instrument. The background can be seen in Panel B of figure 2.9. Next, a small feature accounting for less then 2% of the total impedance appears below 200 Hz. Membrane surfaces have been observed to give low-frequency dispersive responses in EIS[22]. This feature was not present in the background and thus must be attributed to the membrane. It it attributed to the double layer on the surface of the membrane and modeled as an R ∥ C circuit:

$$Z_{\text{ms}} = R_{\text{ms}} \parallel C_{\text{ms}}, \tag{2.21}$$

where, Z_{ms}, R_{ms}, and C_{ms}, are respectively the impedance, resistance, and capacitance of the electrical double layer on the surface of the membrane.

The NCAM is not composed on one single nanocapillary but N nanocapillaries, all in parallel. Adding in parallel to this the impedance due to the membrane, C_{mem} gives:

$$Z_{\text{sys}} = \frac{Z_{\text{VTW}}}{N} \parallel C_{\text{mem}}. \tag{2.22}$$

Finally, the overall equivalent circuit model, the sum of these elements, for the experiment becomes

$$Z_{\text{exp}} = Z_{\text{sys}} + Z_{\text{bk}} + Z_{\text{ms}} \tag{2.23}$$

or

$$Z_{\text{exp}} = \frac{Z_{\text{VTW}}}{N} \parallel C_{\text{mem}} + R_{\text{bk}} \parallel C_{\text{bk}} + R_{\text{ms}} \parallel C_{\text{ms}}. \tag{2.24}$$

Except for the element representing the nanocapillary, all elements will remain unchanged while altering the model in attempts to improve the fit.

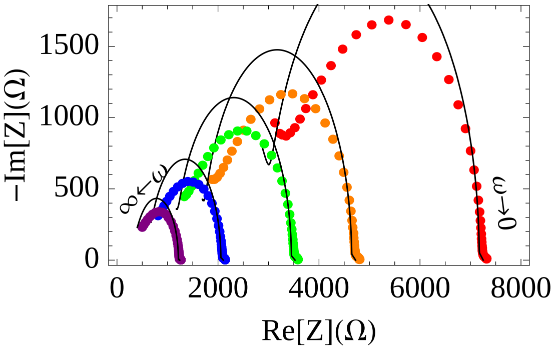

Figure 2.6: Notice this most basic model, using a single resistor to fit the nanocapillary equation 2.25 performs terribly, with a reduced chi squared of about 4500. The only feature the model can obtain is the DC limit. With bulk specific conductivities [S/m] of 1.093, 0.617, 0.342, 0.238, 0.136, purple, blue, green orange, red, respectively.

2.5 Nanocapillary Models

As mentioned, various models of increased complexity are fit to the EIS data where in each model all elements except that which represents the nanocapillary are unchanged. The first model is to use a single resistor R to fit the nanocapillary. Thus is in equation 2.24 Z_{VTW} is replaced with an R, while the impedance of the membrane surface, background, and membrane are fixed:

$$Z_{\text{exp}} = \frac{R}{N} \parallel C_{\text{mem}} + R_{\text{bk}} \parallel C_{\text{bk}} + R_{\text{ms}} \parallel C_{\text{ms}}. \tag{2.25}$$

The fit to this model is shown in figure 2.6. This model performs fairly poorly with a reduced chi squared of about 4500. The only feature this model is able to capture is the DC limit.

The next model is to consider modeling the nanocapillary with the constant radius model Z_{cyl} equation 2.6, while the overall model becomes:

$$Z_{\text{exp}} = \frac{Z_{\text{cyl}}}{N} \parallel C_{\text{mem}} + R_{\text{bk}} \parallel C_{\text{bk}} + R_{\text{ms}} \parallel C_{\text{ms}} \tag{2.26}$$

which is fit to the NCAM EIS data and shown in figure 2.7. This model requires and addition fit parameter, however substantially improves the fit with a reduced chi squared of 500. Unfortunately, this model still does not capture all of the depression

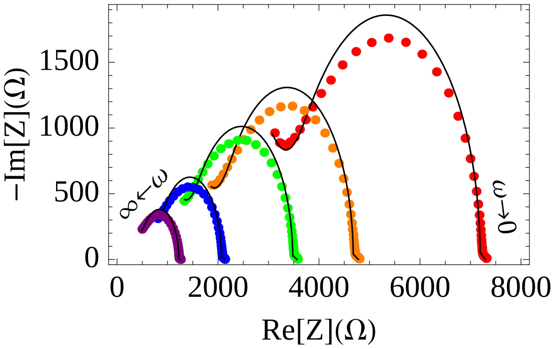

Figure 2.7: Modeling the nanocapillary with Z_{cyl}, equation 2.26 improves the fit with a reduced chi squared of 500 and is a 9 times improvement over equation 2.25. However, the model still does not capture the degree of suppression at the peak of the spectrum. With bulk specific conductivities [S/m] of 1.093, 0.617, 0.342, 0.238, 0.136, purple, blue, green orange, red, respectively.

in the EIS spectrum, indicated that the nanocapillary is not a cylinder but has a more lozenge type form.

Next the nanocapillary is modeled with Z_{loz}, equation 2.12 which gives not a constant radius, but a lozenge shape to the nanocapillaries. Replacing this with Z_{VTW} as our model for our nanocapillaries yields an overall model of

$$Z_{\text{exp}} = \frac{Z_{\text{loz}}}{N} \parallel C_{\text{mem}} + R_{\text{bk}} \parallel C_{\text{bk}} + R_{\text{ms}} \parallel C_{\text{ms}} \tag{2.27}$$

and is fit to the NCAM EIS data and shown in figure 2.8. This model requires and addition fit parameter over using equation 2.26, however dramatically improves the fit, capturing all the features of the data. Unfortunately, this model yields a reduces chi squared of 61, indicating that there is still room for improvement.

Nanowires grown in NCAMs have shown that NCAMs may be tapered only at the ends, but have a constant radii though out the center region of the nanocapillary.[23, 24, 25, 26, 27, 28] Using Z_{loz} implies that the taper is across the entire capillary rather than just at the ends. Thus, fitting with equation 2.24 implies the nanocapillary has a central cylindrical geometry with tapered ends, similar to a cigar. Panel A of figure 2.9 shows the EIS data fit to equation 2.24, while the background is fit to equation 2.20 as shown in Panel B, and the difference between them is shown in Panel C. The model

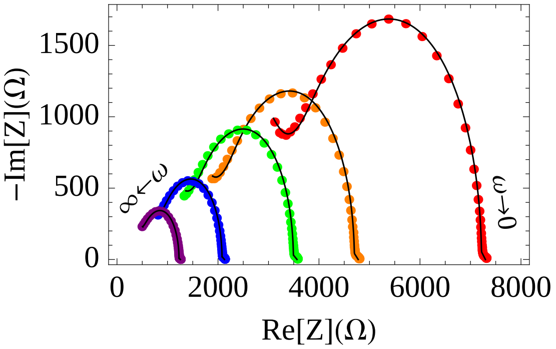

Figure 2.8: Modeling the nanocapillary with Z_{loz}, equation 2.27 improves the fit with a reduced chi squared of 61 and is a 9 times improvement over equation 2.26. The model accurately produces all the features of the data, however the still seemingly large reduced chi squared indicates that there is still improvements to the fit to be made. With bulk specific conductivities [S/m] of 1.093, 0.617, 0.342, 0.238, 0.136, purple, blue, green orange, red, respectively.

---

yields a reduced chi squared of 34, which is almost twice as low as the previous model, the lozenge model. This model is fit both locally, fitting the data sets individually, and globally, fitting all the data sets simultaneously. The advantage of fitting equation 2.24 globally is that one can directly fit to the desired parameters, while locally the fits yield time constants and resistances which must be again fit, vs. concentration to extract the desired properties. However, local fitting is required first to determine how certain parameters, the nanocapillary double layer differential capacitance, and the conductivity within the capillary depend on the bulk specific conductance.

Global fitting yields a reduces chi squared of 37, comparable to the local fitting. Table 2.5 summaries the quality of each model and the shows the number of parameters used in each fit. While table 2.5 shows the relevant fit parameters for equation 2.23 along with errors. The local fits reveal the time constants and resistance values for equation 2.23. Combinations of these parameters reveals their global dependance used in global fitting.

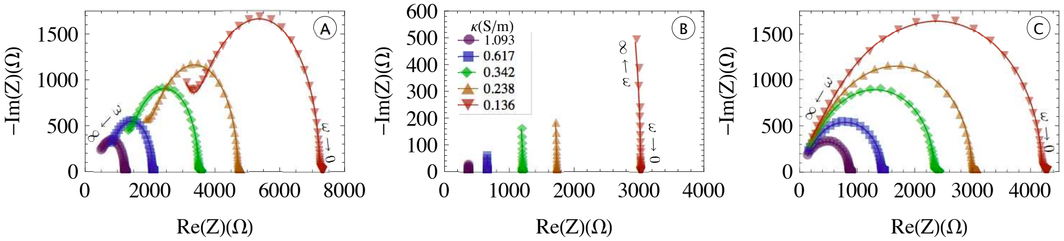

Figure 2.9: Panel A shows markers for experimental EIS data on a NCAM at 5 different concentrations of phosphate buffered NaCl that give conductivities as indicated in the figure ledgend. Panel B shows the response of the cell and instrument for the same solution conditions. Panel C shows the response of just the membrane obtained by the subtraction of the instrument response from the data. Local fits using 2.24, 2.20 and their difference are shown as solid lines in panels A, B, and C, respectively.

Table 2.1: Quality of Model Fits

Model	$\chi^2_{\mathrm{m}} \cdot 10^3$	p	ν	χ^2_{red}
$R \parallel C_{\mathrm{mem}}$	7700	30	640	4500
$Z_{\mathrm{cyl}} \parallel C_{\mathrm{mem}}$	860	35	635	500
$Z_{\mathrm{loz}} \parallel C_{\mathrm{mem}}$	100	40	630	61
local $(Z_{\mathrm{loz}} + Z_{\mathrm{cyl}}) \parallel C_{\mathrm{mem}}$	57	45	625	34
global $(Z_{\mathrm{loz}} + Z_{\mathrm{cyl}}) \parallel C_{\mathrm{mem}}$	64	22	658	37
Active Set	1.5	100	570	1.0

2.6 Local fits reveal global NCAM EIS model

There are two types of parameters in the Z_{VTW} impedance element. Geometric parameters such as r_0, r_1, N, and L which should be independent of the electrolyte concentration. The capacitance of the double layer should depend on the electrolyte concentration. The changes in EIS with electrolyte concentration allows separation of these effects through a global analysis. Figure 2.6 shows plots of combinations of the local parameters that allow extraction of the global dependence of the geometric and capacitive properties of the nanocapillaries.

Figure 2.6A shows a plot of the combination of parameters that isolates the effective

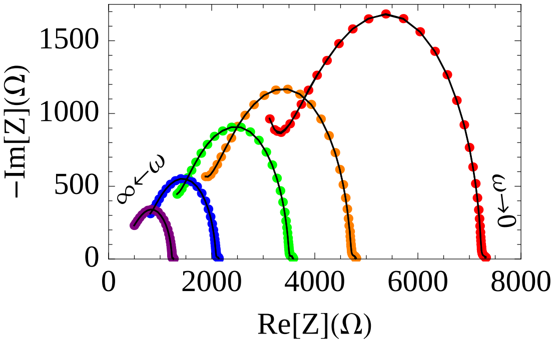

Figure 2.10: Fits using active set are shown above. With bulk specific conductivities [S/m] of 1.093, 0.617, 0.342, 0.238, 0.136, purple, blue, green orange, red, respectively.

Table 2.2: Parameters for local fits to $Z_{\mathrm{VTW}} = Z_{\mathrm{cyl}} + Z_{\mathrm{loz}}$

NaCl mM	Buffer mM	κ_{b} S/m	τ_0 μs	τ_1 μs	R_{cyl}/N Ω	R_{loz}/N Ω
100	10	1.093±0.004	1.6±0.8	4.0±1.3	226±4	644±11
50	10	0.617±0.002	3.9±1.0	8.8±1.6	360±6	1070±14
20	10	0.342±0.001	8.2±1.9	17±3	598±9	1740±20
10	10	0.238±0.001	14±3.5	27±5	788±13	2198±24
0	10	0.136±0.001	31±7.6	52±10	1180±20	3024±30

capillary conductivity,

$$\kappa_{\mathrm{c}} = \frac{(\tau_0+\tau_1)^2}{\tau_1(R_{\mathrm{loz}}\tau_0 + R_{\mathrm{cyl}}\tau_1)}\frac{L}{\pi(r_0+r_1)^2N}, \tag{2.28}$$

versus the bulk solution conductivity. The conductivity in the capillary is observed to be linearly related to the bulk conductivity ($\kappa_{\mathrm{c}} = \kappa_{\mathrm{b}} + \kappa_0$) with ($\kappa_0$ =0.105±0.003 S/m). The slightly higher conductivity inside the nanocapillary is consistent with the requirement of additional charge to neutralize capillary surface charge.[29] This effect is most noticeable for capillaries with diameters comparable to the Debye length at a given electrolyte concentration.[4, 5, 6, 7, 8]

Figure 2.6B shows a plot of the ratio of time constants which is related to the ratio of the entrance and center radii through equation 2.16. The plot shows that the ratio of radii parameter has an average value of 2.0±0.1. Figure 2.6C shows a plot of the combination of local fit parameters that give the fraction of the nanocapillary length that is cylindrical:

$$f = \frac{\tau_1 R_{\mathrm{cyl}}}{\tau_1 R_{\mathrm{cyl}} + \tau_0 R_{\mathrm{loz}}} \tag{2.29}$$

Figure 2.6C shows that the cylindrical fraction parameter has an average value of 0.416±0.009. Both of the geometric nanocapillary parameters show a modest dependence of their values on the conductivity. In both cases the conductivity dependence is smaller than the error in the parameters as propagated from the fit parameters. This small effect is likely due to the covariance of fit parameters in the local nonlinear fitting function.

Figure 2.6D shows a plot of the combination of parameters that isolates the differential capacitance of the nanocapillary interior:

$$\widetilde{C}_{\mathrm{c}} = \frac{2\left(\tau_0 - \tau_1\right)^2 \left(\tau_1 R_{\mathrm{cyl}} + \tau_0 R_{\mathrm{loz}}\right)}{\pi r_1 \tau_0^2 R_{\mathrm{loz}}^2 L\, N}, \tag{2.30}$$

The differential capacitance showed a square root dependence on solution conductivity ($\widetilde{C}_{\mathrm{c}} = \widetilde{C}_0 + \widetilde{C}_1\sqrt{\kappa_{\mathrm{b}}}$) with $\widetilde{C}_0$=1.12±0.03 mF/m^2 and $\widetilde{C}_1$=0.53±0.04 mF/m$^2\sqrt{\mathrm{m/S}}$. The square root power law is consistent with a simple Gouy-Chapman interpretation of the double layer capacitance.[30, 31, 32] Appendix A is dedicated to a discussion on the Gouy-Chapman model.

2.7 EIS global fitting gives NCAM geometry

To obtain final nanocapillary geometric properties, the data was subjected to a global fit to equation 2.17. The dependencies of the local fit parameters on the nanocapillary properties are defined by equations 4.4, 2.12, 3.4a, and 3.4b with the total length parameter replaced by the appropriate fractional length as discussed for equation 2.17. The global analysis directly fit the nanocapillary geometric properties r_0,r_1,f as independent of bulk conductivity. The parameters that control the bulk conductivity dependence of differential capacitance and the capillary conductivity ($\widetilde{C}_0$, $\widetilde{C}_1$ and κ_0) are also re-optimized by the global fit. The background circuit element was globally modeled as a simple electrolyte solution resistor ($R_{\mathrm{bk}} = R_{\mathrm{cell}}/\kappa_{\mathrm{b}}$) with a power-law conductivity-dependent capacitance constant ($C_{\mathrm{bk}} = C_{1\mathrm{bk}}\kappa_{\mathrm{b}}^{3/2} + C_{0\mathrm{bk}}$). The same power

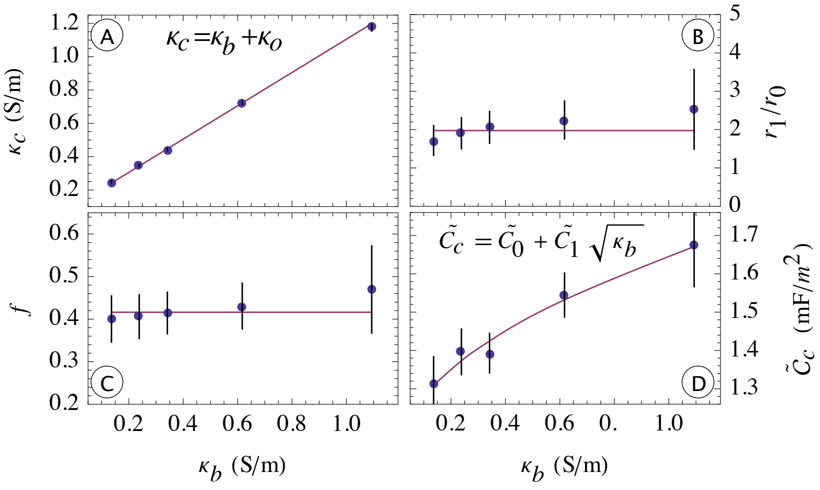

Figure 2.11: Local fit parameters were plotted in combination (points) to obtain the global dependence (fit lines) of nanocapillary parameters as discussed in the text. Error bars were propagated from the standard errors from the fit parameters. Panel A shows the capillary conductivity vs. the bulk conductivity. A linear dependence is found with a constant offset to account for surface charge counter ions in the nanocapillary. Panel B shows the ratio of the radii, r_1/r_0. Panel C shows the fraction, f, of the length, L, of the capillary that is cylindrical. Panel D shows the capillary double-layer differential capacitance and a fit to a square root power law.

---

law functions were observed to fit the instrument response of both the background measurement and the NCAM measurement. The cell constant, R_{cell} was the also the same within experimental uncertainty. The low frequency circuit element (10 parameters) was not re-optimized from the local values that appear in the supporting information. The parameters L, N, and C_{mem} were allowed to float after initial convergence.

Table 2.7 shows the 12 global fit parameters. The uncertainties in table 2.7 were estimated based on the diagonal elements of the covariance matrix of the χ^2 surface for the global fit. For many of the parameters these estimates appear to be unrealistically small if interpreted as uncertainties in the determination of the parameter. Use of the covariance matrix to determine parameter uncertainties is based on the assumption that all variance is due to random errors. The magnitude of the active set fit residuals was consistent with random noise in the measurement. The squared residuals for both the local and global fits are a factor of ~35 larger than those of the active set implying that

Table 2.3: NCAM EIS global fit parameters

r_0	2.19	±	0.01	nm
r_1	4.05	±	0.01	nm
f	0.408	±	0.007	
κ_0	0.109	±	0.001	S/m
$\widetilde{C}_0$	1.21	±	0.05	$\mathrm{mF/m^2}$
$\widetilde{C}_1$	0.36	±	0.09	$\mathrm{mF/m^2}\sqrt{\mathrm{m/S}}$
R_{cell}	410	±	2	$\mathrm{m^{-1}}$
$C_{0\mathrm{bk}}$	7.8	±	1.8	pF
$C_{1\mathrm{bk}}$	58	±	26	$\mathrm{pF(m/S)^{3/2}}$
N	1.70	±	$0.01{\cdot}10^8$	
L	6.00	±	0.03	μm
C_{mem}	139	±	17	pF

there is some aspect of the NCAM response not being accounted for in the model *vida infra*. In this case the uncertainties in the parameters as determined from the diagonal covariance matrix elements must be interpreted as measures of how well the parameter is defined by the fitting procedure.

2.8 Possible model limitations

The equivalent circuit model fits the data well and is able to produce a quantitative estimate of the nanocapillary geometry. However, the fit residuals result in a value of χ^2_{red} that suggest that the model is still incomplete. There are several aspects of the equivalent circuit model where improvement in the physical description of the model could lead to a better fit to the data. Since any of the improvements could be invoked, none should be without specific evidence. In each case there is no evidence compelling the increase in complexity. Therefore inclusion of these phenomena is beyond the scope of the present work.

Though the Z_{VTW} approach can accommodate a distribution of nanocapillary radii and/or shape, the current model does not include any contribution from nanocapillary geometric heterogeneity; it assumes all nanocapillaries have the same geometry. Adding a distribution of geometries would increase the dispersion of the time scales in the main EIS feature and would lead to an improvement in the fit. However, ion-track etched nanocapillaries are reported to be largely homogenous in geometry.[23, 25, 27]. Attributing the dispersion of the nanocapilllary contribution to the EIS signal would imply a distribution of capillary cylindrical radii covering a range of ∼2.5 times the average radius. This is in significant excess of the specified and observed distribution of ion-track etched nanocapillaries.

The range of time constants present in the component attributed to the membrane could include contributions outside of the low-frequency region that the equivalent circuit model currently treats. The phenomenological treatment of these low-frequency contributions is descriptive and invokes serial $R \parallel C$ circuits. To resolve any possible overlap between these dispersive membrane contributions to the EIS and the nanocapillary response would require a better phenomenological description than serial $R \parallel C$ circuits. Until such treatments are available this sort of ambiguity is likely to persist.

The geometry used to solve Z_{VTW} and treat the nanocapillaries may be too simplistic to represent the real nanocapillaries. The present model exhibiting tapered ends with an approximately cylindrical center is most complicated overall geometry that has been confirmed to be present in NCAMs.[23, 24, 25, 26, 27, 28] Independent characterization of any variability of the nanocapillary radius is needed to provide justification for additional geometric complexity.

The surface of the polycarbonate membrane is coated with polyvinylpyrrolidone. This detail is not distinguished in the model. Given the thinness of the PVP passivation layer, it is unlikely that it would contribute significantly to the impedance of the circuit.

The double-layer differential capacitance is treated as a simple differential capacitor element.[19] The actual response of the double layer is likely more complicated. It has been proposed to use multiple $R \parallel C$ components in order to separate the electrical double layer into the more diffuse Gouy-Chapman layer and inner, more compact Stern layer.[33] Substitution of a more complicated model for the differential capacitor element would increase the dispersion of Z_{VTW} and possibly improve the fit. However, as with the other examples of added model complexity, there is no independent evidence to prefer this approach to improving the fit over the others already discussed.

2.9 Comparison of fit parameters and manufacturer's specifications

The fit parameters suggest that the openings to the nanocapillaries are constricted by a factor of 1.85 from their centers. Several imaging studies have shown that the nanocapillaries are wider the middle as compared to the entrance and exit.[23, 28, 27, 25, 26, 24] The middle region of nanocapillaries can be wider than the entrance and exit by almost 3 times in some cases.[23].

The fit parameters indicate a nanocapillary entrance (and exit) radius of 2.19 ± 0.01 nm and a center radius of 4.05 ± 0.01 nm. The manufacturer reports the nominal radius to be 5 nm, with a tolerance between 0 and -20% (or 4.5 ± 0.5 nm) a membrane thickness of 6 μm with a tolerance of ± 10%; and a capillary density of 6×10^8 capillaries/cm^2 with a tolerance of ± 15%. Therefore, the fit parameter for the center radius is at the low end of the manufacturer's specifications. The uncertainty in the membrane thickness and nanocapillary number density together could change the estimated opening and center radii to be 2.49 nm and 4.61 nm, respectively. Several additional phenomena could account for a systematic underestimation of the nanocapillary radii.

The mobility of ions in the electrical double layer is expected to be reduced compared to those in the bulk. Such effects of electroviscosity[34, 35] are not explicitly incorporated into the model. It is possible that such an effect would increase the impedance of the nanocapillary. The net effect in fitting the present model would be to underestimate the nanocapillary radii to compensate for the added impedance. An improvement to the present model might, therefore, be to add a differential resistive element in series with the double layer differential capacitive element. The low frequency component that was attributed to the membrane surface was modeled as a single $R \parallel C$ circuit. The active set fits indicated that this component was very dispersive in nature requiring 6 $R \parallel C$ components covering at least 4 decades in decay time. It is possible that the membrane surface response also included impedance in the same spectral region as the nanocapillaries. In this case the additional impedance would manifest as a smaller nanocapillary radius in the fitting.

Both the membrane thickness and capillary number density are coupled in the fitting to the capillary geometry. If the thickness of the membrane during the experiment is larger than that specified or if the number density of the nanocapillaries is lower than that specified, then the nanocapillaries radius will be underestimated. Changing membrane thickness will also influence the membrane capacitance. However, for changes in C_{mem} consistent with the variability of the membrane thickness, essentially no changes were observed for the geometric parameters.

2.10 Conclusion

An analytical modeling approach for extracting nanocapillary geometry and double layer differential capacitance from EIS data has been presented and validated experimentally through measurement on a commercial NCAM. By exploiting the differences between the nanoscale and the bulk response to changes in electrolyte concentration, the model provides a quantitative estimate for the nanocapillary geometry. The methodology presented in this work is expected to be of interest to the larger community of nanopore and nanocapillary investigators due to the non-invasive nature of the technique.

Table 2.4: NCAM Nomenclature List

name	definition	SI unit
Z	impedance	$[\Omega]$
R	resistance	$[\Omega]$
R'	dR/dx	$[\Omega/\mathrm{m}]$
C'	dC/dx	[F/m]
ω	angular frequency	[rad/s]
i	$\sqrt{-1}$	[]
r	radius	[m]
$\widetilde{C}_{\mathrm{c}}$	capillary double-layer differential capacitance	$[\mathrm{F/m^2}]$
κ_{c}	capillary conductivity	[S/m]
κ_{b}	bulk conductivity	[S/m]
L	capillary length	[m]
Z_{cyl}	cylindrical impedance model	$[\Omega]$
Z_{loz}	lozenge impedance model	$[\Omega]$
Z_{VTW}	variable topology finite Warburg impedance	$[\Omega]$
R_{cyl}	resistance of a cylinder	$[\Omega]$
R_{loz}	resistance of a lozenge	$[\Omega]$
r_0	entrance (and exit) radius	[m]
r_1	center radius	[m]
f	fraction cylindrical length of nanocapillary	[]
τ_{cyl}	time constant for constant radius capillary	[s]
τ_0	time constant for r_0 in Z_{loz}	[s]
τ_1	time constant for r_1 in Z_{loz}	[s]
C_{mem}	membrane capacitance	[F]
N	number of capillaries	[]
A_{mem}	membrane area	$[\mathrm{m^2}]$
R_{ms}	resistance of external membrane surface	$[\Omega]$
C_{ms}	capacitance of external membrane surface	[F]
R_{bk}	cell and instrument resistance	$[\Omega]$
R_{cell}	cell constant	$[\mathrm{m^{-1}}]$
C_{bk}	cell and instrument capacitance	[F]
$C_{0\mathrm{bk}}$	constant coefficient in C_{bk} fit	[F]
$C_{1\mathrm{bk}}$	$\kappa^{3/2}$ coefficient in C_{bk} fit	$[\mathrm{F\ (m/S)^{3/2}}]$
Z_{bk}	cell and instrument impedance	$[\Omega]$
Z_{exp}	experiment impedance	$[\Omega]$
Z_{sys}	system impedance	$[\Omega]$
κ_0	increased capillary conductivity offset	[S/m]
$\widetilde{C}_0$	constant coefficient in $\widetilde{C}_{\mathrm{c}}$ fit	$[\mathrm{F/m^2}]$
$\widetilde{C}_1$	square root coefficient in $\widetilde{C}_{\mathrm{c}}$ fit	$[\mathrm{F/m^2}\sqrt{\mathrm{m/S}}]$
ν	degrees of freedom	[]
p	number of fit parameters	[]
χ^2_{m}	chi squared model	$[\Omega^2]$
χ^2_{as}	chi squared active set	$[\Omega^2]$
χ^2_{red}	reduced chi squared	[]

Bibliography

[1] H. Kaiser, K. D. Beccu, and M. A.. Gutjahr. Abschtzung der porenstruktur porser elektroden aus impedanzmessungen. *Electrochim. Acta*, 21:539, 1976.

[2] Donald R.. Franceschetti. Small-signal a.c. response of supported thin-layer electrochemical cells. *J. Chem. Phys.*, 86:6495–501, 1987.

[3] Ming-Chun Chien, Gou-Jen Wang, and Win-Chun. Yu. Modeling ion diffusion current in nanochannel using infinitesimal distribution resistor-capacitor circuits. *Jpn. J. Appl. Phys., Part 1*, 46:7436–7440, 2007.

[4] Caroline Desgranges and Jerome. Delhommelle. Molecular simulation of transport in nanopores: Application of the transient-time correlation function formalism. *Phys. Rev. E: Stat., Nonlinear, Soft Matter Phys.*, 77:027701/1–027701/4, 2008.

[5] Rohit Karnik, Rong Fan, Min Yue, Deyu Li, Peidong Yang, and Arun. Majumdar. Electrostatic control of ions and molecules in nanofluidic transistors. *Nano Lett.*, 5:943–948, 2005.

[6] Reto B. Schoch, Harald van Lintel, and Philippe. Renaud. Effect of the surface charge on ion transport through nanoslits. *Phys. Fluids*, 17:100604/1–100604/5, 2005.

[7] Derek Stein, Maarten Kruithof, and Cees. Dekker. Surface-charge-governed ion transport in nanofluidic channels. *Phys. Rev. Lett.*, 93:035901/1–035901/4, 2004.

[8] Yuk Wai Tang, Istvan Szalai, and Kwong-Yu. Chan. Diffusivity and conductivity of a primitive model electrolyte in a nanopore. *Mol. Phys.*, 99:309–314, 2001.

[9] E. Warburg. Ueber das verhalten songenannter unpolarisirbarer elektroden gegen wechselstrom. *Ann. Physik.*, 67:493–499, 1899.

[10] J. Ross. Macdonald. Simplified impedance/frequency-response results for intrinsically conducting solids and liquids. *J. Chem. Phys.*, 61:3977–96, 1974.

[11] Donald R. Franceschetti, J. Ross Macdonald, and Richard P. Buck. Interpretation of finite-length-warburg-type impedances in supported and unsupported electrochemical cells with kinetically reversible electrodes. *J. Electrochem. Soc.*, 138:1368–71, 1991.

[12] Shaurya Prakash, Aigars Piruska, Enid N. Gatimu, Paul W. Bohn, Jonathan V. Sweedler, and Mark A. Shannon. Nanofluidics: systems and applications. *IEEE Sens. J.*, 8:441–450, 2008.

[13] David C. Duffy, J. Cooper McDonald, Olivier J. A. Schueller, and George M. Whitesides. Rapid prototyping of microfluidic systems in poly(dimethylsiloxane). *Anal. Chem.*, 70:4974–4984, 1998.

[14] J. Cooper McDonald and George M. Whitesides. Poly(dimethylsiloxane) as a material for fabricating microfluidic devices. *Acc. Chem. Res.*, 35:491–499, 2002.

[15] H. Hillborg, J. F. Ankner, U. W. Gedde, G. D. Smith, H. K. Yasuda, and K. Wikstrom. Crosslinked polydimethylsiloxane exposed to oxygen plasma studied by neutron reflectometry and other surface specific techniques. *Polymer*, 41:6851–6863, 2000.

[16] Werner Kern and David A.. Puotinen. Cleaning solution based on hydrogen peroxide for use in silicon semiconductor technology. *RCA Rev.*, 31:187–206, 1970.

[17] E.D. Steinle, D.T. Mitchell, M. Wirtz, S.B. Lee, and C.R Young, V.Y Martin. Ion channel mimetic micropore and nanotube membrane sensors. *Anal. Chem.*, 74:2416–2422, 2002.

[18] Shaurya Prakash, M. B. Karacor, and S. Banerjee. Surface modification in microsystems and nanosystems. *Surf. Sci. Rep.*, 64:233–254, 2009.

[19] Allen J. Bard and Larry R. Faulkner. *Electrochemical Methods: Fundamentals and Applications*. John Wiley & Sons, 1980.

[20] C. Robert Weast, editor. *CRC Handbook of Chemistry and Physics.* CRC Press, Inc., 1989-1990.

[21] Jason T. Giurleo and David S.. Talaga. Global fitting without a global model: Regularization based on the continuity of the evolution of parameter distributions. *J. Chem. Phys.*, 128:114114/1–114114/18, 2008.

[22] Hans G. L. Coster. The double fixed charge membrane. low frequency dielectric dispersion. *Biophys. J.*, 13:118–32., 1973.

[23] C. Schonenberger, B. M. I. Van Der Zande, and L. G. J.. Fokkink. Nanowires grown electrochemically in porous templates. *Mater. Res. Soc. Symp. Proc.*, 451:359–365, 1997.

[24] Gonzalo Riveros, Humberto Gomez, Ricardo Schrebler, Ricardo E. Marotti, and Enrique A. Dalchiele. An in situ eis study during the electrochemical growth of copper nanowires into porous polycarbonate membranes. *Electrochem. Solid-State Lett.*, 11:K19–K23, 2008.

[25] Munekazu Motoyama, Yasuhiro Fukunaka, Tetsuo Sakka, Yukio H. Ogata, and Shiomi. Kikuchi. Electrochemical processing of cu and ni nanowire arrays. *Proc. - Electrochem. Soc.*, 2004-19:99–108, 2006.

[26] M. De Leo, F. C. Pereira, L. M. Moretto, P. Scopece, S. Polizzi, and P. Ugo. Towards a better understanding of gold electroless deposition in track-etched templates. *Chem. Mater.*, 19:5955–5964, 2007.

[27] S. Leopold, I. U. Schuchert, J. Lu, M. E. Toimil Molares, M. Herranen, and J.-O. Carlsson. Electrochemical deposition of cylindrical cu/cu2o microstructures. *Electrochim. Acta*, 47:4393–4397, 2002.

[28] E. Ferain and R. Legras. Pore shape control in nanoporous particle track etched membrane. *Nucl. Instrum. Methods Phys. Res., Sect. B*, 174:116–122, 2001.

[29] J. J. Tulock, M. A. Shannon, P. W. Bohn, and J. V. Sweedler. Microfluidic separation and gateable fraction collection for mass-limited samples. *Anal. Chem.*, 76:6419–6425, 2004.

[30] Alexei A.. Kornyshev. Double-layer in ionic liquids: Paradigm change? *J. Phys. Chem. B*, 111:5545–5557, 2007.

[31] John O'M. Bockris, Amulya K.N. Reddy, and Maria Evgenij Gamboa-Aldeco. *Modern Electrochemistry 2A, Second Edition: Fundamentals of Electrodics.* Plenum Pub Corp, 2001.

[32] Jan C. T. Eijkel and Albert. van den Berg. Nanofluidics and the chemical potential applied to solvent and solute transport. *Chem. Soc. Rev.*, 39:957–973, 2010.

[33] L. Gaedt, T. C. Chilcott, M. Chan, T. Nantawisarakul, A. G. Fane, and H. G. L.. Coster. Electrical impedance spectroscopy characterisation of conducting membranes ii. experimental. *J. Membr. Sci.*, 195:169–180, 2002.

[34] N. R. Tas, J. Haneveld, H. V. Jansen, M. Elwenspoek, and A. van den Berg. Capillary filling speed of water in nanochannels. *Appl. Phys. Lett.*, 85:3274–3276, 2004.

[35] R.B. Schoch, J.Y. Han, and P. Renaud. Transport phenomena in nanofluidics. *Rev. Mod. Phys.*, 80:839–883, 2008.

Chapter 3

Theoretical Models for Electrochemical Impedance Spectroscopy of Unfolded Proteins Though Nanopores and Relation to Zeta Potential

3.1 Introduction

Individual solid-state nanopores have been fabricated[1, 2] and have been used to develop synthetic systems for ion-channel studies[3, 4, 5, 6, 7], single molecule sensing[8, 9, 10], DNA resistive pulse measurements[1, 10], and DNA sequencing.[11] Recently, electrochemical impedance spectroscopy or EIS[12, 13, 14], which measures the impedance as a function of frequency of applied AC potential, has been used to analyze these nanopores[15]. Since the EIS signal is a measure of the electrokinetic transport of solutions though nanopores, it is sensitive to the surface properties and geometries of these nanopores.[16, 17, 15] Vitarelli, et.al.[15] has shown that by measuring the impedance of nanopores in a conducting solution it is possible to obtain their geometry and the double layer differential capacitance at the walls of the nanopores. Now that an accurate model exists to predict the nanopore geometry dependance of EIS spectrum in a conducting solution, it is possible to extend this model to include the influence of large molecular species, such as proteins, within the nanopore.

This chapter extends the Variable Topology Finite Warburg (VTW) impedance model[15] to include the effect of an unfolded protein within the nanopore, see 3.1. The protein was modeled as a cylinder with a surface charge density that, when in a conducting solution, produces an electrical double layer (EDL) differential capacitance along its surface. Resistive pulse measurements[1, 10] use only the DC potential to measure the current vs. time and typically bin the average current drop and event duration via histograms. This capacitance due to the EDL allows for the measurement

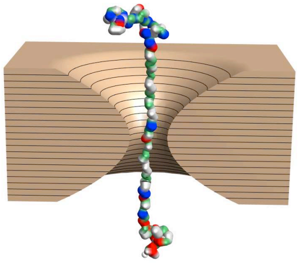

Figure 3.1: Figure above shows an unfolded and elongated protein traversing the nanopore. Each colored sphere on the protein is an amino acid. As the protein passes though the nanopore the groupings of amino acids will be sampled. The amount of excluded volume and surface charge density within each grouping will effect the overall impedance. The goal of this study is to determine the impedance of a protein within a nanopore and propose a method to rapidly sequence a protein.

of the complex resistance under the application of an AC potential. In the natural state a protein is globular however is shown to unfold within nanopores[10], thus a cylindrical model is chosen.

The model should show physically correct high and low frequency limits. In the low frequency limit the model should become purely resistive. The impedance of a capacitor is inversely proportional to the applied frequency, thus in the high frequency limit model's impedance should approach zero as does an $R \parallel C$ circuit. EIS spectra for various protein radii should show that when the radius of the protein within the nanopore is increased to encompass the entire nanopore the EIS spectrum approaches that of an ideal capacitor. In addition to this, when the radius of the protein is set to zero the model should reduce to the original VTW model. Since maximizing the negative imaginary impedance of an $R \parallel C$ circuit, with respect to ω yields a peak frequency which is the inverse of the $R \parallel C$ circuit's time constant, then maximizing the modified VTW model with respect to ω should also yield a peak frequency that is inversely proportional to the time constant. Finally, the effect of different magnitudes of differential capacitance on the imaginary component of the impedance are shown. Noting the location of the peak frequency in the imaginary component of the EIS spectrum should allow for the distinguishment of one protein residue from the other, allowing for the rapid sequencing of proteins.

Lasty, to obtain an approximation for the protein double layer differential capacitance an advancement is shown by transforming the Poisson-Boltzmann equation into an operator equation[18, 19, 20, 21, 22] and solving for the first correction to the potential. This first order correction to the potential yields a double layer differential capacitance which is now a function of the surface potential which is then expressed as a function of the zeta potential[23, 24, 25, 26], a regularly measurable quantity. Now having a relationship between the double layer differential capacitance and the zeta potential allows for single molecule or even single residue zeta potential measurements. Since the protein will unfold in a nanopore[10], one can imagine a nano manipulation experiment in which one end of the protein is attached to an AFM tip and it slowly treaded though the nanopore. By measuring the peak frequency as a function of position one can now simply read off the zeta potential as a function of residue. Lastly, if a large nanopore, with a radius greater then the globular protein radius, is used in which the protein does not unfold then the protein will remain globular and one can measure the overall single protein differential capacitance and thus the single protein zeta potential.

3.2 Results and Discussion

3.2.1 Developing the modified differential equation

A differential equation whose solution is used to model the influence on EIS of the geometry and double layer differential capacitance of nanopores has been developed:[15]

$$Z'(x) + i\omega C'(x) Z(x)^2 - R'(x) = 0, \tag{3.1}$$

where,

$$\frac{dR}{dx} = R'(x) = \frac{1}{\pi r^2(x)\kappa_{\mathrm{n}}} \ , \quad \text{and} \quad \frac{dC}{dx} = C'(x) = 2\pi r(x)\widetilde{C}_{\mathrm{n}}, \tag{3.2}$$

Here $i = \sqrt{-1}$, ω is the angular frequency of the AC voltage, x is the coordinate along the length of the nanopore, $\widetilde{C}_{\mathrm{n}}$ is the double-layer differential capacitance of the solution-nanopore wall interface, and κ_{n} is the specific conductivity of the solution within the nanopore. The conductivity within nanopore is found to be higher then that of the bulk, κ [27, 28, 29, 30, 31]. In this formulation, a nanopore of length zero should have zero impedance and provides the boundary condition, $Z(0) = 0$. The circuit element is symmetrized by solving the differential equation with $r(x)$ proceeding from $x = 0$ to $x = L/2$ and then replacing $r(x)$ by $r(L/2 - x)$ and proceeding again from $x = 0$ to $x = L/2$, to obtain the impedance for the total length, L, for the nanopore [15].

For a constant radius, $r(x) = r_\mathrm{n}$, the solution to 3.1 is

$$Z_\mathrm{cyl}(\omega) = R_\mathrm{cyl}\frac{\tanh\left(\sqrt{i\tau_\mathrm{cyl}\omega/4}\right)}{\sqrt{i\tau_\mathrm{cyl}\omega/4}}. \tag{3.3}$$

with

$$R_\mathrm{cyl} = \frac{L}{\pi r_\mathrm{n}^2\kappa_\mathrm{n}}, \tag{3.4a}$$

$$\tau_\mathrm{cyl} = R_\mathrm{cyl}\, C_\mathrm{cyl} = \frac{2L^2\widetilde{C}_\mathrm{n}}{r_\mathrm{n}\kappa_\mathrm{n}}. \tag{3.4b}$$

Other geometries including linearly varying geometries such as an hourglass, lozenge, and conical, as well as quadratically varying geometries were discussed previously[15].

It is known that the strong electric fields inside nanopores can unfold and elongate proteins[10]. Suppose now that an elongated and unfolded protein is traversing the nanopore, while assuming the protein, with radius r_p, is a cylinder with uniform surface charge density which yields a uniform differential capacitance $\widetilde{C}_\mathrm{p}$, and effective length equal to the length, L of the nanopore; only the portion of the protein within the biased region of the nanopore is influencing the nanopore response. The protein excludes some of the volume of the nanopore, thus reducing the volume of solution in the nanopore, thus increasing the nanopore's impedance. In addition to this the surface charge density on the protein adds a differential capacitance to the system. With this, equation 3.2 becomes:

$$\frac{dR}{dx} = R'(x) = \frac{1}{\pi(r_\mathrm{n}^2(x) - r_\mathrm{p}^2(x))\kappa_\mathrm{n}}\ , \quad \text{and} \quad \frac{dC}{dx} = C'(x) = 2\pi(r_\mathrm{n}(x)\widetilde{C}_\mathrm{n} + r_\mathrm{p}(x)\widetilde{C}_\mathrm{p}(x)). \tag{3.5}$$

For constant radii, $r_\mathrm{n}(x) = r_\mathrm{n}$, $r_\mathrm{p}(x) = r_\mathrm{p}$ and constant protein double layer differential capacitance, $\widetilde{C}_\mathrm{p}(x) = \widetilde{C}_\mathrm{p}$ the solution to equation 3.1 with the definitions in equation

3.5 becomes

$$Z_{\text{cyl+p}}(\omega) = R_{\text{cyl+p}} \frac{\text{Tanh}\left(\sqrt{i\tau_{\text{cyl+p}}\omega/4}\right)}{\sqrt{i\tau_{\text{cyl+p}}\omega/4}} \tag{3.6}$$

with

$$R_{\text{cyl+p}} = \frac{L}{\pi(r_{\text{n}}^2 - r_{\text{p}}^2)\kappa_{\text{n}}}, \tag{3.7a}$$

$$\tau_{\text{cyl+p}} = R_{\text{cyl+p}}\, C_{\text{cyl+p}} = \frac{2L^2(\widetilde{C}_{\text{n}} r_n + \widetilde{C}_{\text{p}} r_{\text{p}})}{(r_{\text{n}}^2 - r_{\text{p}}^2)\kappa_{\text{n}}}. \tag{3.7b}$$

Notice equations 3.7a and 3.7b reduce to equations 3.4a and 3.4b when the radius of the protein, r_{p}, is zero. Equivalently, when there is no protein in the nanopore. Notice in equation 3.5 the protein double layer differential capacitance $\widetilde{C}_{\text{p}}$ was fixed to be independent of x. Each protein reside will, however, have a different surface charge density and thus produce a different differential capacitance. Thus the differential capacitance shown here is the average of all the residues. However, by allowing $\widetilde{C}_{\text{p}}$ to vary with x one may solve this piecewise enabling one to sequence a protein. Also, $\widetilde{C}_{\text{n}}$ is presented, independent of x since, in general, nano-pores will have a uniform surface charge density.

3.2.2 Evaluating the solution

Notice in the low frequency limit equation 3.6 reduces to a purely resistive element, that of a conducting solution though a coaxial:

$$\lim_{\omega \to 0} Z_{\text{cyl+p}}(\omega) = \frac{L}{\pi\kappa_{\text{n}}(r_{\text{n}}^2 - r_{\text{p}}^2)} \tag{3.8}$$

which is also equal to equation 3.7a. While in the high frequency limit equation 3.6 is zero

$$\lim_{\omega \to \infty} Z_{\text{cyl+p}}(\omega) = 0, \tag{3.9}$$

and has zero slope. Next, locating the peak frequency can be found by maximizing $-Im[Z_{\text{cyl+p}}(\omega)]$ from equation 3.6 giving

$$\omega_{\text{peak}} \approx 10.16/\tau_{\text{cyl+p}} \tag{3.10}$$

Which is reasonable since the peak frequency of an $R \parallel C$ circuit is located at the inverse of its time constant.

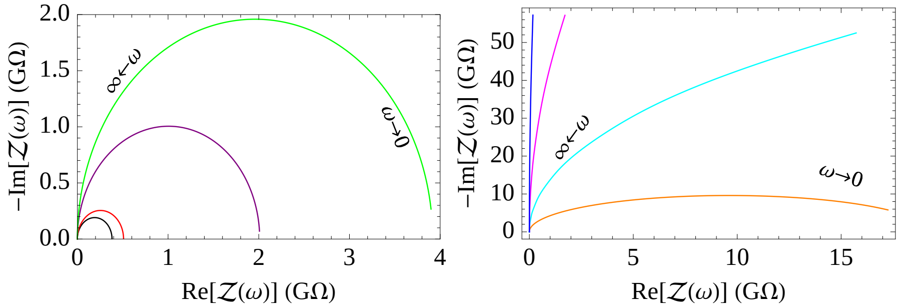

Figure 3.2: Here the EIS spectrum of a protein, modeled as a cylinder, within a nanopore is shown. Both figures show plots of 3.13 with L =60 nm, $\mathrm{r_n}$ =10 nm, $\mathrm{r_s}$ = 100 μm, κ = 0.5 S/m, $\widetilde{C}_{\mathrm{n}} = 1$ mF/m^2, $\widetilde{C}_{\mathrm{p}} = 10$ mF/m^2, and $\epsilon_{\mathrm{s}} = 6$, with $\mathrm{r_p}$ =0 nm, 5 nm, 9 nm, 9.5 nm, 9.9 nm, 9.99 nm, 9.999 nm, and 9.9999 nm, colored black, red, purple, green, orange, cyan, magenta, blue respectively. In the limit the radius of the protein is equal to that of the nanopore, the signal is that of an ideal capacitor.

3.2.3 Completing the model: Inclusion of the chip impedance

The nanopore is not alone, but contained within a substrate, often silicon nitride, who's capacitance is given by

$$C_{\mathrm{s}} = \epsilon_{\mathrm{s}}\epsilon_0 A_{\mathrm{s}}/L \tag{3.11}$$

where ϵ_0 is the permittivity of free space, ϵ_{s} is the dielectric constant of the substrate, $A_{\mathrm{s}} = \pi(r_{\mathrm{s}}^2 - r_{\mathrm{n}}^2)$ is the cross-sectional area of the cylindrical substrate, with r_s being the substrate's radius, and L is the thickness of the substrate and the length of the nanopore though the substrate. While the impedance of this substrate, assuming a perfect capacitor, is given by:

$$Z_{\mathrm{s}} = \frac{1}{i\omega C_{\mathrm{s}}} \tag{3.12}$$

Since the the substrate and nanopore are in parallel the system impedance becomes

$$Z_{\mathrm{sys}} = Z_{\mathrm{cyl+p}} \parallel Z_{\mathrm{s}} \tag{3.13}$$

A final component could be added to this model, the capacitance due to the dielectric of the protein. However, this will have negligible affect on the EIS spectrum.

Equation 3.13 is shown in figure 3.2. Multiple protein radii are shown for a fixed nanopore radius. As the protein's radii approaches the radius of the nanopore the

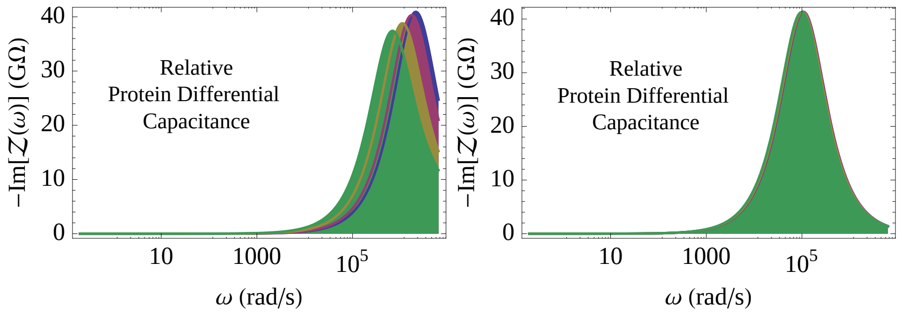

Figure 3.3: The negative imaginary component of equation 3.13 is shown with L=60 nm, r_n =4 nm, r_p =1.5 nm, this is the radius of an unfold protein, r_s =40 nm, κ_n = 0.1 S/m, the experimentally determined[15] nanopore double layer differential capacitance $\widetilde{C}_\mathrm{n}$ = 1 mF/m^2, the calculated protein double layer differential capacitance $\widetilde{C}_\mathrm{p} = 0.1\alpha$ F/m^2, the dielectric constant of the substrate, assuming silicon nitride, ϵ_s = 6, and α = 1,2,5,10, blue, red, yellow, green, respectively. These parameters have been chosen to accentuate the effect of the double layer differential capacitance on the surface of the protein. However, one of the parameters the radius of the substrate, $\mathrm{r_s}$ =50 nm is rather small. The intension is to minimize the capacitance from the substrate so that it does not mask the signal from the capacitance of the double layer of the protein. However, the means that experimentally the nanopore can only be contained in a substrate with a radius of about 50 nm, otherwise the difference in surface charge density from region to region on the protein will not be distinguishable. If one would increase the radius of the substrate to r_s =200 nm then the capacitance of the substrate would mask the signal from the protein as shown in the right panel. Other than changing the radius of the substrate the left and right panels are identically calculated.

EIS spectrum shows that of an ideal capacitor, as one would expect. The system contains a cylinder within a hole in a substrate. As the cylinder fills the hole, the substrate becomes whole, and thus simply a flat substrate. This flat substrate would be accurately modeled as a capacitor.

In figure 3.3 the negative of the imaginary impedance of equation 3.13 vs. frequency is shown for several differential capacitance's on the surface of the protein. As the protein is traversing that nanopore different regions on the protein will have varying amounts of surface charge density. This surface charge density will, when the protein is in a conducting solution, produce a double layer differential capacitance The value of this capacitance can be extracted by fitting to equation 3.13, from which the time constant equation 3.7b is found which is a function of the protein double layer differential capacitance.

Notice equations 3.7a and 3.7b gives 6 physical parameters, r_{p}, r_{n}, $\widetilde{C}_{\mathrm{p}}$, $\widetilde{C}_{\mathrm{n}}$, L and κ_{n}. However these equations only give 2 measurable parameters, $\tau_{\mathrm{cyl+p}}$ and $R_{\mathrm{cyl+p}}$. To obtain all of these parameters a calibration of the nanopore must first be performed to obtain the geometric parameters of the nanopore using equations 3.4a and 3.4b which has been previously shown[15]. After the three geometric parameters of the nanopore is known, along with the nanopore conductivity then the protein parameters may be obtained.

3.2.4 Differential capacitance and zeta potential formalism

Next, an expression for the zeta potential[23, 24, 25, 26] and double layer differential capacitance for a long cylinder is developed. As mentioned before, experimentally the double layer differential capacitance of a protein can be determined. It is shown that once $\widetilde{C}_{\mathrm{p}}$ is found then the surface charge density can be found or visa versa. It is shown that either of these two quantities can be calculated if the zeta potential is known. Since the zeta potential is a regularly measured quantity it would be invaluable to have an expression to calculate the double-layer differential capacitance or surface charge density from the zeta potential. In principle EIS is sensitive to the local differential capacitance enabling a method to measure the local zeta potential.

Beginning with Poisson's equation[12, 32] for a long cylinder, where the potential is independent of the length and angular coordinate:

$$\frac{1}{r}\frac{d}{dr}r\frac{d\Phi(r)}{dr} = -\frac{\rho}{\epsilon_0\epsilon_{\mathrm{r}}} \tag{3.14}$$

With the total charge per unit volume in a given lamina given by the Boltzmann distribution[12, 32]:

$$\rho = \sum_i n_i q z_i = \sum_i n_i^0 q z_i \mathrm{Exp}\left(\frac{-z_i q\Phi}{k_{\mathrm{B}}T}\right) \tag{3.15}$$

where Φ is the potential, k_{B} is Boltzmann's constant, T is absolute temperature, q is the elementary charge, z is the valency, n_i is the species density in the lamina, and n_i^0 is the bulk species density infinitely far from the potential source. Using this density equation

3.15 in equation 3.14 one finds the Poisson-Boltzmann equation for a cylindrical system:

$$\frac{1}{r}\frac{d}{dr}r\frac{d\Phi(r)}{dr} = -\frac{q}{\epsilon_0\epsilon_\mathrm{r}}\sum_i n_i^0 z_i \mathrm{Exp}\left(\frac{-z_i q\Phi(r)}{k_\mathrm{B}T}\right) \tag{3.16}$$

Consider simplifying this for a 1:1 electrolyte such as KCl where $n_1^0 = n_2^0 = n^0$, z_1=1 and $z_2 = -1$:

$$\frac{1}{r}\frac{d}{dr}r\frac{d\Phi(r)}{dr} = \frac{2qn^0}{\epsilon_0\epsilon_\mathrm{r}}\mathrm{Sinh}\left[\frac{q\Phi(r)}{k_\mathrm{B}T}\right] \tag{3.17}$$

For potentials such that $q\Phi$ is less then $k_\mathrm{B}T$, around 20 mV, one can linearize this by keeping the first term of the series expansion of Sinh, one finds:

$$\frac{1}{r}\frac{d}{dr}r\frac{d\Phi(r)}{dr} = \frac{2q^2n^0}{\epsilon_0\epsilon_\mathrm{r}k_\mathrm{B}T}\Phi(r) = \kappa_\mathrm{D}^2\Phi(r) \tag{3.18}$$

Where κ_D is the Debye-Huckle parameter, the inverse of which is the Debye length. With the standard boundary conditions:

$$\lim_{r\to\infty}\Phi(r) = 0 \tag{3.19}$$

This is, as the distance from the surface is large the potential approaches zero. Also,

$$\sigma = -\epsilon_\mathrm{r}\epsilon_0\left(\frac{d\Phi}{dr}\right)_{r=r_\mathrm{p}} \tag{3.20}$$

where σ is the surface charge density, and r_p is the radius of the cylinder, p for protein, which yields

$$\Phi_1(r) = \frac{\sigma K[0, r\kappa_\mathrm{D}]}{\epsilon_\mathrm{r}\epsilon_0\kappa_\mathrm{D}K[1, r_\mathrm{p}\kappa_\mathrm{D}]} \qquad r \geq r_\mathrm{p} \tag{3.21}$$

where K is the modified Bessel function of the second kind. The subscript "1" in the potential is to indicate the solution is to the linear equation where below a correction is shown. The zeta potential can be found by evaluating this, $\Phi_1(r)$ at the slip plane, that is at $r = r_\mathrm{p} + r_\zeta$:

$$\zeta_1 = \frac{\sigma K[0, (r_\mathrm{p} + r_\zeta)\kappa_\mathrm{D}]}{\epsilon_\mathrm{r}\epsilon_0\kappa_\mathrm{D}K[1, r_\mathrm{p}\kappa_\mathrm{D}]} \tag{3.22}$$

where r_ζ is the distance from the surface of the cylinder to the slip plane. The zeta potential is a regularly measured quantity, knowing this and inverting the above equation, one can get the surface charge density on the cylinder or protein.

$$\sigma_1 = \frac{\zeta_1\epsilon_\mathrm{r}\epsilon_0\kappa_\mathrm{D}K[1, r_\mathrm{p}\kappa_\mathrm{D}]}{K[0, (r_\mathrm{p} + r_\zeta)\kappa_\mathrm{D}]} \tag{3.23}$$

This is actually the net surface charge density. Each residue will contribute a given amount of surface charge density; the net surface charge density being the weighted sum of the contribution from each residue, weighted by the surface area of the residue. Next consider the differential capacitance due to the electrical double layer on the surface of the cylinder. Recall the differential capacitance is

$$\widetilde{C} = \frac{d\sigma}{d\Phi_0} \tag{3.24}$$

where Φ_0 is the surface potential. In our case, $\Phi_0 = \Phi(r_\mathrm{p})$. Solving equation 3.21 for the surface charge density, while evaluating this at the radius of the protein

$$\sigma_1 = \frac{\Phi_0 \epsilon_\mathrm{r} \epsilon_0 \kappa_\mathrm{D} K[1, r_\mathrm{p}\kappa_\mathrm{D}]}{K[0, r_\mathrm{p}\kappa_\mathrm{D}]} \tag{3.25}$$

then differentiating with respect to the surface potential yields the electrical double-layer differential capacitance:

$$\widetilde{C}_1 = \frac{\epsilon_\mathrm{r} \epsilon_0 \kappa_\mathrm{D} K[1, r_\mathrm{p}\kappa_\mathrm{D}]}{K[0, r_\mathrm{p}\kappa_\mathrm{D}]} \tag{3.26}$$

Notice, the linearized case is independent of the surface potential. To improve on this we need a correction to the solution to equation 3.21. To do this consider transforming equation 3.17 to a differential equation of the form

$$\Phi(r) = \hat{A}\Phi(r) \tag{3.27}$$

If one has a solution, $\Phi_1(r)$ with $\hat{A}\Phi_1(r)$=$\Phi_2(r)$ and $\hat{A}\Phi_{\mathrm{n}-1}(r)$=$\Phi_\mathrm{n}(r)$, then $\lim_{\mathrm{n}\to\infty}\Phi_\mathrm{n}(r)$= $\Phi(r)$ being the exact solution to the differential equation; for information and examples on Banach space see [18, 19, 20, 21, 22] In our case our $\hat{A}$, is:

$$\hat{A}_\mathrm{cyl} = \frac{k_\mathrm{B}T}{q}\mathrm{Sinh}^{-1}[\frac{\epsilon_\mathrm{r}\epsilon_0}{2qn^0}\frac{1}{r}\frac{d}{dr}r\frac{d}{dr}] = \frac{k_\mathrm{B}T}{q}\mathrm{Sinh}^{-1}[\frac{q}{k_\mathrm{B}T\kappa_\mathrm{D}^2}\frac{1}{r}\frac{d}{dr}r\frac{d}{dr}] \tag{3.28}$$

Notice that

$$\frac{1}{\kappa_\mathrm{D}^2}\frac{1}{r}\frac{d}{dr}r\frac{d}{dr}\Phi_1(r) = \Phi_1(r) \tag{3.29}$$

Thus the 2nd order approximation becomes

$$\Phi_2(r) = \frac{k_\mathrm{B}T}{q}\mathrm{Sinh}^{-1}\left[\frac{q}{k_\mathrm{B}T}\Phi_1(r)\right] = \frac{k_\mathrm{B}T}{q}\mathrm{Sinh}^{-1}\left[\frac{q}{k_\mathrm{B}T}\frac{\sigma K[0, r\kappa_\mathrm{D}]}{\epsilon_\mathrm{r}\epsilon_0\kappa_\mathrm{D}K[1, r_p\kappa_\mathrm{D}]}\right] \qquad r \geq r_\mathrm{p} \tag{3.30}$$

Evaluating 3.30 at r = $\mathrm{r_p}$, the surface of the cylinder, and solving for the surface charge density yields

$$\sigma_2 = \frac{k_{\mathrm{B}}T\epsilon_{\mathrm{r}}\epsilon_0\kappa_{\mathrm{D}}K[1, r_{\mathrm{p}}\kappa_{\mathrm{D}}]\mathrm{Sinh}[q\Phi_0/(k_{\mathrm{B}}T)]}{qK[0, r_{\mathrm{p}}\kappa_{\mathrm{D}}]} \tag{3.31}$$

And using equation 3.24 the double layer differential capacitance becomes

$$\widetilde{C}_2 = \frac{\epsilon_{\mathrm{r}}\epsilon_0\kappa_{\mathrm{D}}K[1, r_{\mathrm{p}}\kappa_{\mathrm{D}}]\mathrm{Cosh}[q\Phi_0/(k_{\mathrm{B}}T)]}{K[0, r_{\mathrm{p}}\kappa_{\mathrm{D}}]} \tag{3.32}$$

Notice

$$\lim_{\Phi_0 \to 0} \widetilde{C}_2 = \widetilde{C}_1 \tag{3.33}$$

Equation 3.32 gives the double layer differential capacitance as a function of the surface potential, this result being the simple geometric capacitance. Solving equation 3.31 for the surface potential an inserting into equation 3.32 gives the double layer differential capacitance as a function of the surface charge density. Neither of which, the surface potential or surface charge density, are easily measurable quantities, however, the zeta potential is. Solving equation 3.30 at the slip plane[12] yields the second order zeta potential

$$\zeta_2 = \frac{k_{\mathrm{B}}T}{q}\mathrm{Sinh}^{-1}\left[\frac{q}{k_{\mathrm{B}}T}\frac{\sigma K[0, (r_p + r_\zeta)\kappa_{\mathrm{D}}]}{\epsilon_r\epsilon_0\kappa_{\mathrm{D}}K[1, r_{\mathrm{p}}\kappa_{\mathrm{D}}]}\right] \tag{3.34}$$

which can be inverted and one can obtain the surface charge density, σ, as a function of zeta potential:

$$\sigma_2(\zeta) = \frac{k_{\mathrm{B}}T\epsilon_{\mathrm{r}}\epsilon_0\kappa_{\mathrm{D}}K[1, (r_{\mathrm{p}} + r_\zeta)\kappa_{\mathrm{D}}]\mathrm{Sinh}[q\zeta/(k_{\mathrm{B}}T)]}{qK[0, r_{\mathrm{p}}\kappa_{\mathrm{D}}]} \tag{3.35}$$

The thickness of the slip plane is approximately the diameter of one solvated ion[12]. Equating equations 3.35 and 3.31, while solving for the surface potential and using this in equation 3.32 yields the double layer differential capacitance as a function of zeta potential.

$$\widetilde{C}_2(\zeta) = \frac{\epsilon_{\mathrm{r}}\epsilon_0\kappa_{\mathrm{D}}K[1, r_{\mathrm{p}}\kappa_{\mathrm{D}}]\sqrt{1 + \frac{K^2[0, r_{\mathrm{p}}\kappa_{\mathrm{D}}]\mathrm{Sinh}^2[q\zeta/k_{\mathrm{B}}T]}{K^2[0, (r_{\mathrm{p}}+r_\zeta)\kappa_{\mathrm{D}})]}}}{K[0, r_{\mathrm{p}}\kappa_{\mathrm{D}}]} \tag{3.36}$$

Lastly, notice

$$\lim_{\zeta \to 0} \widetilde{C}_2(\zeta) = \widetilde{C}_1 \tag{3.37}$$

the second order differential capacitance as a function of the zeta potential, equation 3.37 is equal to the first order differential capacitance equation 3.26 in the limit the surface potential approaches zero. Again, in this limit we return to the purely geometric capacitance.

3.2.5 Transient Analysis

Lastly, transient analysis of alpha synuclein is shown. The left and center panels of figure 3.4 show the excluded volume and the absolute value of the charge in the nanopore as a function of number of amino acids that have traversed the nanopore. Amino acid volume data came from Perkins[33], while pKa data for the charge came from Nazoki and Tanford[34]. The right panel of figure 3.4 shows the peak frequency as a function of number of amino acids that have traversed the nanopore. The peak frequency equation 3.10 is function of the double layer differential capacitance, which was calculated using equations 3.31 and 3.32, where the surface area data came from Samanta et al.[35]. It is assumed that the differential capacitance from each amino acid is additive. This is probably not entirely true since the solution near the boundary of each amino acid will mix. It is also assumed that the protein is static at each instance of measurement, and the applied field is a weak AC field, thus no ionization.

3.3 Conclusion

A model has been developed to predict the impedance of a protein traversing a nanopore, where the protein has been idealized to a cylinder. It has been show that as the protein's radius equals that of the nanopore's radius the overall impedance acts as a capacitor. In addition to this, when the protein's radius is zero, or there is no protein in the nanopore, the formula reduces to the original (VTW) impedance model. The model is able to distinguish one charged region from another on a protein or similar structure by examining the effect on the peak frequency in the negative imaginary impedance. Next, a relationship has been presented to related the double layer differential capacitance to the zeta potential which may allow for single protein or event single residue protein zeta potential measurements. Lastly, transient analysis is present where the peak frequency of a protein traversing a nanopore is shown. It is the authors hope that this model will enable others to further the science of protein sequencing.

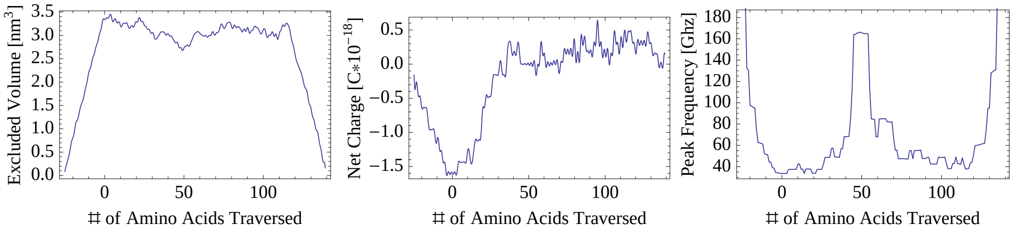

Figure 3.4: The left panel shows the excluded volume for alpha synuclein is shown as a function of the number of amino acids traversed. A protein is composed of numerous amino acids, in the case of alpha synuclein, 140. The shorter the nanopore the more the excluded volume structure is visable. Note that in both panels the zero point is where there are 25 amino acids in the nanopore. The average value of the length of an amino acid is about 0.38 nm. Using a nanopore with an equivalent length of 25 amino acids is about 9.5 nm long. The center panel shows the sum of the charge on the amino acids in the nanopore. The right panel shows the peak frequency for alpha synuclein as a function of the number of amino acids that have traversed the nanopore. Notice at the end points the function seems to diverge. This is due to the short pore used L =9.5 nm. With no protein in the nanopore the time constant is small yielding a large peak frequency. As the double-layer differential capacitance in the nanopore from the protein increases the time constant also increase, thus decreasing the peak frquency. The peak frequency rises again near the center of the figure do to the lack of surface charge density in the central region of alpha synuclein. The protein double layer differential capacitance, which was calculated using equations 3.31 and 3.32. This value was the used to calculate the time constant of the system equation 3.7b, which was then used to calculate the peak frequency, equation 3.10. Notice the time constant of the system with the protein in the nanopore equation 3.7b is a function of the radius of the protein. The radii where calculated by assuming a cylindrical volume with the average length of each amino acid. Then the average value of the radii of the amino acids in the nanopore at a given time was used. Values used include: $\mathrm{r_n}$ =4 nm, $\widetilde{C}_{\mathrm{n}}$ = 1 mF/m^2, T=297 K, with 100 mM KCl yielding a solution conductivity of κ = 1.19 S/m. A solution dielectric constant of $\epsilon_{\mathrm{s}} = 80$ used.

Table 3.1: Nomenclature List

name	definition	SI unit
Z	impedance	$[\Omega]$
R	resistance	$[\Omega]$
C	capacitance	$[F]$
ω	angular frequency	[rad/s]
i	$\sqrt{-1}$	[]
r	radius	[m]
$\widetilde{C}_{\mathrm{n}}$	nanopore double-layer differential capacitance	$[\mathrm{F/m^2}]$
$\widetilde{C}_{\mathrm{p}}$	protein double-layer differential capacitance	$[\mathrm{F/m^2}]$
κ_{n}	nanopore conductivity	[S/m]
L	nanopore length	[m]
Z_{cyl}	cylindrical impedance model	$[\Omega]$
R_{cyl}	resistance of a cylinder	$[\Omega]$
r_{n}	nanopore radius	[m]
r_{p}	protein radius	[m]
r_{s}	substrate radius	[m]
τ_{cyl}	time constant for constant radius nanopore	[s]
$Z_{\mathrm{cyl+p}}$	cylindrical plus protein impedance model	$[\Omega]$
$R_{\mathrm{cyl+p}}$	resistance of a cylinder plus protein	$[\Omega]$
$C_{\mathrm{cyl+p}}$	nanopore and protein double layer capacitance	[F]
$\tau_{\mathrm{cyl+p}}$	time constant for constant radius nanopore plus protein	[s]
C_{s}	substrate capacitance	[F]
A_{s}	substrate area	$[\mathrm{m^2}]$
Z_{s}	substrate impedance	$[\Omega]$
Z_{sys}	system impedance	$[\Omega]$
ϵ_0	permittivity of free space	[F/m]
ϵ_{s}	substrate dielectric constant	[]
α	integer	[]
Φ	potential	[J/C]
q	elementary charge	[q]
k_{B}	Boltzmann constant	[J/K]
T	temperature	[K]
n_i	species density in lamina	$[1/\mathrm{m^3}]$
n_i^0	bulk species density	$[1/\mathrm{m^3}]$
z	valency	[]
κ_{D}	Debye-Huckle parameter	[1/m]
K	modified Bessel function of the second kind	[]
σ	surface charge density	$[\mathrm{C/m^2}]$
Φ_0	surface potential	[J/C]
$\Phi_1(r)$	linearized cylindrical potential	[J/C]
ζ_1	linearized cylindrical zeta potential	[J/C]
σ_1	linearized cylindrical surface charge density	$[\mathrm{C/m^2}]$
$\widetilde{C}_1$	linearized cylindrical differential capacitance	$[\mathrm{F/m^2}]$
$\Phi_2(r)$	second order cylindrical potential	[J/C]
ζ_2	second order cylindrical zeta potential	[J/C]
σ_2	second order cylindrical surface charge density	$[\mathrm{C/m^2}]$
$\widetilde{C}_2$	second order cylindrical differential capacitance	$[\mathrm{F/m^2}]$

Bibliography

[1] Cees. Dekker. Solid-state nanopores. *Nat. Nanotechnol.*, 2:209–215, 2007.

[2] Aigars Piruska, Maojun Gong, Jonathan V. Sweedler, and Paul W. Bohn. Nanofluidics in chemical analysis. *Chem. Soc. Rev.*, 39:1060–1072, 2010.

[3] Y. Tian, X. Hou, L.P. Wen, W. Guo, Y.L. Song, H.Z. Sun, Y.G. Wang, L. Jiang, and D.B. Zhu. A biomimetic zinc activated ion channel. *Chem. Comm.*, 46:1682–1682, 2010.

[4] Z.S. Siwy and S. Howorka. Engineered voltage-responsive nanopores. *Chem. Soc. Rev.*, 39:1115–1132, 2010.

[5] Jason K. Holt, Hyung Gyu Park, Yinmin Wang, Michael Stadermann, Alexander B. Artyukhin, Costas P. Grigoropoulos, Aleksandr Noy, and Olgica. Bakajin. Fast mass transport through sub-2-nanometer carbon nanotubes. *Science*, 312:1034–1037, 2006.

[6] Z. Siwy, E. Heins, C.C. Harrell, P. Kohli, and C.R Martin. Conical-nanotube ion-current rectifiers: the role of surface charge. *J. Am. Chem. Soc.*, 126:10850–10851, 2004.

[7] E.D. Steinle, D.T. Mitchell, M. Wirtz, S.B. Lee, and C.R Young, V.Y Martin. Ion channel mimetic micropore and nanotube membrane sensors. *Anal. Chem.*, 74:2416–2422, 2002.

[8] Stefan Howorka and Zuzanna. Siwy. Nanopore analytics: sensing of single molecules. *Chem. Soc. Rev.*, 38:2360–2384, 2009.

[9] Zhu Chen, Yingbing Jiang, Darren R. Dunphy, David P. Adams, Carter Hodges, Nanguo Liu, Nan Zhang, George Xomeritakis, Xiaozhong Jin, N. R. Aluru,

Steven J. Gaik, Hugh W. Hillhouse, and C. Jeffrey. Brinker. Dna translocation through an array of kinked nanopores. *Nat. Mater.*, 9:667–675, 2010.

[10] D.S. Talaga and J. Li. Single-molecule protein unfolding in solid state nanopores. *J. Am. Chem. Soc.*, 131:9287–9297, 2009.

[11] Daniel Branton, David W. Deamer, Andre Marziali, Hagan Bayley, Steven A. Benner, Thomas Butler, Massimiliano Di Ventra, Slaven Garaj, Andrew Hibbs, Xiaohua Huang, Stevan B. Jovanovich, Predrag S. Krstic, Stuart Lindsay, Xinsheng Sean Ling, Carlos H. Mastrangelo, Amit Meller, John S. Oliver, Yuriy V. Pershin, J. Michael Ramsey, Robert Riehn, Gautam V. Soni, Vincent Tabard-Cossa, Meni Wanunu, Matthew Wiggin, and Jeffery A. Schloss. The potential and challenges of nanopore sequencing. *Nat. Biotechnol.*, 26:1146–1153, 2008.

[12] Allen J. Bard and Larry R. Faulkner. *Electrochemical Methods: Fundamentals and Applications.* John Wiley & Sons, 1980.

[13] Evgenij Barsoukov and Ross. MacDonald. *Impedance Spectroscopy: Theory, Experiment, and Applications, 2nd Edition.* Wiley-Interscience, 2005.

[14] J. Ross Macdonald. *Impedance spectroscopy: emphasizing solid materials and systems.* John Wiley and Sons, 1987.

[15] Michael J. Vitarelli, Shaurya Prakash, and David S. Talaga. Determining nanocapillary geometry from electrochemical impedance spectroscopy using a variable topology network circuit model. *Anal. Chem.*, 83:533–541, 2011.

[16] Eric Nathan Ervin, Henry S. White, Lane A. Baker, and Charles R. Martin. Alternating current impedance imaging of high-resistance membrane pores using a scanning electrochemical microscope. application of membrane electrical shunts to increase measurement sensitivity and image contrast. *Anal. Chem.*, 78:6535–6541, 2006.

[17] Eric Nathan Ervin, Henry S. White, and Lane A. Baker. Alternating current

impedance imaging of membrane pores using scanning electrochemical microscopy. *Anal. Chem.*, 77:5564–5569, 2005.

[18] B. Beauzamy. *Introduction to Banach spaces and their geometry.* Elsevier Science Ltd., 1985.

[19] Z. Wang, B. Guo, G. Zhang, and H. Yu. Study on the electrical double layer of a cylindrical reverse micelle with functional theoretical approach. *Sci. China Ser. B.*, 49:219–224, 2006.

[20] M. Zhou, ZW. Wang, and ZM. Xu. Study on interaction between two parallel plates with iteration method in functional theory. *Chin. J. Chem. Phys.*, 21:131–135, 2008.

[21] M. Zhou, ZW. Wang, and ZM. Xu. Study on the interaction between two identical parallel plates-with iteration method in functional theory. *Acta Phys-Chim. Sin.*, 23:1776–1780, 2007.

[22] ZW. Wang, XM. Liu, HX. Yu, M. Zhou, and J. Jin. Study on electric double layer of a cylindrical particle with functional theoretical approach. *Chinese J. Chem.*, 25:849–856, 2007.

[23] N. Amani, M.R. Saberi, and J.K. Chamani. Investigation by fluorescence spectroscopy, resonance rayleigh scattering and zeta potential approaches of the separate and simultaneous binding effect of paclitaxel and estradiol with human serum albumin. *Protein Pept. Lett.*, 19:935–951, 2011.

[24] A. Doostmohammadi, A. Monshi, R. Salehi, M.H. Fathi, Z. Golniya, and A.U. Daniels. Bioactive glass nanoparticles with negative zeta potential. *Ceram. Int.*, 37:2311–2316, 2011.

[25] P. Leroy, C. Tournassat, and M. Bizi. Influence of surface conductivity on the apparent zeta potential of tio(2) nanoparticles. *J. Colloid Interface Sci.*, 356:442–453, 2011.

[26] Z. Omidvar, K. Parivar, H. Sanee, Z. Amiri-Tehranizadeh, A. Baratian, M.R. Saveri, A. Asoodeh, and J. Chamani. Investigations with spectroscopy, zeta potential and molecular modeling of the non-cooperative behaviour between cyclophosphamide hydrochloride and aspirin upon interaction with human serum albumin: Binary and ternary systems from the view point of multi-drug therapy. *J. Biomol. Struct. Dyn.*, 29:181–206, 2011.

[27] Caroline Desgranges and Jerome. Delhommelle. Molecular simulation of transport in nanopores: Application of the transient-time correlation function formalism. *Phys. Rev. E: Stat., Nonlinear, Soft Matter Phys.*, 77:027701/1–027701/4, 2008.

[28] Rohit Karnik, Rong Fan, Min Yue, Deyu Li, Peidong Yang, and Arun. Majumdar. Electrostatic control of ions and molecules in nanofluidic transistors. *Nano Lett.*, 5:943–948, 2005.

[29] Reto B. Schoch, Harald van Lintel, and Philippe. Renaud. Effect of the surface charge on ion transport through nanoslits. *Phys. Fluids*, 17:100604/1–100604/5, 2005.

[30] Derek Stein, Maarten Kruithof, and Cees. Dekker. Surface-charge-governed ion transport in nanofluidic channels. *Phys. Rev. Lett.*, 93:035901/1–035901/4, 2004.

[31] Yuk Wai Tang, Istvan Szalai, and Kwong-Yu. Chan. Diffusivity and conductivity of a primitive model electrolyte in a nanopore. *Mol. Phys.*, 99:309–314, 2001.

[32] John O'M. Bockris and Amulya K.N. Reddy. *Modern Electrochemistry 1, Seconds Edition: Ionics.* Plenum Pub Corp, 1998.

[33] S.J. Perkins. *Eur. J. Biochem.*, 157:169–180, 1986.

[34] Y. Nozaki and C. Tanford. Examination of titration behavior. *Methods Enzymol*, 11:715–734, 1967.

[35] U. Samanta, R.P Bahadur, and P. Charkrabarti. Quantifying the accessible surface area of protein residues in their local environment. *Protein Eng.*, 15(8):169–180, 2002.

Chapter 4

Focused Ion Beam : FIB

4.1 Introduction

Single solid-state nanopores find increasing use in a variety of applications including, protein translocation dynamics[1, 2, 3], DNA sequencing[4], and other nanofluidic studies[5, 6, 7, 8, 9, 10, 11]. All of these applications are affected by the geometry of the nanopore. This chapter develops the use of electrochemical impedance spectroscopy to determine the geometry and double-layer differential capacitance of a single conical nanopore in a silicon nitride substrate. Here the nanopore is dubbed a FIB or Focused Ion Beam. A true nanopore has a radius around 5 nm. The FIB used in this case has a minimum radius of about 60 nm.

4.2 Methods

The silicon nitride chip is bonded between two cylindrical pieces of polydimethylsiloxane (PDMS) by exposing the PDMS to 50 W oxygen plasma.[12, 13, 14]. This structure is then placed between two glass chambers which contain 5 ml of the test solution in 18 MΩ-cm Millipore water. The test solutions contain 10 mM sodium phosphate buffer used to fix the pH at 7.0±0.1 at each of the four concentrations of KCl: 1.0, 0.5, 0.2, 0.1 M. Bulk conductivities of these solutions were interpolated from published values.[15] A Princeton Applied Research potentiostat, Parstat 2263, was used with a standard 4-electrode permeation cell, with applied 200 mV AC amplitude and no DC bias. 50 frequencies were measured ranging from 0.1 Hz to 1 MHz. Otherwise all experimental techniques used are identical to those discussed in chapter 2.

4.3 Results and Discussion

4.3.1 Conical Model

In Chapter 2 and in our previous paper [14] we developed an impedance model to determine the geometry and of a conical nanopore and electrical double layer differential capacitance within the nanopore:

$$\begin{aligned} Z_{\text{cone}}(\omega) =& \frac{R_{\text{cone}}(I_1(\xi_1)K_1(\xi_0) - I_1(\xi_0)K_1(\xi_1))}{\tau_1 - \tau_0} \times \\ & \left(\frac{\tau_1}{\xi_0(I_2(\xi_0)K_1(\xi_1) + I_1(\xi_1)K_2(\xi_0))} + \frac{\tau_0}{\xi_1(I_2(\xi_1)K_1(\xi_0) + I_1(\xi_0)K_2(\xi_1))} \right) \end{aligned} \tag{4.1}$$

where I_n is the modified Bessel function of the first kind of order n. And K_n is the modified Bessel function of the second kind of order n. Also with,

$$R_{\text{cone}} = \frac{L}{\kappa_{\text{n}} \pi r_1 r_0}, \tag{4.2}$$

and

$$\xi_0 = \sqrt{i4\tau_0\omega} \quad \text{and} \quad \xi_1 = \sqrt{i4\tau_1\omega} \tag{4.3}$$

where,

$$\tau_0 = \frac{2L^2\widetilde{C}_{\text{n}} r_0}{\kappa_{\text{n}}(r_1 - r_0)^2} \quad \text{and} \quad \tau_1 = \frac{2L^2\widetilde{C}_{\text{n}} r_1}{\kappa_{\text{n}}(r_1 - r_0)^2} \tag{4.4}$$

and,

$$\frac{\tau_1}{\tau_0} = \frac{r_1}{r_0}. \tag{4.5}$$

In addition to the impedance of the nanopore, there is the capacitance of the chip which is in parallel to the nanopore:

$$Z_{\text{sys}} = Z_{\text{cone}} \parallel C_{\text{chip}}. \tag{4.6}$$

The capacitance of the chip, C_{chip} can be calculated using the ideal parallel plate model:

$$C_{\text{chip}} = \frac{\epsilon_0 \epsilon_{\text{r}} A}{t} \tag{4.7}$$

where ϵ_0 is the permittivity of free space, ϵ_{r} is the dielectric constant of the chip, A is the cross-sectional area of the chip in parallel to the nanopore, and t is the thickness of

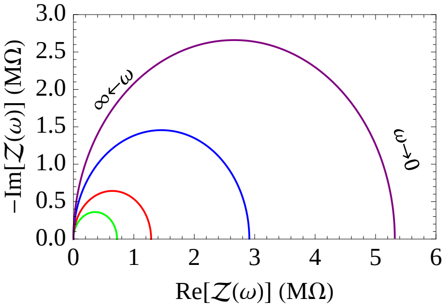

Figure 4.1: Here equation 4.6 is plotted with $L_{\mathrm{n}} = 200$ nm, $r_0 = 60$ nm, $r_1 = 150$ nm, $\widetilde{C}_{\mathrm{n}} = 1$ mF/m^2, $\kappa_0 = 0.136$ S/m, and bulk conductivities of 9.68, 5.37, 2.29, 1.19 S/m, green, red, blue, purple, respectively. The nanopore differential capacitance $\widetilde{C}_{\mathrm{n}}$ was determined previously.[14] The capacitance of the chip, C_{chip}=747 pF was calculated using equation 4.7 with the dielectric constant, ϵ_{r} of silicon nitride being 7, the thickness of the chip t=200 nm, and the area A of the chip being 2.25μm^2. This gives a theoretical expectation of the nanopore impedance with reasonable parameters.

Table 4.1: Parameters for local fits

KCl M	Buffer mM	κ_{b} S/m	τ_0 ms	τ_1 ms	R_{cone} MΩ
1.0	10	9.676±0.049	0.32±0.04	1.05±0.08	0.739±0.001
0.5	10	5.367±0.049	0.48±0.05	1.60±0.11	1.313±0.001
0.2	10	2.291±0.049	0.61±0.06	2.57±0.16	2.987±0.002
0.1	10	1.193±0.049	2.67±0.56	7.03±0.98	5.428±0.005

the chip, which is also equal to the length of the nanopore. This completes the model and is used for local and global fitting though-out. Equation 4.6 is plotted in figure 4.1 in order to give an expectation of what the data should look like. See Appendix B for a derivation and discussion of the parallel plate model.

4.3.2 Local Fitting

The EIS data is presented in Figure 4.2. The left panel shows the run to run variability, while the right panel shows the average of the three runs, at each concentration, fit to equation 4.6. Local fit parameters are shown in Table 4.1. In Figure 4.3 the EIS data scaled by the pore conductivity is presented. It is of particular interest since at higher

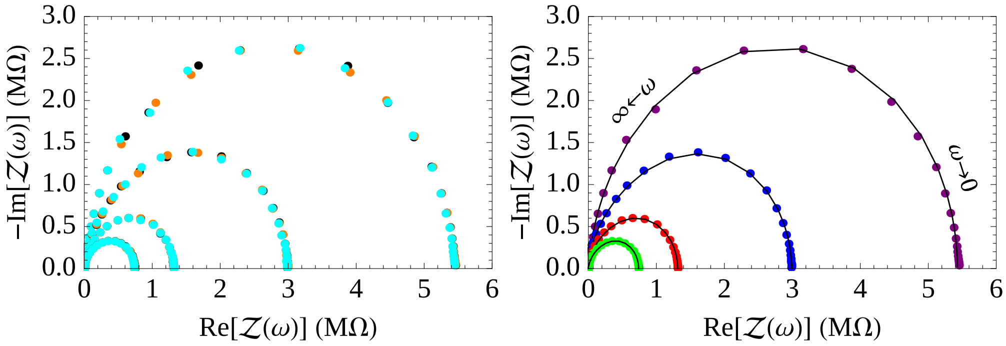

Figure 4.2: Above the EIS data at four different concentrations of phosphate-buffered KCl is shown. The left panel shows the run to run variability. EIS was performed three times at each of the four concentrations. The right panel shows the average of these along with fits to equation 4.6 with fit parameters shown in Table 4.1.

---

concentrations it shows a decrease in the negative imaginary impedance at the peak frequency. This is expected since at higher concentrations the capacitance of the EDL is larger. Causing a greater deviation from an ideal RC circuit.

The DC limited nanopore resistivity is inversely proportional to the conductivity; and, as mentioned earlier, it is known that the nanopore conductivity is higher then that of the bulk conductivity[16, 17, 18, 19, 20]. This is fit to equation 4.8 as a function of the bulk conductivity, and shown in the left panel of figure 4.4.

$$R_{\mathrm{DC}} = \frac{R_{\mathrm{cell}}}{\kappa_{\mathrm{b}} + \kappa_0} = \frac{R_{\mathrm{cell}}}{\kappa_{\mathrm{n}}} \tag{4.8}$$

The nanopore double layer differential capacitance $\widetilde{C}_{\mathrm{n}}$, is partitioned into two layers in series. One, the inner more compact Stern layer $\widetilde{C}_{\mathrm{S}}$, which is approximately independent of solution conductivity, and the outer more diffuse Gouy-Chapman layer $\widetilde{C}_{\mathrm{GC}}$which shows a square root dependence on solution conductivity.[21, 22, 23] Recall capacitive elements add in series add as resisters in parallel:

$$\widetilde{C}_{\mathrm{n}} = \left(\frac{1}{\widetilde{C}_{\mathrm{S}}} + \frac{1}{\widetilde{C}_{\mathrm{GC}}\sqrt{\kappa_{\mathrm{b}}}} \right)^{-1} \tag{4.9}$$

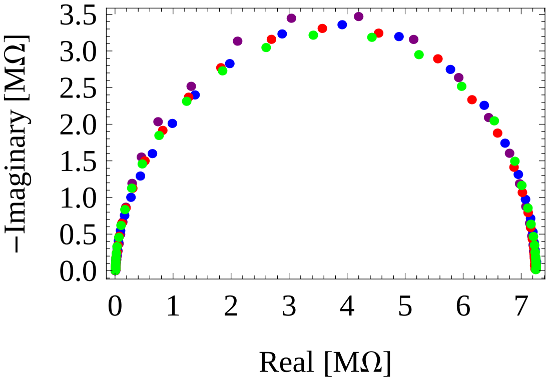

Figure 4.3: Above the EIS data scaled by the pore conductivity is shown, that is both the real and imaginary portions of the EIS spectrum are multiplied by their respective pore conductivity. The net effect is for all the DC limits to be the same. With this scaling one can directly see the effect of the EDL on the impedance. At higher conductivities the capacitance of the EDL is larger thus the deviation from and ideal RC circuit would be larger, in this case causing a decrease in the imaginary impedance at the peak frequency. Where again the bulk conductivities are 9.68, 5.37, 2.29, 1.19 S/m, green, red, blue, purple, respectively.

The nanopore double layer differential capacitance, $\widetilde{C}_{\mathrm{n}}$ may be isolated via a combination of equations 4.2 and 4.3:

$$\widetilde{C}_{\mathrm{n}} = \frac{(\tau_0 - \tau_1)^2 \sqrt{\kappa_{\mathrm{n}}}}{2L^{3/2}\sqrt{\pi\tau_0\tau_1 R_{\mathrm{cone}}}}, \tag{4.10}$$

However, at this point the length of the nanopore is unknown. To compensate for this one can scale the differential capacitance by $L^{3/2}$, yielding:

$$L^{3/2}\widetilde{C}_{\mathrm{n}} = \frac{(\tau_0 - \tau_1)^2 \sqrt{\kappa_{\mathrm{n}}}}{2\sqrt{\pi\tau_0\tau_1 R_{\mathrm{cone}}}}, \tag{4.11}$$

and is plotted in figure 4.4, which is fit to 4.12:

$$L^{3/2}\widetilde{C}_{\mathrm{n}} = L^{3/2}\left(\frac{1}{\widetilde{C}_{\mathrm{S}}} + \frac{1}{\widetilde{C}_{\mathrm{GC}}\sqrt{\kappa_{\mathrm{n}}}}\right)^{-1} = \left(\frac{1}{\widetilde{A}_{\mathrm{S}}} + \frac{1}{\widetilde{B}_{\mathrm{GC}}\sqrt{\kappa_{\mathrm{n}}}}\right)^{-1}, \tag{4.12}$$

where $\widetilde{A}_{\mathrm{S}}=L^{3/2}\widetilde{C}_{\mathrm{S}}$ and $\widetilde{B}_{\mathrm{GC}}=L^{3/2}\widetilde{C}_{\mathrm{GC}}$.

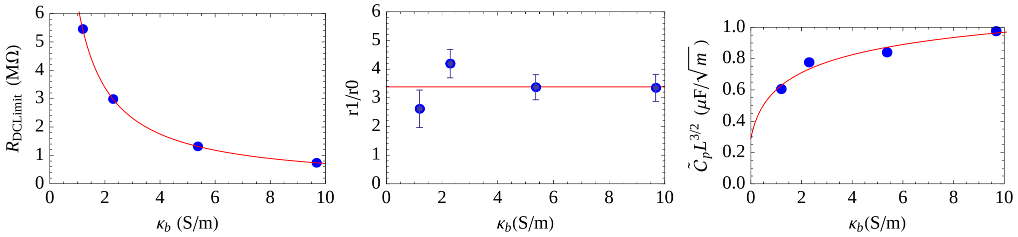

Figure 4.4: Panel A shows the DC limit plotted vs. the bulk conductivity, which is fit to 4.8. From this the nano-pore conductivity offset is obtained that is $\kappa_0 = 0.136$. The center figure shows the ratio of the time constants equation 4.5 and fit to a constant of 3.39. That is $r_1 = 3.39r_0$. In the right panel, the scaled double-layer differential capacitance is shown. The combinations of fit parameters reveals a function form consistent with that of a constant capacitive stern layer and a capacitive Gouy-Chapman layer, depending on the square root of the solution conductivity, all in series. With $\widetilde{A}_{\mathrm{S}}$=1.4±0.18 $\mu\mathrm{F}m^{-1/2}$ and $\widetilde{B}_{\mathrm{GC}}$=0.98±0.18 $\mu\mathrm{F}S^{-1/2}$. Error bars were propagated from the standard errors in the fit parameters.

Table 4.2: Quality of Model Fits

Model	$\chi^2_{\mathrm{m}} \cdot 10^{10}$	p	ν	χ^2_{red}
$R_{\mathrm{pore}} \parallel C_{\mathrm{chip}}$	39.3	8	392	17.6
$Z_{\mathrm{cyl}} \parallel C_{\mathrm{chip}}$	29.1	12	388	13.1
$Z_{\mathrm{cone}} \parallel C_{\mathrm{chip}}$	4.65	16	384	2.12
Global$_1$ $Z_{\mathrm{cone}} \parallel C_{\mathrm{chip}}$	20.2	4	396	8.917
Global$_2$ $Z_{\mathrm{cone}} \parallel C_{\mathrm{chip}}$	20.2	3	397	8.924
Active Set	2.05	40	360	1

4.3.3 Global fitting

There are 7 parameters of interest to this study: The length of the nanopore, L_{n}, the two radii of the conical nanopore r_1 and r_0, the Stern layer differential capacitance $\widetilde{C}_{\mathrm{S}}$, the Gouy-Chapman layer differential capacitance, $\widetilde{C}_{\mathrm{G.S.}}$, the nanopore conductivity off-set κ_0, and the capacitance of the chip C_{chip}. Global fitting was performed two ways. The first way was to fix $\widetilde{C}_{\mathrm{S}}$, $\widetilde{C}_{\mathrm{G.C}}$ and C_{chip}. The second way was to fix $\widetilde{C}_{\mathrm{S}}$, $\widetilde{C}_{\mathrm{G.C}}$, C_{chip}, and κ_0. Global fit parameters are shown in Table 4.3. The geometry is consistent with what was expected. TEM images show a minimum radius of 56.7 nm, while the minimum radius predicted by EIS is 61.3 nm. The thickness of the nanopore 226 nm is consistent with estimations from etching. However, the double-layer differential capacitance is

Table 4.3: FIB EIS global fit parameters

r_0	61.3	±	26.8	nm
r_1	162.6	±	70.7	nm
L_n	226	±	12.4	nm

over 10000 times to large. A possible explanation is a thin oxide layer formed. This could account for some of the increase in the capacitance since a thin oxide layer would have a large surface charge density creating a large differential capacitance. Another explanation is that there is coupling between the double-layer differential capacitance, and the chip capacitance. The chip capacitance will parametrically shift the peak frequency. In this case the time constants from the fit parameters would be to large.

4.4 Conclusion

In conclusion, EIS has been used to determine the geometry and double-layer differential capacitance of a single nanopore in a silicon nitride substrate. A conical nanopore model has been presented and used to fit the EIS data at varying concentrations. The fit parameters indicate a reasonable geometry based on TEM imagery and estimations for etching times, however dramatically over predict the value for the double layer differential capacitance. Possible explanations for the large double-layer differential capacitance is that a thin oxide layer has formed, or that the chip capacitance is coupling with the double layer differential capacitance, shifting the associated time constants to unreasonably large values. Without performing any fits one can simply look at the EIS data and notice the peak frequency is low. This low value also appears in every data set taken on nanopores in these silicon nitride chips. Appendix D shows more examples of EIS data of single nanopores in silicon nitride chips.

Table 4.4: Nomenclature List

name	definition	SI unit
Z	impedance	$[\Omega]$
R	resistance	$[\Omega]$
ω	angular frequency	[rad/s]
i	$\sqrt{-1}$	[]
r	radius	[m]
$\widetilde{C}_{\mathrm{p}}$	nanopore double-layer differential capacitance	$[\mathrm{F/m^2}]$
κ_{b}	bulk conductivity	[S/m]
κ_0	conductivity offset	[S/m]
κ_{n}	nanopore conductivity	[S/m]
L_{n}	nanopore length	[m]
Z_{cyl}	cylindrical impedance model	$[\Omega]$
Z_{cone}	conical impedance model	$[\Omega]$
R_{cyl}	resistance of a cylinder	$[\Omega]$
R_{cone}	resistance of a cone	$[\Omega]$
r_0	entrance radius	[m]
r_1	exit radius	[m]
τ_{cyl}	time constant for constant radius nanopore	[s]
τ_0	time constant for r_0 in Z_{cone}	[s]
τ_1	time constant for r_1 in Z_{cone}	[s]
C_{chip}	chip capacitance	[F]
A_{chip}	chip area	$[\mathrm{m^2}]$
Z_{sys}	system impedance	$[\Omega]$
κ_0	increased nanopore conductivity offset	[S/m]
$\widetilde{C}_{\mathrm{S}}$	Stern layer differential capacitance	$[\mathrm{F/m^2}]$
$\widetilde{C}_{\mathrm{G.C.}}$	Gouy-Chapman layer differential capacitance	$[\mathrm{F/m^2}\sqrt{\mathrm{m/S}}]$
ν	degrees of freedom	[]
p	number of fit parameters	[]
χ^2_{m}	chi squared model	$[\Omega^2]$
χ^2_{as}	chi squared active set	$[\Omega^2]$
χ^2_{red}	reduced chi squared	[]

Bibliography

[1] D.S. Talaga and J. Li. Single-molecule protein unfolding in solid state nanopores. *J. Am. Chem. Soc.*, 131:9287–9297, 2009.

[2] J. Li and D. S. Talaga. The distribution of dna translocation times in solid-state nanopores. *J. Phys. Condens. Mat.*, 22:454129, 2010.

[3] Z. Yang, S. Li, L. Zhang, A. Ur Rehman, and H. Liang. Translocation of alpha-helix chains through a nanopore. *J Chem. Phys.*, 133:154903, 2010.

[4] Daniel Branton, David W. Deamer, Andre Marziali, Hagan Bayley, Steven A. Benner, Thomas Butler, Massimiliano Di Ventra, Slaven Garaj, Andrew Hibbs, Xiaohua Huang, Stevan B. Jovanovich, Predrag S. Krstic, Stuart Lindsay, Xinsheng Sean Ling, Carlos H. Mastrangelo, Amit Meller, John S. Oliver, Yuriy V. Pershin, J. Michael Ramsey, Robert Riehn, Gautam V. Soni, Vincent Tabard-Cossa, Meni Wanunu, Matthew Wiggin, and Jeffery A. Schloss. The potential and challenges of nanopore sequencing. *Nat. Biotechnol.*, 26:1146–1153, 2008.

[5] Y. Tian, X. Hou, L.P. Wen, W. Guo, Y.L. Song, H.Z. Sun, Y.G. Wang, L. Jiang, and D.B. Zhu. A biomimetic zinc activated ion channel. *Chem. Comm.*, 46:1682–1682, 2010.

[6] Z.S. Siwy and S. Howorka. Engineered voltage-responsive nanopores. *Chem. Soc. Rev.*, 39:1115–1132, 2010.

[7] Jason K. Holt, Hyung Gyu Park, Yinmin Wang, Michael Stadermann, Alexander B. Artyukhin, Costas P. Grigoropoulos, Aleksandr Noy, and Olgica. Bakajin. Fast mass transport through sub-2-nanometer carbon nanotubes. *Science*, 312:1034–1037, 2006.

[8] Z. Siwy, E. Heins, C.C. Harrell, P. Kohli, and C.R Martin. Conical-nanotube ion-current rectifiers: the role of surface charge. *J. Am. Chem. Soc.*, 126:10850–10851, 2004.

[9] E.D. Steinle, D.T. Mitchell, M. Wirtz, S.B. Lee, and C.R Young, V.Y Martin. Ion channel mimetic micropore and nanotube membrane sensors. *Anal. Chem.*, 74:2416–2422, 2002.

[10] Cees. Dekker. Solid-state nanopores. *Nat. Nanotechnol.*, 2:209–215, 2007.

[11] Aigars Piruska, Maojun Gong, Jonathan V. Sweedler, and Paul W. Bohn. Nanofluidics in chemical analysis. *Chem. Soc. Rev.*, 39:1060–1072, 2010.

[12] David C. Duffy, J. Cooper McDonald, Olivier J. A. Schueller, and George M. Whitesides. Rapid prototyping of microfluidic systems in poly(dimethylsiloxane). *Anal. Chem.*, 70:4974–4984, 1998.

[13] H. Hillborg, J. F. Ankner, U. W. Gedde, G. D. Smith, H. K. Yasuda, and K. Wikstrom. Crosslinked polydimethylsiloxane exposed to oxygen plasma studied by neutron reflectometry and other surface specific techniques. *Polymer*, 41:6851–6863, 2000.

[14] Michael J. Vitarelli, Shaurya Prakash, and David S. Talaga. Determining nanocapillary geometry from electrochemical impedance spectroscopy using a variable topology network circuit model. *Anal. Chem.*, 83:533–541, 2011.

[15] C. Robert Weast, editor. *CRC Handbook of Chemistry and Physics.* CRC Press, Inc., 1989-1990.

[16] Caroline Desgranges and Jerome. Delhommelle. Molecular simulation of transport in nanopores: Application of the transient-time correlation function formalism. *Phys. Rev. E: Stat., Nonlinear, Soft Matter Phys.*, 77:027701/1–027701/4, 2008.

[17] Rohit Karnik, Rong Fan, Min Yue, Deyu Li, Peidong Yang, and Arun. Majumdar. Electrostatic control of ions and molecules in nanofluidic transistors. *Nano Lett.*, 5:943–948, 2005.

[18] Reto B. Schoch, Harald van Lintel, and Philippe. Renaud. Effect of the surface charge on ion transport through nanoslits. *Phys. Fluids*, 17:100604/1–100604/5, 2005.

[19] Derek Stein, Maarten Kruithof, and Cees. Dekker. Surface-charge-governed ion transport in nanofluidic channels. *Phys. Rev. Lett.*, 93:035901/1–035901/4, 2004.

[20] Yuk Wai Tang, Istvan Szalai, and Kwong-Yu. Chan. Diffusivity and conductivity of a primitive model electrolyte in a nanopore. *Mol. Phys.*, 99:309–314, 2001.

[21] Alexei A.. Kornyshev. Double-layer in ionic liquids: Paradigm change? *J. Phys. Chem. B*, 111:5545–5557, 2007.

[22] John O'M. Bockris, Amulya K.N. Reddy, and Maria Evgenij Gamboa-Aldeco. *Modern Electrochemistry 2A, Second Edition: Fundamentals of Electrodics.* Plenum Pub Corp, 2001.

[23] Jan C. T. Eijkel and Albert. van den Berg. Nanofluidics and the chemical potential applied to solvent and solute transport. *Chem. Soc. Rev.*, 39:957–973, 2010.

Chapter 5

The NCAM DC Bias

5.1 The DC Bias

It is desirable to have a impedance model that not only includes the effects of the AC bias, but also that of the DC bias. Recently[1], experimental data has shown that an increasing DC bias decreases the resistance in nanopores. The plausible explanation is that the effect of the DC bias is to increase the conductivity within the nanopores. In addition to this they show that at low frequency inductive hooks in the impedance spectrum appear. These inductive hooks seem to grow as the DC bias increases. Lastly, it is important to mention that Feng et al.[1] used a single nanopore in a glass substrate while we an array of nanopores in a polycarbonate substrate. Thus, this low frequency phenomenon is not a result of pore-pore coupling but a single nanopore effect. Another possibility was the difference in the ionic mobility of sodium and chloride ions, however Feng et al. used KCl where potassium and chloride ions have similar ionic mobilities, thus ruling out this possibility.

These features, the decrease in nanopore resistivity and the development of low frequency inductive hooks, have also been seen in my data, see figure 5.1 and a close up of the low frequency in figure 5.2 with fits using equation 2.24. Fitting indicates that the conductivity within the nanopore increases as the DC bias increases, as previously seen[1]. However, the fits indicate the the double-layer differential capacitance actually decreases as the DC bias increases. This seems unlikely since there seems to be more ions in the pore as the conductivity in the pore increases so does the double-layer differential capacitance[2, 3, 4]. This may be an artifact in the fit since there is no contribution in the model to account for a DC bias. Lastly, upon examination of the low frequency portion of the fits one can clearly see that the model completely fails in

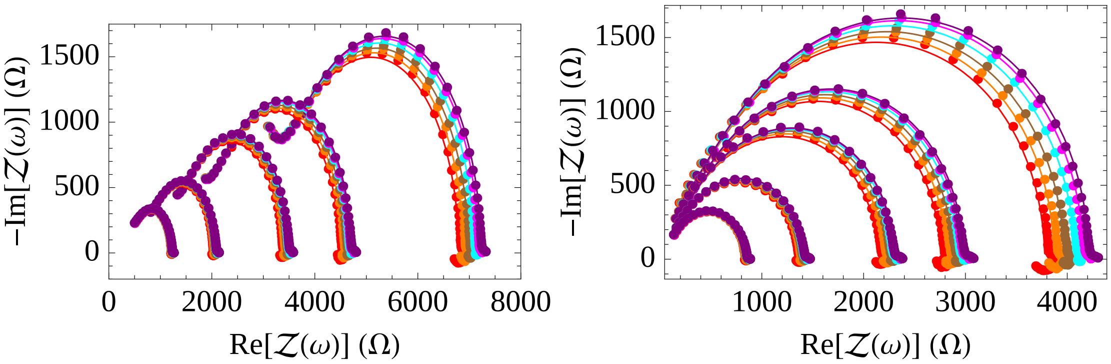

Figure 5.1: Above shows the effect of the DC bias on a NCAM, where the left panel shows the EIS data with background, while the right panel shows the EIS data with the background subtracted. Equation 2.24 was used to fit the EIS data. During fitting the geometric parameters, as indicated in table 2.7 were fixed, while conductivity within the pore and the double-layer differential capacitance were allowed to float. These fits seem deceptively promising, however upon close investigation of the low frequency part of the spectrum one sees that the model completely fails to capture these inductive hooks. This close up is shown in figure 5.2. In all cases, red, orange, brown, cyan, magenta, purple represent, 500, 400, 300, 200, 100, 0 mV DC bias.

---

this region.

5.1.1 Inclusion of an inductor and CPE

To account for this low frequency phenomena Feng et al.[1] used four CPE's to fit their data. This however, is highly unrealistic. Using four CPE's one can fit almost any spectrum. Preliminary fitting indicates that only one CPE is required to fit this data. Equation 5.1 is an extension to equation 2.24 with the addition of one CPE in parallel to the nanopore and an inductor in parallel to the membrane surface effects:

$$Z_{\text{exp}} = \frac{Z_{\text{VTW}}}{N} \parallel C_{\text{mem}} \parallel CPE + R_{\text{ms}} \parallel C_{\text{ms}} \parallel L_{\text{ms}} + R_{\text{bk}} \parallel C_{\text{bk}} \tag{5.1}$$

with

$$Z_{\text{VTW}} = Z_{\text{cyl}} + Z_{\text{loz}}. \tag{5.2}$$

Fitting with equation 5.1 indicates a increase in nanopore conductivity as the DC bias increase and shows an increase in the double-layer differential capacitance as the DC bias increase, as opposed to fitting with equation 2.24. In addition to this fitting

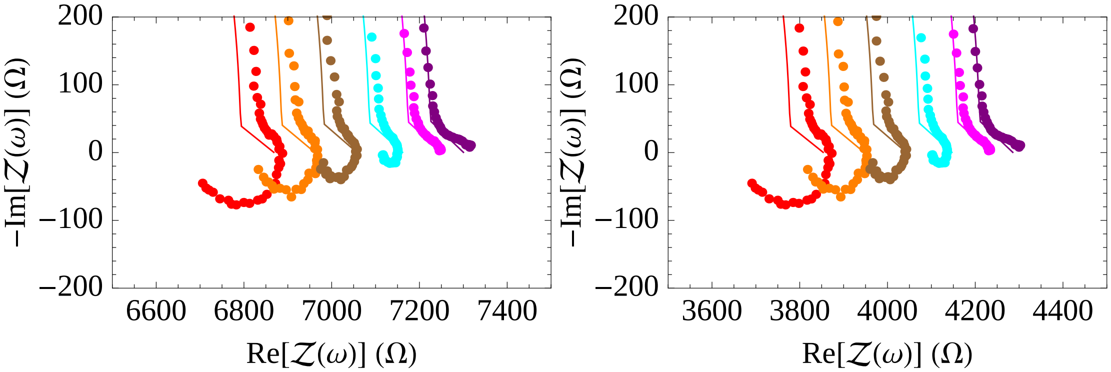

Figure 5.2: Here, a close up of the low frequency spectrum is presented, where the left panel shows the EIS data with background, while the right panel shows the EIS data with the background subtracted. Notice the model equation 2.24 completely fails to capture the low frequency features in the data. There is no element in the model that would produce positive imaginary features, thus a new model is required. Again, red, orange, brown, cyan, magenta, purple represent, 500, 400, 300, 200, 100, 0 mV DC bias.

with equation 5.1 shows and increase in inductance as the DC bias increases. Equation 5.1 captures the low frequency phenomena as shown in figure 5.3, however struggles at low DC bias. At low DC, 0 and 100 mV these extra elements, the inductor and CPE, are not needed produce values for the fit parameters associated with these elements that make their contribution negligible to the overall fit. An element that turns off as the DC bias is lowered would be ideal.

A simple argument to account for the increase in nanopore conductivity as the DC bias increases is as follows. With a negatively charged surface the counter-ions would be possitive. Consider a positive ion near one end of the nanopore. The force due to the DC bias tries to push the ion away from the pore, while the force due to the surface charge density tries to pull it in. At the other end the forces from both DC bias and the surface charge density try to pull the ion into the pore. This effect is opposite for a negativity charged ion. If there are the same amount of positive and negative ions in the pore the effects on the overall nanopore conductivity would cancel. However, there are more positive ions in the pore then negative ions, thus, in net the DC bias, in conjunction with the surface charge density drives more positive ions into the pore then negative ions it excludes. Since this effect is from a simple force balance, it should

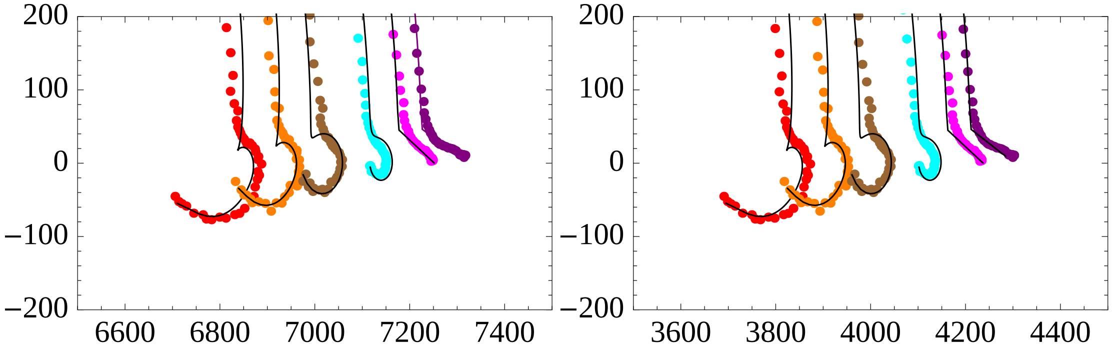

Figure 5.3: Here, a close up of the low frequency spectrum is presented, where the left panel shows the EIS data with background, while the right panel shows the EIS data with the background subtracted. Notice the model equation 5.1 captures the low frequency features in the data. Again, red, orange, brown, cyan, magenta, purple represent, 500, 400, 300, 200, 100, 0 mV DC bias.

be linearly proportionally to the DC bias, which is observed. This higher conductivity is most noticeable for capillaries with diameters comparable to the Debye length at a given electrolyte concentration.[5, 6, 7, 8, 9, 10, 11]

Bibliography

[1] Jingyu Feng, Juan Liu, Baohua Wu, and Gangli. Wang. Impedance characteristics of amine modified single glass nanopores. *Anal. Chem.*, 82:4520–4528, 2010.

[2] G. Gouy. Constitution of the electrical charge at the surface of an electroyte. *J. Phys. Theor. Appl.*, 9:457–468, 1910.

[3] D.A. Chapman. Contribution to the theory of electrocapillarity. *Philos. Mag., Ser. 6*, 25:475–481, 1913.

[4] C. Robert Weast, editor. *CRC Handbook of Chemistry and Physics*. CRC Press, Inc., 1989-1990.

[5] J. J. Tulock, M. A. Shannon, P. W. Bohn, and J. V. Sweedler. Microfluidic separation and gateable fraction collection for mass-limited samples. *Anal. Chem.*, 76:6419–6425, 2004.

[6] Caroline Desgranges and Jerome. Delhommelle. Molecular simulation of transport in nanopores: Application of the transient-time correlation function formalism. *Phys. Rev. E: Stat., Nonlinear, Soft Matter Phys.*, 77:027701/1–027701/4, 2008.

[7] Rohit Karnik, Rong Fan, Min Yue, Deyu Li, Peidong Yang, and Arun. Majumdar. Electrostatic control of ions and molecules in nanofluidic transistors. *Nano Lett.*, 5:943–948, 2005.

[8] Reto B. Schoch, Harald van Lintel, and Philippe. Renaud. Effect of the surface charge on ion transport through nanoslits. *Phys. Fluids*, 17:100604/1–100604/5, 2005.

[9] Derek Stein, Maarten Kruithof, and Cees. Dekker. Surface-charge-governed ion transport in nanofluidic channels. *Phys. Rev. Lett.*, 93:035901/1–035901/4, 2004.

[10] Yuk Wai Tang, Istvan Szalai, and Kwong-Yu. Chan. Diffusivity and conductivity of a primitive model electrolyte in a nanopore. *Mol. Phys.*, 99:309–314, 2001.

[11] Michael J. Vitarelli, Shaurya Prakash, and David S. Talaga. Determining nanocapillary geometry from electrochemical impedance spectroscopy using a variable topology network circuit model. *Anal. Chem.*, 83:533–541, 2011.

Appendix A

Gouy-Chapman Model

A.1 Gouy-Chapman Model

The Gouy-Chapman model[1, 2] shows a square root dependance on the solution concentration. Since at low to moderate concentrations the solution conductivity is proportional to the concentration[3], this implies that the Gouy-Chapman model shows also shows a square root dependance on the solution conductivity. The model is developed for an infinite plate with a surface potential submerged in a conducting solution. Starting with the Boltzmann distribution for charged particles near a potential source:

$$n_i = n_i^o exp\left(\frac{-z_i q \Phi}{kT}\right) \tag{A.1}$$

where Φ is the potential in the lamina, n_i^o is the bulk concentration of species i, n_i is the concentration of species i in a given laminae under the influences of the potential, T is temperature, k is the Boltzmann constant, q is the elementary charge, and z_i is the valency. Notice as the particles are far from the potential source this source becomes zero and the concentration becomes that of the bulk. The total charge per unit volume in a given lamina is:

$$\rho = \sum_i n_i q z_i = \sum_i n_i^o q z_i exp\left(\frac{-z_i q \Phi}{kT}\right) \tag{A.2}$$

Next, recalling Gauss's law:

$$\int \vec{E} \cdot d\vec{A} = \frac{Q_{in}}{\epsilon_0} = \frac{1}{\epsilon_0} \int \rho dV \tag{A.3}$$

where ϵ_0 is the permittivity of free space. Using the divergence theorem:

$$\int \vec{\nabla} \cdot \vec{F} dV = \int \vec{F} \cdot d\vec{A} \tag{A.4}$$

where $\vec{F}$ is an arbitrary vector function, gauss's law can be reformulated in differential form:

$$\vec{\nabla} \cdot \vec{E} = \frac{\rho}{\epsilon_0} \tag{A.5}$$

Next defining the electric field as the gradient of the electric potential:

$$\vec{E} = -\vec{\nabla}\Phi \tag{A.6}$$

Lastly, with equation A.6 and equation A.5, in one dimension, one find the one dimensional Poisson equation:

$$\frac{d^2\Phi}{dx^2} = -\frac{\rho}{\epsilon_o \epsilon_r} \tag{A.7}$$

Where Φ is the potential as a function of the distance from the surface. Using equation A.2 in equation A.7, one finds the 1-Dimensional Poisson-Boltzmann equation:

$$\frac{d^2\Phi}{dx^2} = -\frac{q}{\epsilon_o \epsilon_r} \sum_i n_i^o z_i exp\left(\frac{-z_i q \Phi}{k_\mathrm{B} T}\right) \tag{A.8}$$

Next recall the following identity:

$$2\frac{d^2\Phi}{dx^2} = \frac{d}{d\Phi}\left(\frac{d\Phi}{dx}\right)^2 \tag{A.9}$$

Since:

$$\frac{d}{d\Phi}\left(\frac{d\Phi}{dx}\right)^2 = \frac{d}{dx}\left(\frac{d\Phi}{dx}\right)^2 \frac{dx}{d\Phi} = 2\frac{d\Phi}{dx}\frac{d\Phi^2}{dx^2}\frac{dx}{d\Phi} = 2\frac{d^2\Phi}{dx^2} \tag{A.10}$$

Using equation A.9, equation A.8 becomes:

$$d\left(\frac{d\Phi}{dx}\right)^2 = -\frac{2q}{\epsilon_o \epsilon_r} \sum_i n_i^o z_i exp\left(\frac{-z_i q \Phi}{k_\mathrm{B} T}\right) d\Phi \tag{A.11}$$

Next ntegrating with respect to Φ

$$\left(\frac{d\Phi}{dx}\right)^2 = \frac{2k_\mathrm{B} T}{\epsilon_o \epsilon_r} \sum_i n_i^o z_i exp\left(\frac{-z_i q \Phi}{kT}\right) + Constant \tag{A.12}$$

The constant can be found by noticing that at distances far from the potential source Φ=0 and $d\Phi/dx$=0:

$$\left(\frac{d\Phi}{dx}\right)^2 = \frac{2kT}{\epsilon_o \epsilon_r} \sum_i n_i^o z_i \left[exp\left(\frac{-z_i q \Phi}{k_\mathrm{B} T}\right) - 1\right] \tag{A.13}$$

Next, we simplify this for a symmetrical electrolyte, a z:z electrolyte such as NaCl or KCl, with |z| = 1:

$$\frac{d\Phi}{dx} = \left(\frac{8kTn^o}{\epsilon_o \epsilon_r}\right)^{1/2} \sinh\left(\frac{q\Phi}{2k_\mathrm{B}T}\right) \tag{A.14}$$

Since

$$\sigma = \epsilon_r \epsilon_o \left(\frac{d\Phi}{dx}\right)_{x=0} \tag{A.15}$$

where σ is the surface charge density, one finds:

$$\sigma = (8kTn^o \epsilon_o \epsilon_r)^{1/2} \sinh\left(\frac{q\Phi_o}{2k_\mathrm{B}T}\right) \tag{A.16}$$

where Φ_o is the surface potential. Lastly recall the capacitance per unit area, or differential capacitance:

$$\widetilde{C} = \frac{d\sigma}{d\Phi_o} \tag{A.17}$$

Thus we have the Gouy-Chapman model:

$$\widetilde{C} = \left(\frac{2q^2 n^o \epsilon_o \epsilon_r}{k_\mathrm{B}T}\right)^{1/2} \cosh\left(\frac{q\Phi_o}{2kT}\right) \tag{A.18}$$

Recalling that

$$\frac{2q^2 n^o}{\epsilon_\mathrm{o} \epsilon_\mathrm{r} k_\mathrm{B} T} = \kappa^2 = \frac{1}{\lambda_D^2} \tag{A.19}$$

where κ is the Debye-Huckle parameter, the inverse of which is the Debye length, λ_D. Notice equation A.18 becomes

$$\widetilde{C} = \frac{\epsilon_o \epsilon_r}{\lambda_D} \cosh\left(\frac{q\Phi_o}{2kT}\right) \tag{A.20}$$

Lastly, in the limit the surface potential approaches zero this becomes:

$$\widetilde{C} = \frac{\epsilon_o \epsilon_r}{\lambda_D} \tag{A.21}$$

Which is the geometric capacitance. That is the capacitance where all the counterions are situated at distance equal to the Debye length away from the surface. See appendix B for further information.

Bibliography

[1] G. Gouy. Constitution of the electrical charge at the surface of an electroyte. *J. Phys. Theor. Appl.*, 9:457–468, 1910.

[2] D.A. Chapman. Contribution to the theory of electrocapillarity. *Philos. Mag., Ser. 6*, 25:475–481, 1913.

[3] C. Robert Weast, editor. *CRC Handbook of Chemistry and Physics.* CRC Press, Inc., 1989-1990.

Appendix B

Capacitance Models and the Stern Layer

The parallel plate model, equation 1.57 gives the capacitance of a planar material. However, situations may arise where the material is not planar but possibly spherical or cylindrical. Furthermore, in various limits distributions of charges may assume these convenient geometries. The purpose of this appendix is to give an overview of these models, to give an overview of the electric double layer, and using the planer model to predict the capacitance of the Stern layer.[1]

B.1 Planar Model

The electric field from an infinite plane with surface charge density σ is given by

$$\overrightarrow{E} = \frac{\sigma}{2\epsilon_o}\hat{x} \tag{B.1}$$

If a second infinite plane parallel to the second is given a surface charge density -σ then the field between them is

$$\overrightarrow{E} = \frac{\sigma}{\epsilon_o}\hat{x} \tag{B.2}$$

If the distance between them is H, then the potential difference between them is

$$V = \frac{\sigma H}{\epsilon_o} \tag{B.3}$$

With the capacitance of this parallel plate model is given by

$$C = \frac{\epsilon_o A}{H} \tag{B.4}$$

or in terms of capacitance per area, or differential capacitance

$$\widetilde{C} = \frac{\epsilon_o}{H} \tag{B.5}$$

B.2 Spherical Model

If an inner sphere with radius R and charge Q, and an outer sphere with radius b, and charge -Q, then the electric field between them is

$$\overrightarrow{E} = \frac{Q}{4\pi\epsilon_o r^2}\hat{r} \tag{B.6}$$

recalling that by symmetry the outer sphere does not contribute to the electric field. The difference potential between them is given by

$$V = \frac{Q}{4\pi\epsilon_o}\left(\frac{1}{R} - \frac{1}{b}\right) \tag{B.7}$$

with capacitance given by

$$C = 4\pi\epsilon_o\left(\frac{1}{R} - \frac{1}{b}\right)^{-1} \tag{B.8}$$

If now we let b=R+H, and divide by the area of the inner sphere, $4\pi R^2$ we obtain

$$\widetilde{C} = \frac{\epsilon_o}{H}\left(1 + \frac{H}{R}\right) \tag{B.9}$$

Notice this reduces to B.5 when the radius of the sphere, R becomes large in comparison to H.

B.3 Cylindrical Model

If an inner cylinder with radius R and charge Q on it and an outer cylindrical shell has a radius R+H and charge -Q on it, then the electric field between them is

$$\overrightarrow{E} = \frac{Q}{2\pi\epsilon_o Lr}\hat{r} \tag{B.10}$$

The difference potential between them is given by

$$V = \frac{Q}{2\pi\epsilon_o L} ln\left(1 + H/R\right) \tag{B.11}$$

with capacitance given by

$$C = \frac{2\pi\epsilon_o L}{ln\left(1 + H/R\right)} \tag{B.12}$$

Dividing by the area of the inner cylinder, with area $2\pi RL$ yields

$$\widetilde{C} = \frac{\epsilon_o}{R * ln\,(1 + H/R)} \tag{B.13}$$

Recalling that

$$\lim_{R \to \infty} (1 + H/R)^R = Exp[H] \tag{B.14}$$

one see that equation B.13 reduces to B.5 when the radius of the cylinder becomes large.

B.4 Relation to Stern layer capacitance

If in the above relations we allow a dielectric with dielectric constant ϵ_r to be between the layers and if the distance between the layers, H, is the distance to the Helmholtz plane, then we obtain models for the differential capacitance of the Stern layer. The midpoint of the Stern layer being the Helmholtz plane. One finds

$$\widetilde{C}_H = \begin{cases} \frac{\epsilon_o \epsilon_r}{H} & \text{Planar} \\ \frac{\epsilon_o \epsilon_r}{H}\left(1 + \frac{H}{R}\right) & \text{Spherical} \\ \frac{\epsilon_o \epsilon_r}{R * ln(1+H/R)} & \text{Cylindrical} \end{cases} \tag{B.15}$$

Figure B.1 shows the Stern layer in reference to other constructs within the electrical double layer. The Stern layer is the first layer of solvated counter-ions closest to the material surface. If the surface moves though the solution, or equivalently, solution moves past the surface the Stern layer remains with the material. The boundary between the Stern layer and the more diffused Gouy-Chapman[2, 3] layer is known as the slip plane. Again, this is the boundary between what moves with the surface and what does not. Incidentally, the potential at the slip plane is known as the Zeta potential. The thickness of the Stern layer is about 0.8 nm, half of this, the distance to the Helmholtz plane is about 0.4 nm. With the dialectric constant of water being about 80, the differential capacitance of the Stern layer is about 1.8 F/m^2. Notice in figure B.1 that the capacitance of the Stern layer is in series with the capacitance of the Gouy-Chapman layer, which has a smaller differential capacitance then the Stern layer. Thus, as equation 1.7 shows that if the capacitance of the Gouy-Chapman layer is much smaller then the capacitance of the Stern layer, then the capacitance of the Gouy-Chapman layer will dominate the overall result, yielding a equivalent capacitance smaller then the two.

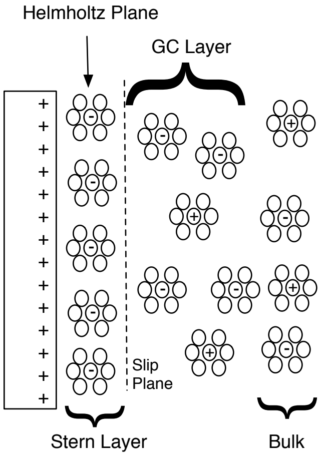

Figure B.1: Here the electrical double layer is shown. It is partitioned into the in Stern layer, the more diffuse Gouy-Chapman layer, and the bulk. The Stern layer is composed of solvated counter-ions, while the Gouy-chapman layer is mixture of solvated counter-ions and solvated species of the same valency a the surface. As one moves further from the surface concentration of counter-ions in the Gouy-Chapman layer falls and the concentration of oppositely charged species increases until one reaches the bulk where net neutrality occurs.

Bibliography

[1] H. Wang and L. Pilon. Accurate simulations of electric double layer capacitance of ultramicroelectrodes. *J. Phys. Chem. C.*, 115:16711–16719, 2011.

[2] G. Gouy. Constitution of the electrical charge at the surface of an electroyte. *J. Phys. Theor. Appl.*, 9:457–468, 1910.

[3] D.A. Chapman. Contribution to the theory of electrocapillarity. *Philos. Mag., Ser. 6*, 25:475–481, 1913.

Appendix C

Warburg Impedance

C.1 Developing the Warburg Impedance Model

The model developed thoughout this dissertation is referred to as the Variable Topology finite Warburg Impedance model [1, 2, 3]. In this appendix the finite length Warburg impedance model is presented. The impedance of which arises from a concentration polarization about two parallel electrodes under an AC bias.

First, consider the concentration of ions nder an AC bias:

$$c(x,t) = c_0 + c_1(x)e^{i\omega t} \tag{C.1}$$

where c_0 is the steady state component, c_1 is the sinusoidally varying component and ω is the frequency of the excitation. On substitution of equation C.1 into Fick's second law:

$$\frac{\partial c}{\partial t} = D\frac{\partial^2 c}{\partial x^2} \tag{C.2}$$

one obtains:

$$i\omega c_1 = D\frac{d^2 c_1}{dx^2} \tag{C.3}$$

The solution of which is:

$$c_1(x) = g\ Sinh[(i\omega/D)^{0.5}x] + h\ Cosh[(i\omega/D)^{0.5}x] \tag{C.4}$$

where D is the diffusion constant. To obtain g and h, first consider a symmetric system where the distance between the electrodes is d, and the origin is at x = 0. Under these conditions notice that when t advances to t $+\pi/\omega$, the electrodes will have reversed polarity and requires the concentration to be, $c_1(-x) = -c_1(x)$ and thus h = 0. With the current being:

$$I(x,t) = zFAD\frac{dc}{dx} = zFADg(i\omega/D)^{0.5}\ Cosh[(i\omega/D)^{0.5}x]e^{i\omega t} \tag{C.5}$$

where A is the electrode cross-sectional area, F is the Faraday constant, and z is the valency. Recalling the linearized Nernst equation:

$$V(x,t) = -\frac{RT}{zFc_0}\Delta c(x,t) \tag{C.6}$$

Since from C.1 on sees that $\Delta c(x,t)$ is:

$$\Delta c(x,t) = c_0 - c(x,t) = -c_1(x)e^{i\omega t} \tag{C.7}$$

The potential difference becomes:

$$V(x,t) = \frac{gRT}{zFc_0}Sinh[(i\omega/D)^{0.5}x]e^{i\omega t} \tag{C.8}$$

Thus the impedance as a function of x becomes:

$$Z(x,\omega) = \frac{RT}{Az^2F^2c_0(i\omega D)^{0.5}}Tanh[(i\omega/D)^{0.5}x] \tag{C.9}$$

Notice this is a function of x. If the distance between the electrodes is d, while recalling the center is at x=0, the the impedance becomes:

$$Z_{W_f}(\omega) = \frac{2RT}{Az^2F^2c_0(i\omega D)^{0.5}}Tanh\left[(i\omega/D)^{0.5}(d/2)\right] \tag{C.10}$$

The model was evaluated at x=d/2 and then multiplied by 2, since the system is symmetric. This model, equation C.10 is known as the finite length Warburg impedance.

C.2 Model Limits

In the limit the separation between the electrodes approaches infinity the finite length Warburg impedance becomes the Warburg impedance model:

$$Z_W(\omega) = \lim_{d\to\infty} Z_{W_f}(\omega) = \frac{2RT}{Az^2F^2c_0(i\omega D)^{0.5}} \tag{C.11}$$

Notice only one diffusion constant, D appears in the above expressions. In this derivation we are assuming all species have the same diffusion constant and valency magnitude.

The finite length Warburg impedance model, equation C.10 has the same functional form, but different parameterization as the cylindrical VTW model, equation 2.6. All three models, equation C.10, equation C.11 and equation 2.6 have the same high frequency limit:

$$\lim_{\omega\to\infty} Z_{W_f}(\omega) = \lim_{\omega\to\infty} Z_W(\omega) = \lim_{\omega\to\infty} Z_{\mathrm{cyl}}(\omega) = 0. \tag{C.12}$$

In the low frequency limit the both the cylindrical VTW model, equation 2.6, and the finite length Warburg impedance model, C.10 have the same limits:

$$\lim_{\omega\to 0} Z_{W_f}(\omega) = \frac{dRT}{Az^2F^2c_0D} \tag{C.13}$$

again however, different parameterizations. But notice the impedance diverges in the low frequency limit for the warburg impedance model:

$$\lim_{\omega\to 0} Z_W(\omega) = \infty \tag{C.14}$$

The source of this divergence being the a-physical construction of the warburg impedance model, that being setting the distance between the electrodes d, to ∞.

Table C.1: Warburg Nomenclature List

name	definition	SI unit
$C(x,t)$	concentration	$[mol/m^3]$
C_0	steady state concentration	$[mol/m^3]$
C_1	sinusoidally varying concentration	$[mol/m^3]$
ω	frequency	$[rad/s]$
t	time	$[s]$
x	coordinate	$[m]$
D	Diffusion constant	$[m^2/s]$
I	Current	$[C/s]$
z	valency	$[]$
F	Faraday constant	$[C/mol]$
A	Cross sectional area	$[m^2]$
V	Potential difference	$[V]$
R	ideal gas constant	$[J/(molK)]$
T	Temperature	$[K]$
$Z(x,\omega)$	impedance	$[\Omega]$
$Z_{\mathrm{W_f}}(\omega)$	Finite length Warburg Impedance	$[\Omega]$
$Z_{\mathrm{W}}(\omega)$	Warburg impedance	$[\Omega]$

Bibliography

[1] E. Warburg. Ueber das verhalten songenannter unpolarisirbarer elektroden gegen wechselstrom. *Ann. Physik.*, 67:493–499, 1899.

[2] J. Ross. Macdonald. Simplified impedance/frequency-response results for intrinsically conducting solids and liquids. *J. Chem. Phys.*, 61:3977–96, 1974.

[3] Donald R. Franceschetti, J. Ross Macdonald, and Richard P. Buck. Interpretation of finite-length-warburg-type impedances in supported and unsupported electrochemical cells with kinetically reversible electrodes. *J. Electrochem. Soc.*, 138:1368–71, 1991.

Appendix D

Other Nanopore EIS Data

D.1 Clogging of a Nanopore

Figure D.1 shows the EIS spectrum on a single nanopore in a silicon nitride chip. During each run a 10 mV AC bias is applied with a 0 mV DC bias in a 10 mM sodium phosphate buffered solution with 1.0 M KCl. The solution was made using Millipore water, however was not post filtered. Each spectrum in figure D.1 is performed identically. However, notice the dramatic difference between the spectra. This difference is attributed to the clogging of the nanopore as a function of run. That is, each time the experiment is performed the nanopore becomes further clogged. A second possible explanation is that the nanopore is de-wetting. This would give a similar effect as clogging. What is interesting to note is the comparison between figure D.1 and figure 3.2 as the proteins radius increases, the protein is clogging the nanopore.

D.2 Gamry Single Nanopore Data

Data presented in figure D.2 was performed on a Gamry Instruments Reference 600 potentiostat on a single nanopore in a silicon nitride chip. During each run a 200 mV AC bias is applied with a 0 mV DC bias in a 10 mM sodium phosphate buffered,2.0, 1.5, 1.0, 0.5 M KCl solution. The solution was made using Millipore water, and was post filtered as opposed to the solution used for the data presented in Figure D.1. It is reasonable to believe that the buffer and KCl had dust in their containers. This bring plausibility to the explanation that the nanopore is clogging as opposed to de-wetting, since this clogging phenomenon was not seen in any further EIS nanopore data, all of which had been post filtered.

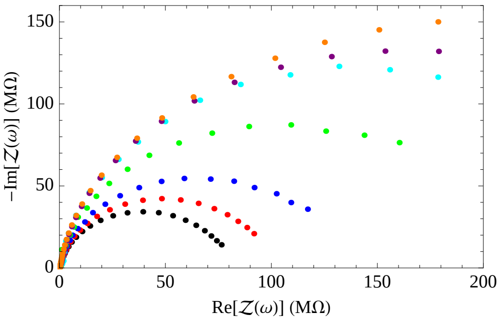

Figure D.1: Here EIS data is shown for what appears to be the clogging of a nanopore. Although millipore water was used, possible dust and other particulates could have been in the dry buffer and KCl, which would clog the nanopore. During each subsequent run the clogging seems to increase. The nanopore is essentially acting as a filter. Each run is performed identically, from black to orange, as explained in the text.

D.3 Parstat 2263 Potentiostat Single Nanopore and FIB

Next, I started using a Princeton Applied Research Parstat 2263 Potentiostat. Figure D.3 shows unequilibrated single-nanopore and single FIB data. These were equilibrated for 4 hours, however for these nanopores that does not seem to be enough time. 24 hours seems to be sufficient. The nanopore used chapter 6 was equilibrated for 24 hours prier to performing the measurement. It's recommended not to simply place the chip in the test solution and wait the 24 hours, but test to make sure the nanopore is actually open, then wait 24 hours to perform runs.

D.4 NCAM Wetting Kinetics

The NCAM takes approximately 48 hours to equilibrate. During this time the nanocapillaries are first hydrated with the conducting solution. Then further equilibration occurs in which additional counter-ions enter the capillaries to neutralize the surface charge density. The EIS data in Figure D.4 was taking on a Princeton Applied Research Parstat 2263 Potentiostat, with 50 frequency points from 1 MHz to 100 mHz and a 20 mV AC and 0 mV DC potential. Using a 1.0 M KCl, 10 mM sodium phosphate buffered solution. The right panel is a plot of the DC limit vs. time, showing an

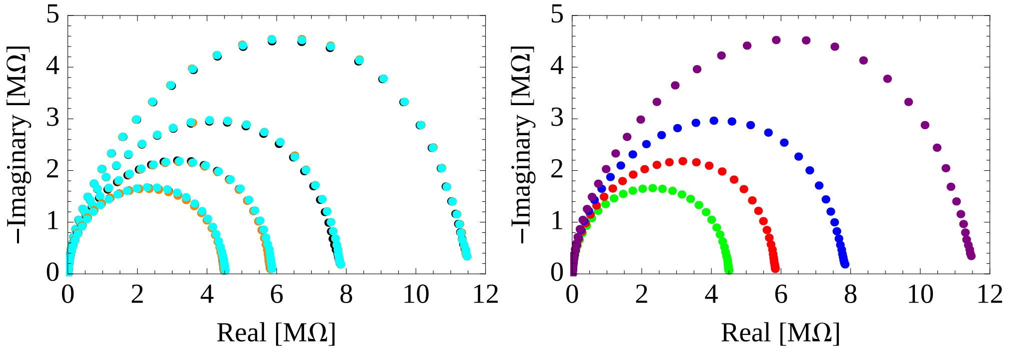

Figure D.2: Left panel shows the run to run variability in the EIS spectrum, while the right panel is the average of the three runs. Simply by inspecting the EIS data on can see that the peak frequency is low indicating a large double-layer differential capacitance, large chip capacitance or a combination of both. With bulk conductivities of 9.68, 5.37, 2.29, 1.19 S/m, green, red, blue, purple, respectively.

---

exponential decay this limit as a function of time, which is fit to equation D.1.

$$1270 * Exp[-0.03t] \tag{D.1}$$

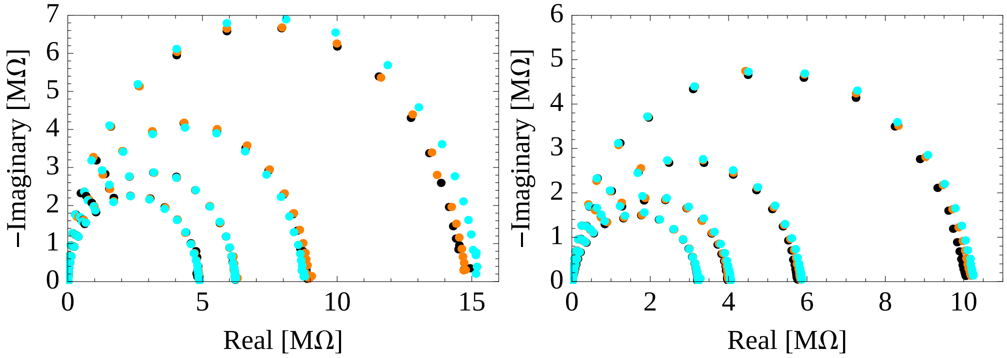

Figure D.3: Left panel shows unequilibrated single nanopore EIS spectra on chip 88728-89133. The right panel shows unequilibrated FIB EIS spectra on chip 88671. There is also a possibility that that the fib was not completely hydrated. That EIS data presented in chapter 6 is on the same chip as that presented in the right panel.

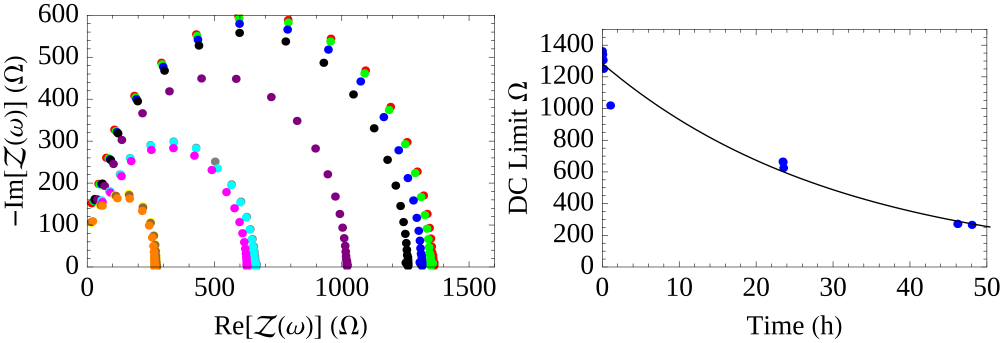

Figure D.4: Left panel shows the EIS of a NCAM. The test solution, a 1.0 M KCl, 10 mM sodium phosphate buffered solution is unchanged from run to run. However, as time progresses the EIS spectrum tends towards lower impedance. As time progresses the nano-capillaries are hydrated and their surface charge density is neutralized, drawing in excess counter-ions. The right panel shows the DC limit as a function of time, which is then fit to an exponential decay, equation D.1. This shows that 48 hours is a minimum amount of time required to properly equilibrate the NCAMs.

Appendix E

Spherical Case

Now, consider the Poisson-Boltzmann equation in spherical coordinates with a symmetric surface potential, thus independent of the θ and ϕ coordinates and simplified to a 1:1 electrolyte:

$$\frac{1}{r^2}\frac{d}{dr}r^2\frac{d\Phi(r)}{dr} = \frac{2qn^o}{\epsilon_o\epsilon_r}Sinh\left[\frac{q\Phi(r)}{kT}\right] \tag{E.1}$$

Then linearized:

$$\frac{1}{r^2}\frac{d}{dr}r^2\frac{d\Phi(r)}{dr} = \kappa^2\Phi(r) \tag{E.2}$$

where κ is again the Debye-Huckle parameter. Using the same boundary conditions as used in the cylindrical case yields

$$\Phi_{sph,1}(r) = \frac{\sigma r_s^2 e^{(r_s-r)\kappa}}{r\epsilon_r\epsilon_o(1+r_s\kappa)} \qquad\qquad r \geq r_s \tag{E.3}$$

Solving equation E.3 for σ the surface charge density at the surface of the sphere $r = r_s$ then differentiating this with respect to the surface potential yields the differential capacitance

$$\widetilde{C}_{sph,1}(r) = \frac{\epsilon_o\epsilon_r}{\lambda_D}\left(1+\frac{\lambda_D}{R}\right) \tag{E.4}$$

where λ_D is the Debye length, the inverse of the Debye-Huckle parameter. This is the geometric capacitance. Physically the meaning of this is that all the counter-ions are situated at a length equal to the Debye length, away from the surface. See Appendix B for more information and derivations.

The Zeta potential is the potential at the slip plate, that is at r = $r_s + r_z$, where r_z is the distance from the surface of the sphere to the slip plane:

$$\zeta_{sph,1} = \frac{\sigma r_s^2 e^{r_z\kappa}}{(r_s+r_z)\epsilon_r\epsilon_o(1+r_s\kappa)} \tag{E.5}$$

To obtain the second order correction we transform our differential equation E.1 to an operator equation:

$$\frac{kT}{q} ArcSinh \left[\frac{\epsilon_o \epsilon_r}{2qn^o} \frac{1}{r^2} \frac{d}{dr} r^2 \frac{d\Phi(r)}{dr} \right] = \Phi(r) \tag{E.6}$$

and noticing that

$$\frac{1}{\kappa^2 r^2} \frac{d}{dr} r^2 \frac{d\Phi(r)}{dr} = \Phi(r) \tag{E.7}$$

Simplifies the operator to

$$\hat{S} = \frac{kT}{q} \mathrm{Sinh}^{-1} \left[\frac{q}{kT} \right] \tag{E.8}$$

Which is the same as in the cylindrical case. Thus:

$$\Phi_{sph,2}(r) = \hat{S} \Phi_{sph,1}(r) = \frac{kT}{q} \mathrm{Sinh}^{-1} \left[\frac{q}{kT} \frac{\sigma r_s^2 e^{(r_s - r)\kappa}}{r \epsilon_r \epsilon_o (1 + r_s \kappa)} \right] \tag{E.9}$$

Solving this for surface charge density at $r = r_s$ then differentiating this with respect to the surface potential yields the differential capacitance

$$\widetilde{C}_{sph,2}(r) = \frac{\epsilon_o \epsilon_r}{\lambda_D} \left(1 + \frac{\lambda_D}{R} \right) Cosh \left[\frac{q\Phi_0}{kT} \right] \tag{E.10}$$

Notice, now we have a differential capacitance that is a function of the surface potential, and as expected with we let this go to zero, then we return to equation E.4

Bibliography

[1] Michael J. Vitarelli, Shaurya Prakash, and David S. Talaga. Determining nanocapillary geometry from electrochemical impedance spectroscopy using a variable topology network circuit model. *Anal. Chem.*, 83:533–541, 2011.

[2] D.S. Talaga and J. Li. Single-molecule protein unfolding in solid state nanopores. *J. Am. Chem. Soc.*, 131:9287–9297, 2009.

[3] J. Li and D. S. Talaga. The distribution of dna translocation times in solid-state nanopores. *J. Phys. Condens. Mat.*, 22:454129, 2010.

[4] Z. Yang, S. Li, L. Zhang, A. Ur Rehman, and H. Liang. Translocation of alpha-helix chains through a nanopore. *J Chem. Phys.*, 133:154903, 2010.

[5] Cees. Dekker. Solid-state nanopores. *Nat. Nanotechnol.*, 2:209–215, 2007.

[6] Daniel Branton, David W. Deamer, Andre Marziali, Hagan Bayley, Steven A. Benner, Thomas Butler, Massimiliano Di Ventra, Slaven Garaj, Andrew Hibbs, Xiaohua Huang, Stevan B. Jovanovich, Predrag S. Krstic, Stuart Lindsay, Xinsheng Sean Ling, Carlos H. Mastrangelo, Amit Meller, John S. Oliver, Yuriy V. Pershin, J. Michael Ramsey, Robert Riehn, Gautam V. Soni, Vincent Tabard-Cossa, Meni Wanunu, Matthew Wiggin, and Jeffery A. Schloss. The potential and challenges of nanopore sequencing. *Nat. Biotechnol.*, 26:1146–1153, 2008.

[7] Y. Tian, X. Hou, L.P. Wen, W. Guo, Y.L. Song, H.Z. Sun, Y.G. Wang, L. Jiang, and D.B. Zhu. A biomimetic zinc activated ion channel. *Chem. Comm.*, 46:1682–1682, 2010.

[8] Z.S. Siwy and S. Howorka. Engineered voltage-responsive nanopores. *Chem. Soc. Rev.*, 39:1115–1132, 2010.

[9] Jason K. Holt, Hyung Gyu Park, Yinmin Wang, Michael Stadermann, Alexander B. Artyukhin, Costas P. Grigoropoulos, Aleksandr Noy, and Olgica. Bakajin. Fast mass transport through sub-2-nanometer carbon nanotubes. *Science*, 312:1034–1037, 2006.

[10] Z. Siwy, E. Heins, C.C. Harrell, P. Kohli, and C.R Martin. Conical-nanotube ion-current rectifiers: the role of surface charge. *J. Am. Chem. Soc.*, 126:10850–10851, 2004.

[11] E.D. Steinle, D.T. Mitchell, M. Wirtz, S.B. Lee, and C.R Young, V.Y Martin. Ion channel mimetic micropore and nanotube membrane sensors. *Anal. Chem.*, 74:2416–2422, 2002.

[12] Aigars Piruska, Maojun Gong, Jonathan V. Sweedler, and Paul W. Bohn. Nanofluidics in chemical analysis. *Chem. Soc. Rev.*, 39:1060–1072, 2010.

[13] Stefan Howorka and Zuzanna. Siwy. Nanopore analytics: sensing of single molecules. *Chem. Soc. Rev.*, 38:2360–2384, 2009.

[14] Zhu Chen, Yingbing Jiang, Darren R. Dunphy, David P. Adams, Carter Hodges, Nanguo Liu, Nan Zhang, George Xomeritakis, Xiaozhong Jin, N. R. Aluru, Steven J. Gaik, Hugh W. Hillhouse, and C. Jeffrey. Brinker. Dna translocation through an array of kinked nanopores. *Nat. Mater.*, 9:667–675, 2010.

[15] Sang Bok Lee and Charles R. Martin. Electromodulated molecular transport in gold-nanotube membranes. *J. Am. Chem. Soc.*, 124:11850–11851, 2002.

[16] S. Prakash, J. Yeom, N. Jin, I. Adesida, and M. A Shannon. Characterization of ionic transport at the nanoscale. *Proc. Inst. Mech. Eng., Part N*, 220:45–52, 2007.

[17] Evin Gultepe, Dattatri Nagesha, Latika Menon, Ahmed Busnaina, and Srinivas. Sridhar. High-throughput assembly of nanoelements in nanoporous alumina templates. *Appl. Phys. Lett.*, 90:163119/1–163119/3, 2007.

[18] Z.X. Lu, A. Namboodiri, and M.M. Collinson. Self-supporting nanopore membranes with controlled pore size and shape. *ACS Nano*, 2:993–999, 2008.

[19] A. V. Raghunathan and N. R. Aluru. Self-consistent molecular dynamics formulation for electric-field-mediated electrolyte transport through nanochannels. *Phys. Rev. E: Stat., Nonlinear, Soft Matter Phys.*, 76:011202/1–011202/12, 2007.

[20] Paula J. Kemery, Jack K. Steehler, and Paul W. Bohn. Electric field mediated transport in nanometer diameter channels. *Langmuir*, 14:2884–2889, 1998.

[21] Matsuhiko Nishizawa, Vinod P. Menon, and Charles R. Martin. Metal nanotubule membranes with electrochemically switchable ion-transport selectivity. *Science*, 268:700–2, 1995.

[22] Meng-Yue Wu, Ralph M. M. Smeets, Mathijs Zandbergen, Ulrike Ziese, Diego Krapf, Philip E. Batson, Nynke H. Dekker, Cees Dekker, and Henny W. Zandbergen. Control of shape and material composition of solid-state nanopores. *Nano Lett.*, 9:479–484, 2009.

[23] A. J. Storm, J. H. Chen, X. S. Ling, H. W. Zandbergen, and C. Dekker. Fabrication of solid-state nanopores with single-nanometre precision. *Nat. Mater.*, 2:537–540, 2003.

[24] Daniel Fologea, James Uplinger, Brian Thomas, David S. McNabb, and Jiali. Li. Slowing dna translocation in a solid-state nanopore. *Nano Lett.*, 5:1734–1737, 2005.

[25] Rohit Karnik, Rong Fan, Min Yue, Deyu Li, Peidong Yang, and Arun. Majumdar. Electrostatic control of ions and molecules in nanofluidic transistors. *Nano Lett.*, 5:943–948, 2005.

[26] R.B. Schoch, J.Y. Han, and P. Renaud. Transport phenomena in nanofluidics. *Rev. Mod. Phys.*, 80:839–883, 2008.

[27] Derek Stein, Maarten Kruithof, and Cees. Dekker. Surface-charge-governed ion transport in nanofluidic channels. *Phys. Rev. Lett.*, 93:035901/1–035901/4, 2004.

[28] Allen J. Bard and Larry R. Faulkner. *Electrochemical Methods: Fundamentals and Applications.* John Wiley & Sons, 1980.

[29] Evgenij Barsoukov and Ross. MacDonald. *Impedance Spectroscopy: Theory, Experiment, and Applications, 2nd Edition.* Wiley-Interscience, 2005.

[30] J. Ross Macdonald. *Impedance spectroscopy: emphasizing solid materials and systems.* John Wiley and Sons, 1987.

[31] Eric Nathan Ervin, Henry S. White, Lane A. Baker, and Charles R. Martin. Alternating current impedance imaging of high-resistance membrane pores using a scanning electrochemical microscope. application of membrane electrical shunts to increase measurement sensitivity and image contrast. *Anal. Chem.*, 78:6535–6541, 2006.

[32] Eric Nathan Ervin, Henry S. White, and Lane A. Baker. Alternating current impedance imaging of membrane pores using scanning electrochemical microscopy. *Anal. Chem.*, 77:5564–5569, 2005.

[33] Digby D.. Macdonald. Reflections on the history of electrochemical impedance spectroscopy. *Electrochim. Acta*, 51:1376–1388, 2006.

[34] James Ross. Macdonald. Impedance spectroscopy: old problems and new developments. *Electrochim. Acta*, 35:1483–92, 1990.

[35] J. M. Kavanagh, S. Hussain, T. C. Chilcott, and H. G. L.. Coster. Fouling of reverse osmosis membranes using electrical impedance spectroscopy: Measurements and simulations. *Desalination*, 236:187–193, 2009.

[36] H.G.L. Coster and T.C Chilcott. *Surface chemistry and electrochemistry of membranes.* Marcel Dekker, Inc., 1999.

[37] H. G. L. Coster, K. J. Kim, K. Dahlan, J. R. Smith, and C. J. D. Fell. Characterization of ultrafiltration membranes by impedance spectroscopy. i. determination of the separate electrical parameters and porosity of the skin and sublayers. *J. Membr. Sci.*, 66:19–26, 1992.

[38] L. Gaedt, T. C. Chilcott, M. Chan, T. Nantawisarakul, A. G. Fane, and H. G. L..

Coster. Electrical impedance spectroscopy characterisation of conducting membranes ii. experimental. *J. Membr. Sci.*, 195:169–180, 2002.

[39] Ming-Chun Chien, Gou-Jen Wang, and Ming-Chang. Yu. Nanopore size estimation by electrochemical impedance spectroscopy analysis. *Jpn. J. Appl. Phys.*, 47:7459–7463, 2008.

[40] H. Kaiser, K. D. Beccu, and M. A.. Gutjahr. Abschtzung der porenstruktur porser elektroden aus impedanzmessungen. *Electrochim. Acta*, 21:539, 1976.

[41] Donald R.. Franceschetti. Small-signal a.c. response of supported thin-layer electrochemical cells. *J. Chem. Phys.*, 86:6495–501, 1987.

[42] Ming-Chun Chien, Gou-Jen Wang, and Win-Chun. Yu. Modeling ion diffusion current in nanochannel using infinitesimal distribution resistor-capacitor circuits. *Jpn. J. Appl. Phys., Part 1*, 46:7436–7440, 2007.

[43] N. Amani, M.R. Saberi, and J.K. Chamani. Investigation by fluorescence spectroscopy, resonance rayleigh scattering and zeta potential approaches of the separate and simultaneous binding effect of paclitaxel and estradiol with human serum albumin. *Protein Pept. Lett.*, 19:935–951, 2011.

[44] A. Doostmohammadi, A. Monshi, R. Salehi, M.H. Fathi, Z. Golniya, and A.U. Daniels. Bioactive glass nanoparticles with negative zeta potential. *Ceram. Int.*, 37:2311–2316, 2011.

[45] P. Leroy, C. Tournassat, and M. Bizi. Influence of surface conductivity on the apparent zeta potential of tio(2) nanoparticles. *J. Colloid Interface Sci.*, 356:442–453, 2011.

[46] Z. Omidvar, K. Parivar, H. Sanee, Z. Amiri-Tehranizadeh, A. Baratian, M.R. Saveri, A. Asoodeh, and J. Chamani. Investigations with spectroscopy, zeta potential and molecular modeling of the non-cooperative behaviour between cyclophosphamide hydrochloride and aspirin upon interaction with human serum albumin:

Binary and ternary systems from the view point of multi-drug therapy. *J. Biomol. Struct. Dyn.*, 29:181–206, 2011.

[47] J.R. Cogdell. *Foundations of Electric Circuits.* Prentice Hall, 1999.

[48] G. Gouy. Constitution of the electrical charge at the surface of an electroyte. *J. Phys. Theor. Appl.*, 9:457–468, 1910.

[49] D.A. Chapman. Contribution to the theory of electrocapillarity. *Philos. Mag., Ser. 6*, 25:475–481, 1913.

[50] Caroline Desgranges and Jerome. Delhommelle. Molecular simulation of transport in nanopores: Application of the transient-time correlation function formalism. *Phys. Rev. E: Stat., Nonlinear, Soft Matter Phys.*, 77:027701/1–027701/4, 2008.

[51] Reto B. Schoch, Harald van Lintel, and Philippe. Renaud. Effect of the surface charge on ion transport through nanoslits. *Phys. Fluids*, 17:100604/1–100604/5, 2005.

[52] Yuk Wai Tang, Istvan Szalai, and Kwong-Yu. Chan. Diffusivity and conductivity of a primitive model electrolyte in a nanopore. *Mol. Phys.*, 99:309–314, 2001.

[53] E. Warburg. Ueber das verhalten songenannter unpolarisirbarer elektroden gegen wechselstrom. *Ann. Physik.*, 67:493–499, 1899.

[54] J. Ross. Macdonald. Simplified impedance/frequency-response results for intrinsically conducting solids and liquids. *J. Chem. Phys.*, 61:3977–96, 1974.

[55] Donald R. Franceschetti, J. Ross Macdonald, and Richard P. Buck. Interpretation of finite-length-warburg-type impedances in supported and unsupported electrochemical cells with kinetically reversible electrodes. *J. Electrochem. Soc.*, 138:1368–71, 1991.

[56] Shaurya Prakash, Aigars Piruska, Enid N. Gatimu, Paul W. Bohn, Jonathan V. Sweedler, and Mark A. Shannon. Nanofluidics: systems and applications. *IEEE Sens. J.*, 8:441–450, 2008.

[57] David C. Duffy, J. Cooper McDonald, Olivier J. A. Schueller, and George M. Whitesides. Rapid prototyping of microfluidic systems in poly(dimethylsiloxane). *Anal. Chem.*, 70:4974–4984, 1998.

[58] J. Cooper McDonald and George M. Whitesides. Poly(dimethylsiloxane) as a material for fabricating microfluidic devices. *Acc. Chem. Res.*, 35:491–499, 2002.

[59] H. Hillborg, J. F. Ankner, U. W. Gedde, G. D. Smith, H. K. Yasuda, and K. Wikstrom. Crosslinked polydimethylsiloxane exposed to oxygen plasma studied by neutron reflectometry and other surface specific techniques. *Polymer*, 41:6851–6863, 2000.

[60] Werner Kern and David A.. Puotinen. Cleaning solution based on hydrogen peroxide for use in silicon semiconductor technology. *RCA Rev.*, 31:187–206, 1970.

[61] Shaurya Prakash, M. B. Karacor, and S. Banerjee. Surface modification in microsystems and nanosystems. *Surf. Sci. Rep.*, 64:233–254, 2009.

[62] C. Robert Weast, editor. *CRC Handbook of Chemistry and Physics.* CRC Press, Inc., 1989-1990.

[63] Jason T. Giurleo and David S.. Talaga. Global fitting without a global model: Regularization based on the continuity of the evolution of parameter distributions. *J. Chem. Phys.*, 128:114114/1–114114/18, 2008.

[64] Hans G. L. Coster. The double fixed charge membrane. low frequency dielectric dispersion. *Biophys. J.*, 13:118–32., 1973.

[65] C. Schonenberger, B. M. I. Van Der Zande, and L. G. J.. Fokkink. Nanowires grown electrochemically in porous templates. *Mater. Res. Soc. Symp. Proc.*, 451:359–365, 1997.

[66] Gonzalo Riveros, Humberto Gomez, Ricardo Schrebler, Ricardo E. Marotti, and Enrique A. Dalchiele. An in situ eis study during the electrochemical growth of copper nanowires into porous polycarbonate membranes. *Electrochem. Solid-State Lett.*, 11:K19–K23, 2008.

[67] Munekazu Motoyama, Yasuhiro Fukunaka, Tetsuo Sakka, Yukio H. Ogata, and Shiomi. Kikuchi. Electrochemical processing of cu and ni nanowire arrays. *Proc. - Electrochem. Soc.*, 2004-19:99–108, 2006.

[68] M. De Leo, F. C. Pereira, L. M. Moretto, P. Scopece, S. Polizzi, and P. Ugo. Towards a better understanding of gold electroless deposition in track-etched templates. *Chem. Mater.*, 19:5955–5964, 2007.

[69] S. Leopold, I. U. Schuchert, J. Lu, M. E. Toimil Molares, M. Herranen, and J.-O. Carlsson. Electrochemical deposition of cylindrical cu/cu2o microstructures. *Electrochim. Acta*, 47:4393–4397, 2002.

[70] E. Ferain and R. Legras. Pore shape control in nanoporous particle track etched membrane. *Nucl. Instrum. Methods Phys. Res., Sect. B*, 174:116–122, 2001.

[71] J. J. Tulock, M. A. Shannon, P. W. Bohn, and J. V. Sweedler. Microfluidic separation and gateable fraction collection for mass-limited samples. *Anal. Chem.*, 76:6419–6425, 2004.

[72] Alexei A.. Kornyshev. Double-layer in ionic liquids: Paradigm change? *J. Phys. Chem. B*, 111:5545–5557, 2007.

[73] John O'M. Bockris, Amulya K.N. Reddy, and Maria Evgenij Gamboa-Aldeco. *Modern Electrochemistry 2A, Second Edition: Fundamentals of Electrodics.* Plenum Pub Corp, 2001.

[74] Jan C. T. Eijkel and Albert. van den Berg. Nanofluidics and the chemical potential applied to solvent and solute transport. *Chem. Soc. Rev.*, 39:957–973, 2010.

[75] N. R. Tas, J. Haneveld, H. V. Jansen, M. Elwenspoek, and A. van den Berg. Capillary filling speed of water in nanochannels. *Appl. Phys. Lett.*, 85:3274–3276, 2004.

[76] B. Beauzamy. *Introduction to Banach spaces and their geometry.* Elsevier Science Ltd., 1985.

[77] Z. Wang, B. Guo, G. Zhang, and H. Yu. Study on the electrical double layer of a cylindrical reverse micelle with functional theoretical approach. *Sci. China Ser. B.*, 49:219–224, 2006.

[78] M. Zhou, ZW. Wang, and ZM. Xu. Study on interaction between two parallel plates with iteration method in functional theory. *Chin. J. Chem. Phys.*, 21:131–135, 2008.

[79] M. Zhou, ZW. Wang, and ZM. Xu. Study on the interaction between two identical parallel plates-with iteration method in functional theory. *Acta Phys-Chim. Sin.*, 23:1776–1780, 2007.

[80] ZW. Wang, XM. Liu, HX. Yu, M. Zhou, and J. Jin. Study on electric double layer of a cylindrical particle with functional theoretical approach. *Chinese J. Chem.*, 25:849–856, 2007.

[81] John O'M. Bockris and Amulya K.N. Reddy. *Modern Electrochemistry 1, Seconds Edition: Ionics.* Plenum Pub Corp, 1998.

[82] S.J. Perkins. *Eur. J. Biochem.*, 157:169–180, 1986.

[83] Y. Nozaki and C. Tanford. Examination of titration behavior. *Methods Enzymol*, 11:715–734, 1967.

[84] U. Samanta, R.P Bahadur, and P. Charkrabarti. Quantifying the accessible surface area of protein residues in their local environment. *Protein Eng.*, 15(8):169–180, 2002.

[85] Jingyu Feng, Juan Liu, Baohua Wu, and Gangli. Wang. Impedance characteristics of amine modified single glass nanopores. *Anal. Chem.*, 82:4520–4528, 2010.

[86] H. Wang and L. Pilon. Accurate simulations of electric double layer capacitance of ultramicroelectrodes. *J. Phys. Chem. C.*, 115:16711–16719, 2011.